SU-SEL-66-112

Photoemission Studies of the Electronic Structure of CdTe, CdSe, and CdS

by

Joseph L. Shay

December 1966

Technical Report No. 5216-1

Prepared under
National Aeronautics and Space Administration
Research Grant No. NGR-05-020-066

Center for Materials Research Contract SD-87

and

National Science Foundation Grants GP-1033 and GK-149

SOLID-STATE ELECTRONICS LABORATORY

STANFORD ELECTRONICS LABORATORIES

STANFORD UNIVERSITY • STANFORD, CALIFORNIA

SEL-66-112

PHOTOEMISSION STUDIES OF THE ELECTRONIC STRUCTURE OF CdTe, CdSe, AND CdS

by

Joseph L. Shay

December 1966

Technical Report No. 5216-1

Prepared under

National Aeronautics and Space Administration
Research Grant No. NGR-05-020-066

Center for Materials Research Contract SD-87

and

National Science Foundation Grants GP-1033 and GK-149

Solid-State Electronics Laboratory
Stanford Electronics Laboratories
Stanford University Stanford, California

ABSTRACT

Photoemission studies are used to determine properties of the electronic structure of CdTe, CdSe, and CdS over an energy range extending from about 10 eV below to 10 eV above the valence band maximum. The features of the photoemission from CdSe and CdS are very similar; however the features of the photoemission from CdTe are quite different from those of CdSe and CdS.

The sharp features of the CdTe photoemission data are due to direct transitions. These direct transitions are assigned to specific regions of the Brillouin zone, and several reflectivity peaks are given new assignments. Although there are sharp matrix-element variations in CdSe and CdS, few of these have been positively identified as being due to direct transitions. Using the density of states analysis, we have separated the matrix-element-dependent transitions from those due only to the density of states.

The mean free path for electron-electron scattering increases in the sequence CdTe, CdSe, and CdS. For electrons about 8.5 eV above the top of the valence band, approximate values for the escape depths are 16, 64, and 75 Å. Since the electron-electron scattering is strongest in CdTe and weakest in CdS, the yield is smallest in CdTe and largest in CdS.

The d-band of cadmium is at about 8 eV below the other valence band states in CdTe, CdSe, and CdS. We show that the slight changes in the location of the d-band in the sequence CdTe, CdSe, and CdS are consistent with both the ionic and the covalent models for the II-VI compounds. Hence we are unable to determine the degree of ionicity of these materials.

CONTENTS

CONTENTS (Cont)

TABLES

ILLUSTRATIONS

ILLUSTRATIONS (Cont)

ILLUSTRATIONS (Cont)

ILLUSTRATIONS (Cont)

SYMBOLS

A	a constant
B	a constant
C	correction term
e	electronic charge
E	electron energy above valence band maximum
$\mathcal{E}$	total system energy
E_g	semiconductor bandgap
E_p	energy of a peak of photoemitted electrons
$E_{v,m}$	vacuum level at metal surface
$E_{v,s}$	vacuum level at semiconductor surface
E_F	Fermi level
f	strength of coupling
F	photon flux
g	small signal conductance
$\hbar$	Planck's constant/2π
$\mathcal{H}$	system Hamiltonian
$\mathcal{H}'$	electron-radiation interaction Hamiltonian
I	photocurrent
I_o	dc bias current
k	wave vector for Bloch function
$\overline{K}$	total wave vector for Slater determinant of Bloch functions
$L(E)$	escape depth for an electron at an energy E
n	refractive index
$n(E)$	normalized energy distribution of photoemitted electrons
N	number of electrons in system
N_c	conduction band density of states
N_v	valence band density of states
$N(j)$	density of one-electron states near state j
N_c^{eff}	effective conduction band density of states

$N_c^{eff'}$	effective conduction band density of states times L(E)
$\bar{p}$	electron momentum operator
R	reflectivity
S	fraction of electrons which are not scattered
T(E)	threshold function (surface transmission probability)
$u_k(x)$	periodic part of Bloch function
U	electrostatic potential due to nuclei
V	voltage applied to photodiode
V_{max}	high-energy intercept on energy distribution
V_o	dc bias voltage
w	transition rate
W	collector work function
x_i	position of electron i
x_{ij}	separation of electrons i and j
α	absorption coefficient
δ	Dirac delta function
σ	optical conductivity
ϵ	one-electron energy eigenvalue
ϵ_2	imaginary part of the dielectric function
φ	one-electron wave function
ψ	many-particle wave function formed from Hartree-Fock one-electron wave functions
Ψ	many-particle eigenfunction of exact Hamiltonian
ω	frequency of electromagnetic radiation

ACKNOWLEDGMENT

I wish to thank Professor W. E. Spicer for his constant guidance and encouragement throughout the course of this work. Thanks are also due Professor F. Herman and Professor D. Stevenson for a careful reading of the manuscript and to R. J. Powell for his frequent advice on experimental techniques. I also wish to express my appreciation to the National Science Foundation for providing the fellowship under which I studied.

I. INTRODUCTION

Until recent years most studies of the electronic properties of semiconductors have been limited to the vicinity of the energy band gap. There have been relatively few experimental studies of the electronic structure far from the band edge. Photoemission and optical experiments provide information about the electronic structure of solids over a region extending from about 10 eV below to 10 eV above the Fermi energy. Photoemission measurements also determine the energies of the initial and final quantum levels involved in an electronic excitation, whereas conventional optical experiments determine only the energy difference between the quantum levels. This work presents the results of photoemission studies of vacuum-cleaved single crystals of CdTe, CdSe, and CdS.

Photoemission from semiconductors is a two-step process involving the photoexcitation of electrons from initial states in the valence band to final states in the conduction band, followed by transport to the surface and escape into vacuum. Frequently the effects of the two steps can be separated and studied independently. Under favorable conditions both the transition probabilities and the scattering mechanisms can be studied. Information about the matrix elements and densities of states causing transition probabilities and the mean free paths for scattering may often be derived from the photoemission data.

One of the principal objectives of this work is to determine the importance of direct transitions in optical excitation. Recent theoretical studies (e.g., PHILLIPS, 1966) proceed on the premise that the major features of the optical properties of semiconductors are due to direct transitions. However, photoemission studies of metals (BERGLUND and SPICER, 1964b; BLODGETT and SPICER, 1965; SPICER, 1966; BLODGETT et al, 1966) and semiconductors (KINDIG and SPICER, 1965a) have revealed that direct transitions are not important for most of the observed transitions. In these studies the photoemission data are explained by a transition probability proportional to the product of the initial and final densities of states. These transitions have been referred to as nondirect transitions. Although we observe both direct and nondirect transitions in the CdTe photoemission data, the sharp features result from direct transitions.

We assign these features to transitions in specific regions of the Brillouin zone. Direct transitions are also observed in the CdSe photoemission data, but they are not as prominent as in CdTe. Other matrix-element-dependent transitions have been observed in CdSe, but these are not necessarily direct transitions. Matrix-element-dependent transitions have also been observed in CdS; these, too, are not necessarily direct transitions.

In Chapter II the quantum theory for the photoexcitation of solids is discussed; Chapter III presents the principles involved in the photoemission experiments; in Chapters IV, V, and VI we present the CdTe, CdSe, and CdS photoemission data and features of the electronic structure deduced from these data; in Chapter VII other results are deduced from the photoemission data.

II. PHOTOEXCITATION OF SOLIDS

A standard result of the band theory of solids is that radiation incident onto a solid induces direct transitions. In a direct transition, both the electron and hole created are in Bloch states which extend throughout the crystal, and the electron wave vector is the same as the hole wave vector. Although most of our photoemission studies of CdTe (Chapter IV) are explained by direct transitions, our photoemission studies of CdSe (Chapter V) and CdS (Chapter VI), as well as other photoemission studies referred to in Chapter I, cannot be explained by direct transitions. Although the failure of the direct transition model is as yet unexplained, it is likely that the explanation involves the approximations essential to the band theory of solids. Accordingly, we discuss these approximations in this chapter. Other models of the electronic structure of solids have been proposed to explain the photoemission data. We also discuss these models in the present chapter.

A. DERIVATION OF CRYSTAL WAVE EQUATION

In this section we outline the derivation of the crystal wave equation of band theory. The block diagram in Fig. 1 shows the essential ingredients in the derivation. This crystal wave equation

$$[-\nabla^2(x) + V(x)]\varphi(x) = \epsilon\varphi(x) \tag{1}$$

begins most discussions of the quantum properties of solids. However, the crystal wave equation is only an approximation to the more fundamental Hartree-Fock equation. This approximation is necessary due to the computational difficulties involved in solving the Hartree-Fock equation for a solid. In this section we discuss some consequences of this approximation. Throughout this chapter we frequently refer to the literature for details and mathematical rigor. We are interested mainly in the physical implications of the various approximations.

We assume that the nuclei are fixed in position; hence Schrödinger's equation for the system of nuclei and N electrons is

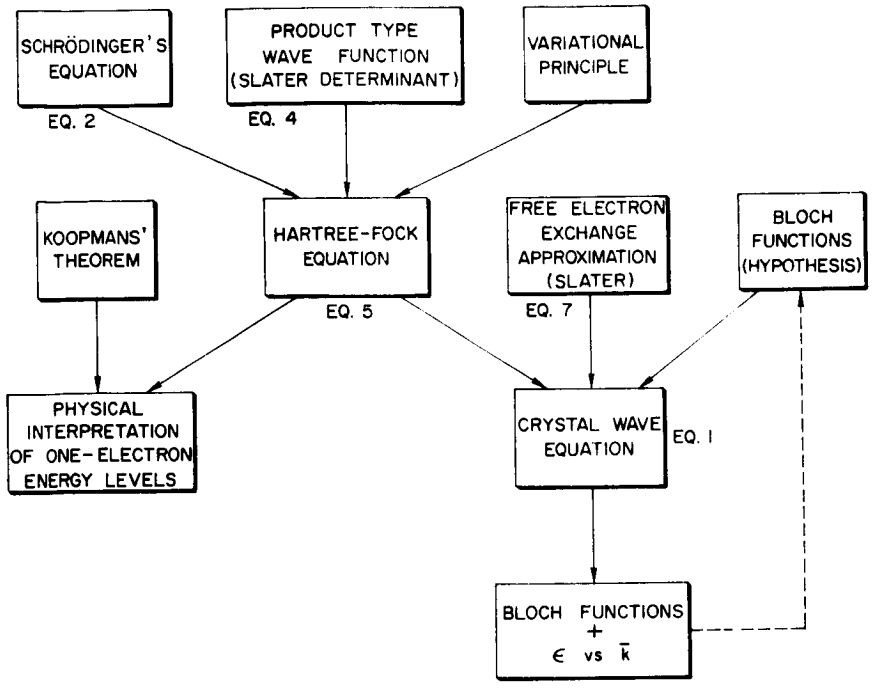

FIG. 1. DERIVATION OF CRYSTAL WAVE EQUATION AND BAND STRUCTURE FROM SCHRÖDINGER'S EQUATION. Equation numbers refer to equations in the text.

$$\left\{ \sum_{i=1}^{N} \left[-\nabla^2(x_i) + U(x_i) \right] + \sum_{i \neq j}^{N} \sum^{N} \frac{1}{|x_{ij}|} \right\} \psi(x_1, x_2, \ldots x_N)$$

$$= \mathcal{H}\psi = \mathcal{E}\psi(x_1, x_2, \ldots x_N) \qquad (2)$$

In Eq. (2), $-\nabla^2(x_i)$ is the kinetic energy operator for electron i, $U(x_i)$ is the potential energy of electron i in the field of the fixed nuclei, and $2/|x_{ij}|$ is the interaction potential between electrons i and j, where $|x_{ij}| \equiv |\bar{x}_i - \bar{x}_j|$. This electron-electron interaction is the most difficult element of this problem, for otherwise Eq. (2) would be separable into N individual equations and the wave function for a stationary state of the entire system would be a product of solutions to the individual problems: $\psi(x_1, x_2, \ldots x_N) = \varphi_a(x_1)\varphi_b(x_2)\ldots\varphi_c(x_N)$. For this wave function the electrons would move independently, and system

properties would be determined by the properties of electron 1 in state a, electron 2 in state b, etc.

As an approximate solution to Eq. (2), let us find the product-type wave function that minimizes the expectation value of the Hamiltonian $\mathcal{H}$. If in Eq. (2) we substitute for ψ a product-type wave function and minimize the energy using variational calculus, we deduce Hartree's equation (HARTREE, 1928):

$$\left\{-\nabla^2(x_1) + U(x_1) + 2\sum_{i\neq j}^{N}\int \frac{|\varphi_j(x_2)|^2}{|x_{12}|}\,dx_2\right\}\varphi_i(x_1) = \varepsilon_i\varphi_i(x_1) \tag{3}$$

This formula explicitly determines the set of φ's which, when joined in a product-type wave function, minimizes the total energy.

The analysis leading to Eq. (3) overlooked the indistinguishability of electrons. For instance, it is not possible to determine which electron is in state a. The product function that we have chosen does not satisfy the Pauli exclusion principle, nor the more fundamental restriction of the Fermi statistics that the wave function should be antisymmetric under interchange of any two electrons. The antisymmetric wave function that comes closest to obeying the hypothesis of statistical independence of all possible one-electron quantities is the Slater determinant:

$$\psi(x_1,x_2,\ldots,x_N) = (N!)^{-1/2}\begin{vmatrix} \varphi_1(x_1) & \varphi_1(x_2) & \ldots & \varphi_1(x_N) \\ \varphi_2(x_1) & & & \cdot \\ \cdot & & & \cdot \\ \cdot & & & \cdot \\ \cdot & & & \\ \varphi_N(x_1) & \varphi_N(x_2) & \ldots & \varphi_N(x_N) \end{vmatrix} \tag{4}$$

Here the coordinate x denotes both space and spin variables. For the determinantal wave function the motion of pairs of electrons is not entirely uncorrelated, because, for instance, the exclusion principle

requires that if $x_1 = x_2$ and if the spin coordinates of the two electrons are identical, then the first two columns are identical and the determinant vanishes.

FOCK (1930) and SLATER (1930) showed that the correct wave equation, allowing for the indistinguishability of electrons, is the Hartree-Fock equation:

$$\left\{-\nabla^2(x_1) + U(x_1) + 2\sum_j^N \int \frac{|\varphi_j(x_2)|^2}{|x_{12}|}\, dx_2\right\} \varphi_i(x_1)$$

$$-2\sum_{\substack{j \\ \| \text{spins}}}^N \left\{\int \frac{\varphi_j^*(x_2)\varphi_i(x_2)dx_2}{|x_{12}|}\right\} \varphi_j(x_1) = \epsilon_i \varphi_i(x_1) \qquad (5)$$

This is an explicit formula for the set of φ's which, when combined in a determinantal wave function, minimizes the energy. Note that the sums over j in Eq. (5) can include $j = i$ because the $j = i$ interaction terms are identical and cancel. Since the linear operator on the left-hand side of Eq. (5) is therefore identical for all φ's, the single particle wave functions are automatically orthogonal for different one-electron eigenvalues ϵ_i (and, of course, orthogonalizable if the eigenvalues are the same).

SLATER (1951) has given the physical significance of each term in Eq. (5). The first term is the kinetic energy of electron 1; the second term is its potential energy in the field of the nuclei. The third term is the potential energy acting on the electron at position x_1 of all the electronic charge, including that of the i^{th} wave function whose wave equation we are writing. The last term, the so-called exchange term, is peculiar in that it is multiplied by $\varphi_j(x_1)$ rather than $\varphi_i(x_1)$. It corrects for the fact that the electron does not act on itself, which it would be doing if this term were omitted.

The exchange operator in Eq. (5) is readily shown to be linear and Hermitian, as are the kinetic and potential energy terms. Hence Eq. (5)

is a wave equation having, in general, an infinite number of solutions, although the sums in Eq. (5) only run over the N orbitals occupied in the Slater determinant. We now discuss the significance of these solutions found in addition to the N orbitals in the ground state determinant.

The Slater determinant of the N occupied orbitals is the Hartree-Fock approximation to the ground state of the system. For this wave function the expectation value of the energy of Eq. (2) is

$$\mathcal{E} = \sum_{j}^{N} \left\{ \epsilon_j - \sum_{i}^{N} \iint \frac{|\varphi_i(x_2)|^2 |\varphi_j(x_1)|^2 dx_1 dx_2}{|x_{12}|} + \sum_{\substack{i \\ \| \text{spins}}}^{N} \iint \frac{\varphi_j^*(x_1)\varphi_i^*(x_2)\varphi_j(x_2)\varphi_i(x_1) dx_1 dx_2}{|x_{12}|} \right\} \tag{6}$$

Note that due to the electron-electron interaction, the total energy is not just the sum of single-particle energies ϵ_j. Approximate excited states can be formed from the approximate ground state by replacing, everywhere in the ground state determinant, one of the occupied orbitals, say $\varphi_i(x)$, by one of the extra orbitals, say $\varphi_\alpha(x)$. We shall now show that the difference in energy between the Hartree-Fock ground state and this approximate excited state is simply related to the single-particle energies ϵ_i and ϵ_α.

The justification for the designation "single-particle energy" is Koopmans' theorem (KOOPMANS, 1933): The difference in energy of two determinantal wave functions, one containing N orbitals and the other containing N-1 orbitals, is ϵ_i, the eigenvalue for the orbital appearing in only one of the determinants. Therefore, the physical significance of the energy parameter $-\epsilon_i$ is that it is approximately the energy required to remove an electron from state i. This is a good approximation to the extent that the N-1 orbital determinant approximates the Hartree-Fock solution for the N-1 particle system. In other words, $-\epsilon_i$ is the energy required to remove an electron from state i if the

other N-1 orbitals remain unchanged. If φ_i is occupied in the Hartree-Fock ground state and φ_α is one of the extra orbitals, then the energy required to take an electron from state i and place it in state α is $\epsilon_\alpha - \epsilon_i$, if the other orbitals remain unchanged (CALLAWAY, 1964, p. 118; SEITZ, 1940, p. 314). Since the energy bands in a solid are determined, in principle, from the Hartree-Fock energy parameters, the physical interpretation of the bands is that afforded by Koopmans' theorem.

Bloch's theorem (BLOCH, 1928) states that the solutions to the crystal wave equation, Eq. (1), are of the form $\varphi_k = u_k(x)\epsilon^{ik\cdot x}$, where $u_k(x)$ has the periodicity of the crystal lattice. It is possible to find Bloch functions as solutions of the Hartree-Fock equation, since the potential and exchange integrals which are computed with the Bloch functions have the proper periodicity. The use of Bloch's theorem as a boundary condition on the wave function is self-consistent. However, it must be kept in mind that Hartree-Fock solutions can be found which are not Bloch functions. In fact, there is no uniqueness theorem for solutions to the Hartree-Fock equation. One can achieve a perfectly self-consistent solution of the Hartree-Fock equation and have it represent not the actual ground state of the system under consideration nor even an approximate exact state (ANDERSON, 1964; OVERHAUSER, 1962).

The exchange operator in Eq. (5) depends on the state i whose wave function is being calculated. Furthermore, it contains a sum over about 10^{23} electrons for a normal solid. Because of these computational difficulties, it is often desirable to approximate the exchange operator by a potential which is the same for all states. The most celebrated such approximation is that proposed by SLATER (1951). The exchange potential in an electron system with a given charge density $\rho = \sum_i \varphi_i^*(x)\varphi_i(x)$ should be about the same as in a free electron gas of the same density. The exchange potential for a free electron gas of density ρ_o is easily found to be $-6(3\rho_o/8\pi)^{1/3}$ (CALLAWAY, 1964). Hence the Slater approximation for the exchange operator is

$$-6\left\{\frac{3}{4\pi}\sum_j(\varphi_j^*\varphi_j)\right\}^{1/3} \qquad (7)$$

The sum includes only states of the same spin as the one on which the exchange operator acts. With this approximation for the exchange and the assumption that the orbitals are Bloch functions, the Hartree-Fock equation (5) takes the form of the crystal wave equation (1). Although this equation is computationally tractable, it has one serious drawback: Koopmans' theorem is not valid for the solutions of the crystal wave equation. Koopmans' theorem is satisfied only to the extent that the Slater approximation adequately represents exchange (LINDGREN, 1965). Consequently, the Hartree-Fock eigenvalues ϵ_j only approximately correspond to one-electron binding energies when this approximate form of the exchange operator is used. This can result in disagreement between energy band calculations and experimental eigenvalues.

B. EXTENSIONS OF HARTREE-FOCK THEORY

The Hartree-Fock wave function is only an approximate solution to the exact problem. A single Slater determinant is not a stationary state of the system. However, the exact ground state can be formed as a linear combination of Slater determinants constructed from the Hartree-Fock orbitals. This is the method of configuration interaction which is discussed in Sec. B1. If the system wave function is initially a single Slater determinant (e.g., immediately after optical excitation), then the system wave function will subsequently evolve into other wave functions of the same total energy. This is the phenomenon of electron-electron scattering which is discussed in Sec. B2.

1. Configuration Interaction

Assume that we have solved the Hartree-Fock equation. We have determined the N orbitals occupied in the ground state wave function, and in general an infinite number of unoccupied orbitals. Let $\varphi_i, \varphi_j, \ldots$ represent orbitals occupied in the Hartree-Fock ground state, and $\varphi_\alpha, \varphi_\beta, \ldots$ represent unoccupied orbitals. Let ψ_i^α represent the Slater determinant formed from the N occupied orbitals, except for φ_i which is everywhere replaced by φ_α. By virtue of Koopmans' theorem (Sec. A), ψ_i^α lies at an energy $\epsilon_\alpha - \epsilon_i$ above the Hartree-Fock ground state energy. Let $\psi_{ij}^{\alpha\beta}$ represent the Slater determinant containing the N occupied

orbitals, except for φ_i which is everywhere replaced by φ_α, and φ_j which is everywhere replaced by φ_β. The energy of this state is $\epsilon_\alpha + \epsilon_\beta - \epsilon_i - \epsilon_j$. The wave functions, $\psi_{ijk}^{\alpha\beta\gamma}$, etc., are similarly constructed.

The Hartree-Fock ground state ψ_o is not a stationary state of the exact Hamiltonian, since we have approximated the electron-electron interaction. However, since each orbital of the infinite set of Hartree-Fock orbitals is an eigenfunction of a linear and Hermitian operator, the collection of all possible N-orbital Slater determinants, $\psi_o, \psi_i^\alpha, \psi_{ij}^{\alpha\beta}, \cdots$, forms a complete set (NESBET, 1958). Configuration interaction is the exact expansion of a stationary state of the system in terms of this complete set.

The configuration interaction expansion for the exact ground state is

$$\Psi_o = a_o\psi_o + \sum_{i\alpha} a_{i\alpha}\psi_i^\alpha + \cdots \tag{8}$$

If the exact ground state is only slightly different from the Hartree-Fock ground state, then a perturbation expansion for the exact ground state gives

$$\Psi_o = \psi_o + \sum_{i\alpha} \frac{\langle\psi_i^\alpha|\mathcal{H}|\psi_o\rangle\psi_i^\alpha}{\epsilon_i - \epsilon_\alpha} + \sum_{ij\alpha\beta} \frac{\langle\psi_{ij}^{\alpha\beta}|\mathcal{H}|\psi_o\rangle\psi_{ij}^{\alpha\beta}}{\epsilon_i + \epsilon_j - \epsilon_\alpha - \epsilon_\beta} \tag{9}$$

If the φ's satisfy the Hartree-Fock equation, then $\langle\psi_o|\mathcal{H}|\psi_i^\alpha\rangle = 0$ (NESBET, 1958). In other words, for the exact Hamiltonian all matrix elements which couple the Hartree-Fock ground state with singly excited states are identically zero. Similarly, for triply excited and higher order terms, Brillouin's theorem (NESBET, 1958) states that $\langle\psi_o|\mathcal{H}|\psi_{ij\ldots}^{\alpha\beta\ldots}\rangle = 0$. In other words, for the exact Hamiltonian, all matrix elements which couple the Hartree-Fock ground state with triply (and higher) excited states are identically zero. This is a special case of a more general theorem: If $\mathcal{H}$ contains only one- and two-electron operators (e.g., $-\nabla^2$ and $1/|x_{ij}|$), then $\langle\Psi_A|\mathcal{H}|\Psi_B\rangle = 0$, if Ψ_A and Ψ_B differ by more than two pairs of occupied orbitals (TINKHAM, 1964). Consequently, to first order in perturbation theory the ground state wave function is

$$\Psi_o = \psi_o + \sum_{ij\alpha\beta} \frac{\langle \psi_{ij}^{\alpha\beta} | \mathcal{H} | \psi_o \rangle \psi_{ij}^{\alpha\beta}}{\epsilon_i + \epsilon_j - \epsilon_\alpha - \epsilon_\beta} \tag{10}$$

i.e., only doubly excited states are mixed into the Hartree-Fock ground state. Furthermore, the φ's are orthogonal since the Hartree-Fock operator is linear and Hermitian; hence, $\langle \psi_o | \psi_{ij}^{\alpha\beta} \rangle = 0$ and we expect $\langle \psi_o | \mathcal{H} | \psi_{ij}^{\alpha\beta} \rangle$ to be small. This accounts for the success of the Hartree-Fock approximation.

The approximate excited states ψ_i^α also are not stationary states of the system. It is readily seen that the only nonvanishing matrix elements couple ψ_i^α to singly, doubly, and triply excited states. Although the largest mixing with ψ_i^α will come from states of the same energy, there also will be contributions to the exact wave function due to approximate excited states with energies unequal to $\epsilon_\alpha - \epsilon_i$. If there exists an exact excited state having nearly the same energy as ψ_i^α, then a perturbation expansion for the exact excited state Ψ gives

$$\Psi \approx \psi_1^\alpha + (\text{large contribution due to states degenerate with } \psi_i^\alpha)$$

$$+ \sum_{j\beta} \frac{\langle \psi_j^\beta | \mathcal{H} | \psi_i^\alpha \rangle \psi_j^\beta}{\epsilon_\alpha - \epsilon_i - \epsilon_\beta + \epsilon_j} + \sum_{j\beta\gamma} \frac{\langle \psi_{ij}^{\beta\gamma} | \mathcal{H} | \psi_i^\alpha \rangle \psi_{ij}^{\beta\gamma}}{\epsilon_\alpha - \epsilon_\beta - \epsilon_\gamma + \epsilon_j}$$

$$+ \sum_{j\beta} \frac{\langle \psi_{ij}^{\alpha\beta} | \mathcal{H} | \psi_i^\alpha \rangle}{\epsilon_j - \epsilon_\beta} \psi_{ij}^{\alpha\beta} + \sum_{jk\beta\gamma} \frac{\langle \psi_{ijk}^{\alpha\beta\gamma} | \mathcal{H} | \psi_i^\alpha \rangle \psi_{ijk}^{\alpha\beta\gamma}}{\epsilon_j + \epsilon_k - \epsilon_\beta - \epsilon_\gamma} \tag{11}$$

2. Electron-Electron Scattering

The physical result of the large contribution in Eq. (11) due to states degenerate with ψ_i^α is electron-electron scattering. If the system wave function is initially ψ_i^α, as might result from electron-hole pair production by the absorption of a photon, then the system wave function will subsequently evolve into other approximate states of the same energy. Only states of the form ψ_j^β, $\psi_{ij}^{\beta\gamma}$, and $\psi_{jk}^{\alpha\beta}$ have nonvanishing matrix elements with ψ_i^α; hence ψ_i^α can scatter only into these states. We

show these scattering events in Fig. 2. In all cases, the electron-hole pair, φ_α and φ_i, was created by a photon of energy $\hbar\omega$.

The scattering event shown in Fig. 2a is not easily detected experimentally. If a measurement indicates that the system is in state ψ_j^β, it is difficult to determine whether ψ_j^β resulted from the scattering of ψ_i^α, or the system was optically excited to ψ_j^β. However, scattering from ψ_i^α to $\psi_{ij}^{\alpha\beta}$ or $\psi_{jk}^{\alpha\beta}$ (Figs. 2b and 2c) is easily observed, since $\psi_{ij}^{\alpha\beta}$ and $\psi_{jk}^{\alpha\beta}$ are not optically excited. These doubly excited states are not optically excited from the ground state ψ_o since the electron-radiation interaction is a one-electron operator and hence couples ψ_o only to singly excited states. The scattering event shown in Fig. 2a can be observed whenever optical excitation to ψ_j^β is forbidden. If a measurement indicates that the system is in state ψ_j^β then this state resulted from the scattering of some other state ψ_i^α which was optically excited.

The scattering events depicted in Figs. 2b and 2c are the familiar electron and hole scattering events. In Fig. 2b an electron scatters from φ_α to φ_β, and an electron-hole pair, φ_γ and φ_j, is created. Regarding the indices i, j, α, β, etc. as continuous variables for a solid, the golden rule of perturbation theory (SCHIFF, 1955) requires that ψ_i^α scatters into states near $\psi_{ij}^{\beta\gamma}$ at a rate

$$w(\psi_i^\alpha \rightarrow \psi_{ij}^{\beta\gamma}) = \frac{2\pi}{\hbar} \left|\langle \psi_i^\alpha | \mathcal{H} | \psi_{ij}^{\beta\gamma} \rangle\right|^2 N(j)N(\gamma)N(\beta)\delta(\epsilon_\alpha - \epsilon_\beta - \epsilon_\gamma + \epsilon_j) \qquad (12)$$

where $N(j)$ is the density of one-electron states near state φ_j.

It is apparent from Fig. 2b that an electron can lose a minimum energy equal to the band gap, E_g; by conservation of energy and Koopmans' theorem $\epsilon_\alpha - \epsilon_\beta = \epsilon_\gamma - \epsilon_j \geq E_g$. Also, since $N(j)$ and $N(\gamma)$ are small near the band edge, the probability of an electron φ_α scattering to φ_β and losing an energy slightly larger than E_g is an increasing function of the energy loss.

C. DIRECT AND NONDIRECT TRANSITIONS

In this section we discuss two models for the photoexcitation of a solid: (1) direct transition model, in which conservation of one-electron

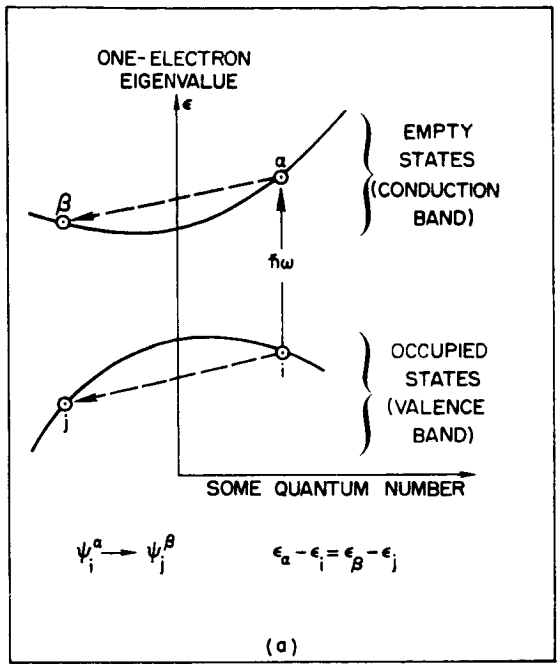

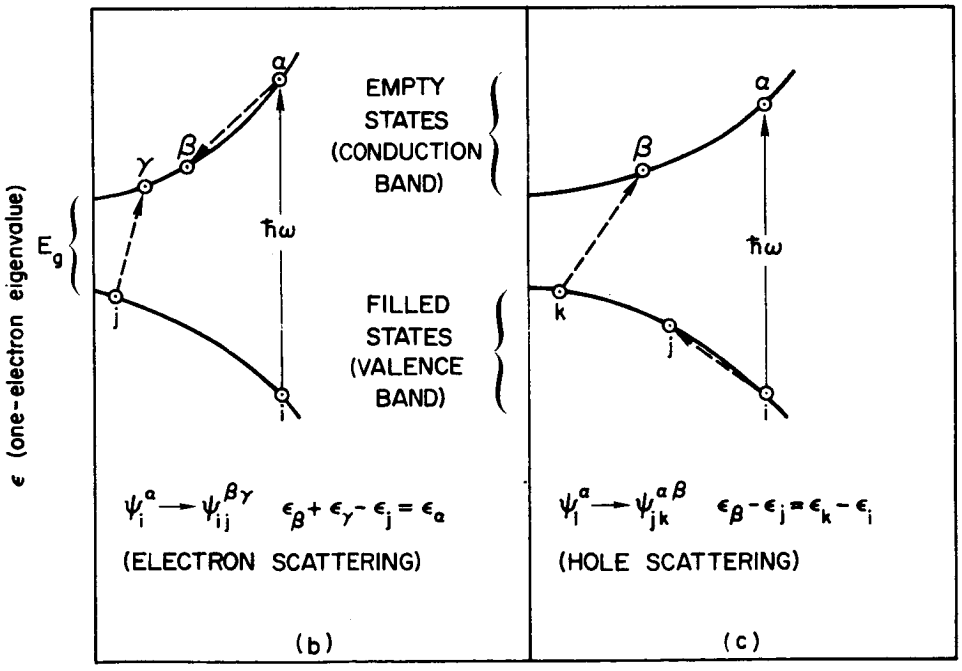

FIG. 2. ELECTRON-ELECTRON SCATTERING. In each case the electron-hole pair, φ_α and φ_i, is created by a photon of energy $\hbar\omega$. (a) One electron-hole pair, φ_α and φ_i, scatters into another, φ_β and φ_j. (b) An electron in state φ_α scatters into another state φ_β and creates an electron-hole pair, φ_γ and φ_j. (c) A hole in state φ_i scatters into another state, φ_j, and creates an electron-hole pair, φ_β and φ_k.

wave vector is an important selection rule, and (2) nondirect transition model, in which conservation of one-electron wave vector is not an important selection rule.

If the system wave function is initially Ψ_{init}, then electromagnetic radiation of frequency ω causes transitions to final states, Ψ_{final}, at a rate

$$w = \frac{2\pi}{\hbar} |\langle \Psi_{init} | \mathcal{H}' | \Psi_{final} \rangle|^2 N(f) \delta(\mathcal{E}_{final} - \mathcal{E}_{init} - \hbar\omega) \tag{13}$$

where $N(f)$ is the density of final states, and $\mathcal{H}'$ is the operator for the electron-radiation interaction, $(1/m)A \cdot p$ (SCHIFF, 1955). If the initial and final wave functions are Slater determinants, then the matrix element in Eq. (13) vanishes if Ψ_{init} and Ψ_{final} differ by more than one pair of orbitals (Sec. B2). If the initial wave function is the Hartree-Fock ground state, ψ_o, then the matrix element is nonzero only for approximate final states of the form ψ_i^α. It follows from Eq. (13) that the transition rate to final states near ψ_i^α is

$$w_{i\alpha} = \frac{2\pi}{\hbar} |\langle \psi_o | \mathcal{H}' | \psi_i^\alpha \rangle|^2 N_c(\alpha) N_v(i) \delta(\epsilon_\alpha - \epsilon_i - \hbar\omega) \tag{14}$$

$N_c(\alpha)$ is the conduction band density of states near φ_α, and $N_v(i)$ is the valence band density of states near φ_i. By virtue of Koopmans' theorem, the change in electronic energy is $\epsilon_\alpha - \epsilon_i$; hence conservation of energy requires that for a photon energy $\hbar\omega$, $\epsilon_\alpha - \epsilon_i = \hbar\omega$. The excitation rate given by Eq. (13) depends on both the density of states and the interaction matrix element. In this section we discuss situations in which one or the other is more important in determining the electronic excitation rate.

1. Direct Transitions

If the solutions to the Hartree-Fock equation are Bloch functions, then each Slater determinant is classified according to its total wave vector $\bar{K} = \sum_{j=1}^{N} \bar{k}_j$. It is a standard result of band theory that if $\bar{K}_i \neq \bar{K}_f$, then $\langle \Psi(\bar{K}_i) | \mathcal{H}' | \Psi(\bar{K}_f) \rangle = 0$ (assuming that the wave vector of the radiation is small in comparison with $\bar{k}_j$). The only allowed transitions satisfy $\Delta\bar{K} \equiv \bar{K}_f - \bar{K}_i = 0$. If the initial and final wave functions

differ by only one pair of orbitals $(\psi_o \rightarrow \psi_i^\alpha)$, then the wave vector for the excited orbital φ_α must equal the wave vector for the orbital φ_i replaced in the initial wave function. Such transitions are known as direct transitions, since on a plot of electron eigenvalue vs wave vector, the eigenvalue for the excited orbital lies vertically above that for the empty orbital. Only those approximate excited states having one-electron eigenvalues separated by a vertical distance of $\hbar\omega$ are optically excited. For the direct transition model, the $\Delta\bar{K} = 0$ selection rule causes the matrix element to vanish for all but a small fraction of the states at an energy $\hbar\omega$ above the ground state energy; hence the final density of states only slightly affects the electron transition rate.

We now discuss features of the photoemission characteristic of direct transitions. The photoemission experiment measures the energy distribution of the photoemitted electrons. For the one-electron eigenvalues shown in Fig. 3, the only allowed excitation for $\hbar\omega_1$ would excite an electron from φ_i to φ_α. If the photon energy is increased

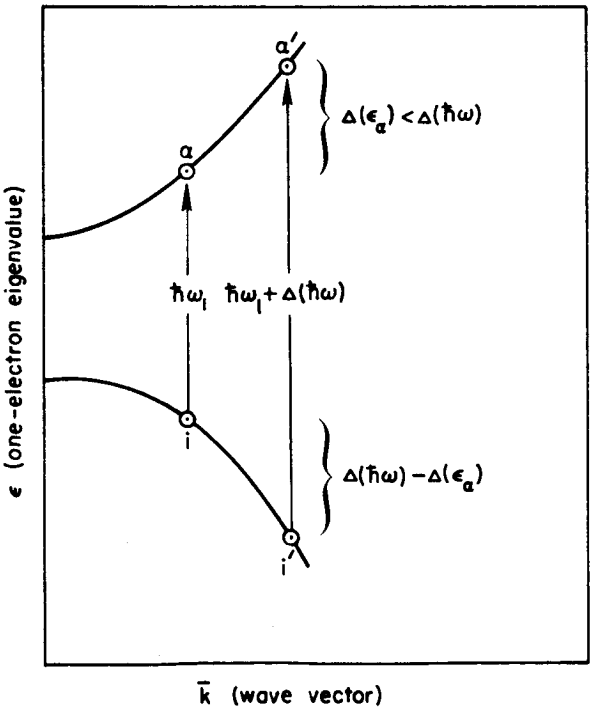

FIG. 3. PHOTOEXCITATION FOR DIRECT TRANSITION MODEL.

by $\Delta(\hbar\omega)$, the eigenvalue of the excited orbital φ_α will, in general, change by an amount unequal to $\Delta(\hbar\omega)$. If the only excitation were that shown in Fig. 3, the energy distribution of the photoemitted electrons would show a peak of electrons moving to higher energy with $\Delta(\epsilon_\alpha) < \Delta(\hbar\omega)$. The rest of $\Delta(\hbar\omega)$ is given to the hole left behind. This movement of a peak of electrons to higher energies with changes in energy unequal to changes in photon energy is characteristic of direct transitions, since it is dictated by the $\Delta\bar{K} = 0$ selection rule.

2. Nondirect Transitions

The photoemission studies referred to in Chapter I concluded that direct transitions are not important for most of the observed transitions. The nondirect and the nondirect constant-matrix-elements models have been proposed to explain much of the photoemission data.

The nondirect (ND) model of electronic excitation assumes that $\Delta\bar{K} = 0$ is not an important selection rule for photoexcitation. This assumption will be valid if

1. The lowest energy solutions to the Hartree-Fock equation are not Bloch functions. This possibility exists since there is no uniqueness theorem for solutions to the Hartree-Fock equation (Sec. A).

2. The electrons or lattice relax in a time comparable to the excitation time. Koopmans' theorem does not apply since the orbitals in the excited state determinant differ from the orbitals in the ground state determinant (Sec. A).

3. A single Slater determinant poorly approximates a stationary state of the system. The electron-electron interaction causes a strong configuration interaction (Sec. B1).

4. An excited state is formed from the ground state determinant by replacing a localized orbital with a Bloch function. For the ground state, an equivalent determinant of localized orbitals can be formed from the determinant of Bloch functions (SEITZ, 1940; KNOX, 1963).

It is also possible (EDEN, 1966) that the Fourier transform of the decaying electric field intensity, $e^{-\alpha x}$, has large amplitudes for $\bar{K} \neq 0$; hence it would allow transitions for $\Delta\bar{K} \neq 0$. For the ND model, the excitation rate to any excited state is still determined by Eq. (13). However, the magnitudes of the densities of states will be more significant in determining the relative strengths of various excitations,

since the matrix element will no longer vanish for most excitations as it does for the direct transition model.

The nondirect constant-matrix-elements (NDCME) model of electronic excitation consists of the ND model and the additional assumption that the matrix elements coupling all initial and final states are equal to a constant. For the NDCME model the relative number of electrons photoexcited to an energy E is

$$n(E) \propto N_c(E)N_v(E - \hbar\omega) \tag{15}$$

where $N_c(E)$ is the conduction band density of states at energy E and $N_v(E - \hbar\omega)$ is the valence band density of states at energy $E - \hbar\omega$. Electron energies are stated relative to the valence band maximum. The energy distribution of the photoexcited electrons given by Eq. (15) follows immediately from Eq. (14) and the assumption of constant matrix elements. Although the following comments are exact only for the NDCME model, they are approximately true for the ND model to the extent that the matrix element in Eq. (14) is a slowly varying function of the initial and final states. If there is a peak in the valence band density of states at energy ϵ_i below the top of the valence band, then there will always be a peak in the energy distribution at an energy $E_p = \hbar\omega - \epsilon_i$. If the photon energy is changed by an amount $\Delta(\hbar\omega)$, then the energy of the peak changes by the same amount $\Delta(\hbar\omega)$. On the other hand, if there is a peak in the conduction band density of states at an energy ϵ_f above the valence band maximum, then there will be a peak in the energy distributions at $E_p = \epsilon_f$ for all $\hbar\omega$.

3. Comparison of Direct and NDCME Models

The characteristics of the direct and NDCME models are compared in Table 1. Most of the entries have been discussed earlier, but the second entry for the direct transition model requires elaboration. Often there are transitions for which the initial or final densities of states are quite large, but the transitions are forbidden by the $\Delta\bar{K} = 0$ selection rule. For some range of photon energy, transitions to this large

TABLE 1. CHARACTERISTICS OF DIRECT AND NONDIRECT TRANSITIONS

Model	Characteristics
Direct Transition ($\Delta\bar{K} = 0$)	Peaks move $\Delta(E_p) \neq \Delta(\hbar\omega)$ Structure appears and disappears
NDCME	Peaks move $\Delta(E_p) = \Delta(\hbar\omega)$ Peaks move $\Delta(E_p) = 0$

density of final states (or from a large density of initial states) are allowed, since the $\Delta\bar{K} = 0$ selection rule becomes satisfied. For this range of photon energy, peaks or shoulders appear in the energy distributions of the photoemitted electrons. This situation is shown in Fig. 4. Even though there is a large final density of states near φ_α, ψ_j^α is not excited for $\hbar\omega_1$ since $\Delta\bar{K} \neq 0$. For $\hbar\omega_2$, ψ_i^α is excited since

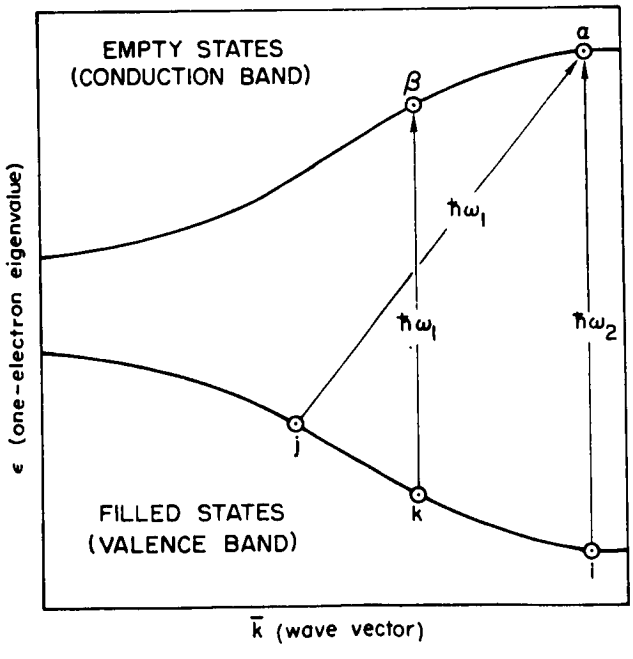

FIG. 4. STRUCTURE WHICH APPEARS AND DISAPPEARS DUE TO DIRECT TRANSITIONS.

$\Delta\bar{K} = 0$. The large density of states for ψ_i^α would cause direct transitions to appear in the energy distributions for $\hbar\omega_2$, even if nondirect transitions dominated the energy distributions for $\hbar\omega_1$. When $\Delta\bar{K} = 0$ again cannot be satisfied, the structure due to transitions to φ_α disappears from the energy distribution. This appearance and disappearance of structure in the energy distributions is characteristic of direct transitions.

D. DENSITY OF STATES ANALYSIS OF PHOTOEMISSION DATA

SPICER (1963) was the first to derive a valence band density of states from photoemission energy distributions. BERGLUND and SPICER (1964a) developed an analysis which determined the electronic density of states from photoemission data when the conduction band density of states is constant. KINDIG and SPICER (1965a) extended this analysis to allow for an arbitrary conduction band density of states. The present form of the density of states analysis is due to EDEN (1966). If the NDCME model is sufficient to explain the photoemission data, then the present method derives the same density of states as does the analysis of KINDIG and SPICER. When the NDCME model is not sufficient to explain the photoemission data, the present method clearly displays the details of the matrix-element-dependent transitions.

The present version of the density of states analysis determines whether or not the NDCME model of electronic excitation is sufficient to explain the photoemission data. The NDCME model is assumed by hypothesis; hence the energy distributions of the photoexcited electrons are given by Eq. (15). As described in detail below, the conduction band and valence band densities of states can then be determined using only a small fraction of the photoemission data. The derived conduction band and valence band densities of states are then used in Eq. (15) to predict all of the photoemission data. By comparing with experiment the predictions of Eq. (15), one is able to determine explicitly whether or not the NDCME model is sufficient to explain the photoemission data. When it is sufficient, the density of states analysis determines the conduction band and valence band densities of states. When it is not sufficient, the

analysis determines the matrix element variation required to explain the photoemission data.

1. Energy Distributions Predicted by NDCME Model

The density of states analysis assumes by hypothesis the NDCME model for electronic excitation. Here we derive the expression for the energy distributions of the photoemitted electrons predicted by the NDCME model; in Sec. D2 we present the details of the density of states analysis.

The NDCME model assumes that the strength of an electronic transition is proportional to the product of the initial and final densities of states. The matrix elements coupling initial and final states are assumed equal to a constant for all transitions conserving energy and zero otherwise. On this model the energy distribution of the photoexcited electrons per absorbed photon is

$$n(E,\hbar\omega) = \frac{N_c(E)N_v(E - \hbar\omega)}{\int_{E_g}^{\hbar\omega} N_c(E)N_v(E - \hbar\omega)dE} \tag{16}$$

where $n(E,\hbar\omega)$ is the density of electrons photoexcited to energy E for a photon energy $\hbar\omega$. N_v and N_c are the valence band and conduction band densities of states. In Eq. (16) $n(E,\hbar\omega)$ is normalized, so that there is one photoexcited electron per absorbed photon.

The energy distribution of the photoemitted electrons differs from the energy distribution of the photoexcited electrons, Eq. (16), for the reasons given below. If the surface of the solid is planar and if there is no scattering, then only half of the photoexcited electrons are initially heading toward the surface. Furthermore, the threshold function (or surface transmission probability), $T(E)$, is the probability that an electron reaching the surface with energy E will escape the solid. For energies below the vacuum level $T(E) = 0$; for energies above the vacuum level it is expected that $T(E)$ will be a smooth function of energy.

Corrections to Eq. (16) due to electron-electron scattering of electrons out of the energy distributions can be approximated. It is

assumed that $e^{-x/L(E)}$ is the probability that an electron that is excited to an energy E at a distance x from the surface will travel to the surface without scattering. We refer to $L(E)$ as the escape depth for electrons at energy E. At a distance x from the surface the intensity of radiation is proportional to $e^{-\alpha x}$, where $\alpha(\hbar\omega)$ is the absorption coefficient for a photon energy $\hbar\omega$. If α is much larger than $1/L$, most of the absorption is close to the surface and relatively few electrons scatter on their way to the surface; if α is much smaller than $1/L$, light reaches far into the crystal and there is a large probability that an electron will be scattered before it reaches the surface. It is readily shown (SPICER, 1961) that the fraction of electrons that are excited to an energy E and reach the surface without scattering is

$$S(E,\hbar\omega) = \frac{\alpha(\hbar\omega)L(E)}{1 + \alpha(\hbar\omega)L(E)} \tag{17}$$

If all scattered electrons are unable to escape the solid (i.e., electron-electron scattered to energies below the vacuum level), the energy distribution of the photoemitted electrons is given by

$$n(E,\hbar\omega) = \frac{T(E)S(E,\hbar\omega)N_c(E)N_v(E - \hbar\omega)}{2\int_{E_g}^{\hbar\omega} N_c(E)N_v(E - \hbar\omega)dE} \tag{18}$$

The minimum energy loss through electron-electron scattering is equal to the band gap (Sec. B2), and the more probable energy losses exceed the band gap. Therefore, Eq. (18) is a reasonable treatment of electron-electron scattering, at least for photon energies within about a band gap above the threshold for photoemission.

We have ignored all effects due to phonon scattering. These effects will be negligible if the mean free path for electron-electron scattering is shorter than the mean free path for phonon scattering. The low yields observed in the present work (1 to 10 percent for high-vacuum-cleaved samples, for example see Sec. A of Chapter IV) indicate that the mean free path for electron-electron scattering is shorter than

the absorption depth (for a quantitative estimate of $L(E)$ see Chapter VII. Sec. B). We find no evidence in the present work for any of the transport effects suggested by KANE (1966a) for silicon.

For the NDCME model of electronic excitation, ϵ_2, the imaginary part of the dielectric function, is simply related to the denominator in Eq. (16) (BERGLUND and SPICER, 1964b)

$$\epsilon_2 = A \int_{E_g}^{\hbar\omega} \frac{N_c(E)N_v(E - \hbar\omega)dE}{\omega^2} \tag{19}$$

where A is an undetermined constant. Also, on the basis of photoemission data alone, the product $T(E)N_c(E)$ cannot be resolved into the two distinct quantities. We therefore define this product as the effective conduction band density of states $N_c^{eff}(E)$. Substituting Eq. (19) into (18) and introducing $N_c^{eff}(E)$ we have

$$n(E,\hbar\omega) = \frac{AS(E,\hbar\omega)N_c^{eff}(E)N_v(E - \hbar\omega)}{2\omega^2\epsilon_2} \tag{20}$$

Finally, we combine terms to form a correction term

$$C(E,\hbar\omega) = \frac{AS(E,\hbar\omega)}{2\epsilon_2\omega^2} \tag{21}$$

so that the energy distribution of the photoemitted electrons is given by

$$n(E,\hbar\omega) = C(E,\hbar\omega)N_c^{eff}(E)N_v(E - \hbar\omega) \tag{22}$$

We conclude this section by discussing two approximations for $C(E,\hbar\omega)$. In the first case $\alpha L \gg 1$. The escape depth is long compared to the absorption depth $(1/\alpha)$ so that most electrons reach the surface without scattering. Then $S(E,\hbar\omega) \approx 1$ and $C(E,\hbar\omega) \propto 1/(\epsilon_2\omega^2)$. Using published optical data for ϵ_2, $C(E,\hbar\omega)$ is determined, and Eq. (22) reduces to

$$n(E,\hbar\omega) \propto \frac{N_c^{eff}(E)N_v(E - \hbar\omega)}{\epsilon_2\omega^2} \tag{23}$$

The second limiting form is used when $\alpha L \ll 1$. For this case the escape depth is short compared to the absorption depth so that most electrons are electron-electron scattered before they reach the surface. Then $S(E,\hbar\omega) \approx \alpha L$ and $C(E,\hbar\omega) \propto \alpha L/(\epsilon_2\omega^2) \propto L/(n\omega)$. The refractive index n is available from published optical data, but we cannot reliably estimate $L(E)$. We therefore include $L(E)$ in the effective conduction band density of states $N_c^{eff'}(E)$ and Eq. (22) reduces to

$$n(E,\hbar\omega) \propto \frac{N_c^{eff'}(E)N_v(E - \hbar\omega)}{n\omega} \tag{24}$$

where $N_c^{eff'}(E) = L(E)T(E)N_c(E)$.

2. Theory of Density of States Analysis

We shall describe the density of states analysis using Eq. (24), which is valid when $\alpha L \ll 1$. If $\alpha L \gg 1$, then the energy distributions are given by Eq. (23) and the analysis which follows must be modified by replacing $n\omega$ by $\epsilon_2\omega^2$. The low yields measured in the present work indicate that most electrons are electron-electron scattered before they reach the surface (for a quantitative discussion see Chapter VII); hence $\alpha L \ll 1$ and Eq. (24) applies.

The density of states analysis determines the valence band density of states in the following manner. If we choose a fixed final state energy $E = E_f$, then in Eq. (24), $N_c^{eff'}(E_f)$ is a constant. For a photon energy $\hbar\omega$, the valence band density of states at an energy $E_f - \hbar\omega$ is proportional to the amplitude of the normalized energy distribution at an energy E_f, and to $n\omega$:

$$N_v(E_f - \hbar\omega) \propto \frac{n\omega}{N_c^{eff'}(E_f)}\, n(E_f,\hbar\omega) \tag{25}$$

In other words, the amplitudes of the energy distributions at only one energy E_f but for all photon energies suffice to determine the relative valence band density of states seen by a final state energy E_f. If we choose another final energy E_f, the relative valence band density of states can again be determined. In general the valence band densities of states seen by different final states will not superimpose since the effective conduction band density of states $N_c^{eff'}(E_f)$ which enters into Eq. (25) is a function of final state energy E_f. The scale factors $1/N_c^{eff'}(E_f)$ are determined by finding the set necessary to make the computed valence band densities of states superimpose. The resulting $N_c^{eff'}(E_f)$ is the effective conduction band density of states. If the valence band densities of states seen by all final states superimpose, one must conclude that the NDCME model is sufficient to explain the photoemission data.

If the shapes of the valence band densities of states seen by any two final states differ, one must conclude that the NDCME model is not sufficient to explain the photoemission data. Although a unique density of states cannot be determined, the general features of the valence band are usually apparent when one compares the valence band densities of states seen by various E_f.

The density of states analysis determines the conduction band density of states in the following manner. If we choose a fixed initial state energy $E_i = E - \hbar\omega$, then in Eq. (24), $N_v(E_i)$ is a constant. For a photon energy $\hbar\omega$, the effective conduction band density of states at an energy $E_i + \hbar\omega$ is proportional to the amplitude of the energy distribution at an energy $E_i + \hbar\omega$ and to $n\omega$

$$N_c^{eff'}(E_i + \hbar\omega) \propto \frac{n\omega}{N_v(E_i)}\, n(E_i + \hbar\omega, \hbar\omega) \qquad (26)$$

where $N_v(E_i)$ is a constant. In other words, the amplitudes of the energy distributions at an energy $\hbar\omega$ above one initial energy but for all photon energies suffice to determine the relative conduction band density of states. If we choose another initial energy E_i, the relative conduction band density of states can again be determined. In general the effective conduction band densities of states seen by different

initial state energies will not superimpose since $N_v(E_i)$, which enters into Eq. (26), is a function of initial state energy E_i. The scale factors $1/N_v(E_i)$ are determined by finding the set necessary to make the effective conduction band densities of states superimpose. The resulting $N_v(E_i)$ is the valence band density of states. If the effective conduction band densities of states seen by all initial states superimpose, one must conclude that the NDCME model is sufficient to explain the photoemission data.

The test for the validity of the NDCME model is therefore very simple and straightforward. One attempts to derive the valence band and conduction band densities of states from the photoemission data. The results must be consistent in that the densities of states derived using various initial and final states must be the same. If the curves superimpose, one must conclude that the density of states model is sufficient to explain the photoemission data. On the other hand, if the densities of states do not superimpose, one must conclude that the density of states model is not sufficient to explain the photoemission data. The amount by which the curves do not superimpose is a quantitative measure of the matrix element variation required to explain the photoemission data. These matrix-element-dependent transitions may be direct transitions or other transitions (ND) for which the matrix elements are not equal to a constant.

We now give a simple example of the density of states analysis, showing the effects of the simultaneous presence of NDCME transitions and matrix-element-dependent transitions. We show in Fig. 5 the valence band and effective conduction band densities of states which might result from the density of states analysis of a typical set of photoemission data. The circles indicate the scale factors used in Eqs. (25) and (26). E_f is the final state energy used to derive the valence band density of states; E_i is the initial state energy used to derive the effective conduction band density of states.

Since most of the curves in Fig. 5 superimpose, the NDCME model explains most of the photoemission data. The amount by which the various curves do not superimpose is a quantitative measure of the variation of the matrix elements coupling initial and final states. The effective

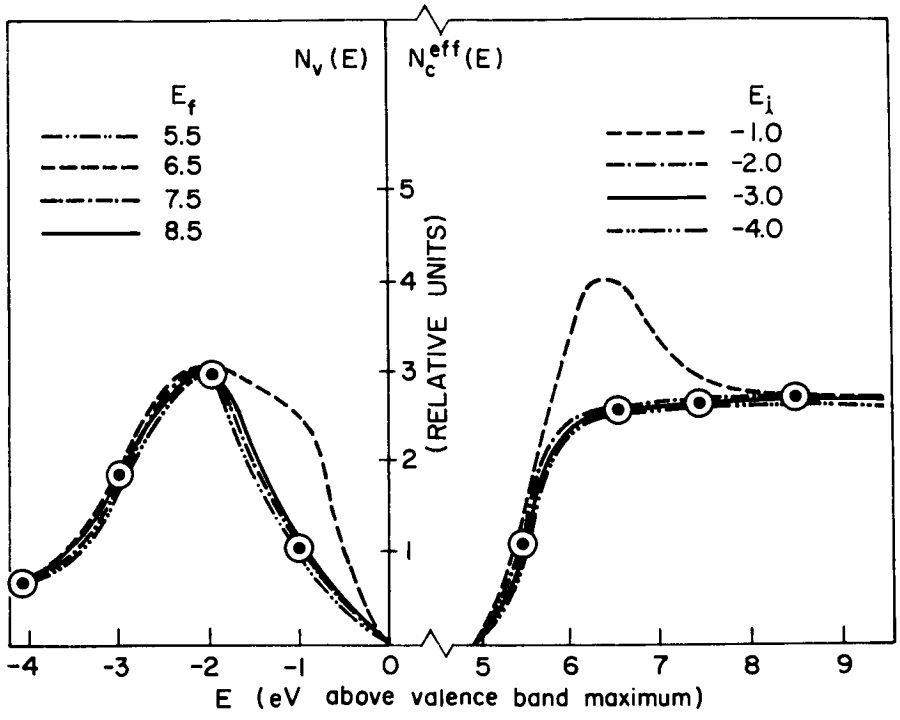

FIG. 5. EXAMPLE OF DENSITY OF STATES ANALYSIS OF PHOTOEMISSION DATA. E_f is the energy of the conduction band state used to derive the valence band density of states $N_v(E)$; E_i is the energy of the initial state used to derive the effective conduction band density of states, $N_c^{eff}(E)$. The points indicate the scale factors used in Eqs. (25) and (26).

conduction band density of states seen by $E_i = -1.0$ eV lies above the other densities of states for $E \approx 6.5$ eV; also, the valence band density of states seen by $E_f = 6.5$ eV lies above the other densities of states for $E \approx -1.0$ eV. This indicates that transitions from initial states near -1.0 eV to final states near 6.5 eV are stronger than the NDCME model predicts. From these data alone it is difficult to determine whether this enhancement is due to direct transitions ($\Delta\bar{K} = 0$) or to nondirect transitions with about a factor of 2 variation in the matrix elements. The matrix-element-dependent transitions observed in the CdTe photoemission data (Chapter IV) can be attributed to direct transitions, since several features of the data are characteristic of direct transitions (see Table 1). On the other hand, the matrix-element-dependent

transitions observed in the CdSe and CdS photoemission data (Chapters V and VI) are not necessarily direct transitions, since the features of the data are not necessarily characteristic of direct transitions.

III. EXPERIMENTAL METHODS

We have measured the photoemission from single crystals of CdTe, CdSe, and CdS cleaved in vacuum. The adsorption of gases onto the freshly cleaved surfaces was minimized by cleaving in high-vacuum chambers at pressures less than 10^{-9} torr. At these pressures several minutes are required before enough gas atoms or molecules strike the surface to form a monolayer. If some of the particles striking the surface do not adhere, a much longer time will be required to form a monolayer. Energy distributions taken a few hours after cleaving were indistinguishable from those taken immediately after cleaving. We conclude that the surface contamination is negligible in the high-vacuum experiments; hence, the high-vacuum photoemission data are characteristic of the individual solids.

For the reasons given below, crystals were also cleaved in a low-vacuum chamber at a pressure of 10^{-4} torr. In the low-vacuum chamber there is no window between the light source and the cleaved crystal; hence measurements can be extended beyond the 12 eV cutoff of the LiF window which seals the high-vacuum chambers. As discussed in Sec. A2, most of the features of the low-vacuum photoemission data are also characteristic of the individual solids.

The electrical measurements of photoemission experiments are (1) the quantum yield, which is the number of photoemitted electrons per absorbed photon, and (2) the energy distribution of the photoemitted electrons. The experimental methods used in this work are discussed in the present chapter; in succeeding chapters the photoemission data are interpreted in terms of the quantum properties of the individual solids.

A. SAMPLE PREPARATION

1. High-Vacuum Experiments

Most of the high-vacuum* experiments used a modified version of the pump station described by KINDIG and SPICER (1965b). A sketch of the modified system is shown in Fig. 6. The new features of this system are:

*Throughout this work, "high-vacuum experiments" refers to experiments performed at pressures less than 10^{-9} torr; "low-vacuum experiments" refers to experiments performed at pressures of about 10^{-4} torr.

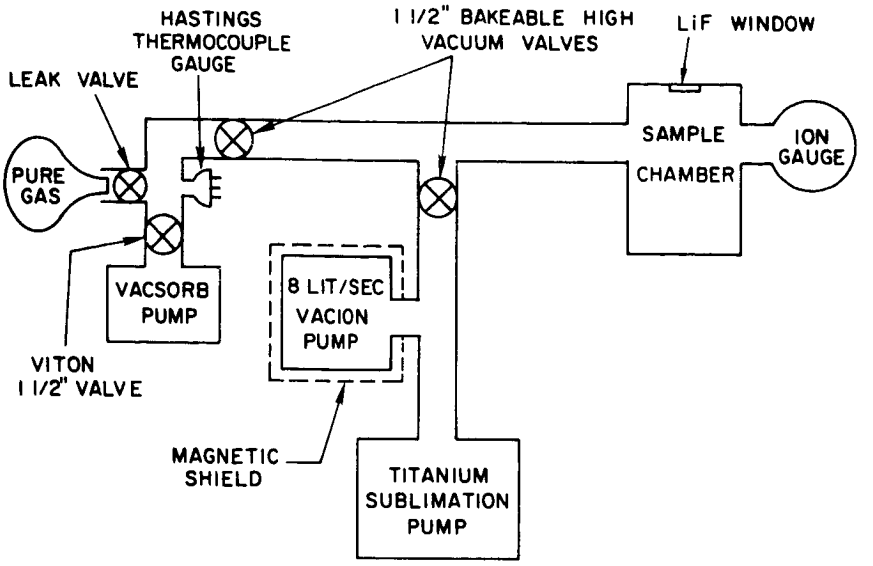

FIG. 6. PUMP STATION FOR HIGH-VACUUM EXPERIMENTS.

1. A high-vacuum valve was inserted between the sample chamber and the high-vacuum pumps.
2. The titanium and VacIon pumps were placed in parallel.
3. A Consolidated Vacuum Corporation (CVC) ionization gauge, model GIC-017, was mounted on the vacuum chamber.
4. A magnetic shield was placed around the magnet used with the VacIon pump.

The first modification prevented the high-vacuum pumps from pumping gases which were introduced into the sample chamber during studies of the effects of these gases on the high-vacuum cleavage. Also, since the pressure within the pumps is maintained below 10^{-9} torr, the gases introduced into the chamber can be rapidly removed by slowly opening the high-vacuum valve. Furthermore, at the conclusion of an experiment, this high-vacuum valve can be sealed before the sample chamber is opened to the atmosphere. With the VacIon and titanium pumps maintained in a high vacuum, the next pumpdown requires less time than if the pumps had been exposed to the atmosphere.

With the second modification, the VacIon pump is more effective since the gas load does not travel through the titanium pump before reaching the VacIon pump, as was necessary when the titanium and VacIon

pumps were in series. In addition, the pressure indicated by the pump is now more representative of the pressure in the sample chamber. In the present system for pressures between about 10^{-4} and 10^{-8} torr measured at the pump during pumpdown, the pressure measured by the CVC ion gauge mounted on the sample chamber was as much as a factor of 10 higher than the pressure at the pump. However, for pressures below about 10^{-8} torr, the two measurements agreed to within a factor of 2.

The sample chamber was not continuously pumped during earlier high-vacuum experiments (KINDIG and SPICER, 1965b). Otherwise, when the magnet used with the VacIon pump was left in place, the magnetic field distorted the energy distributions (see Sec. B4 below). For the present studies we placed a magnetic shield around the magnet used with the VacIon pump and thus prevented distortion of the energy distributions by stray magnetic fields. Hence it was not necessary to remove the magnet for the duration of an experiment, and the sample chamber could be continuously pumped. The shield consisted of a 0.031-in.-thick layer of Netic alloy within a 0.031-in.-thick layer of Conetic Alloy. At the sample chamber, the field due to the magnet was reduced by the shield from about 5 gauss to a value much less than the earth's magnetic field.

With the pump station just described we have used the sample chamber described by KINDIG and SPICER (1965b). Other high-vacuum experiments used a sample chamber described by POWELL (1966). Both vacuum chambers admit ultraviolet radiation through a LiF window which only transmits for photon energies less than 12 eV.

2. Low-Vacuum Experiments

Although it is desirable to cleave in a very good vacuum in order to study properties characteristic of the solid, we were motivated to cleave at a higher pressure for two reasons:

1. The large thresholds for photoemission (6 to 7 eV) measured when the samples were cleaved in high vacuum could be reduced by more than a volt by cleaving at a higher pressure (for details see the initial sections of Chapters IV, V, and VI).

2. In the low-vacuum chamber there is no window between the light source and the cleaved crystal; hence, measurements can be extended beyond the 12 eV cutoff of the LiF window which seals the high-vacuum chamber.

For the low-vacuum experiments we have developed the vacuum chamber shown in Fig. 7. It is constructed of stainless steel and the vacuum seals use neoprene O-rings. Two linear motions are accomplished by a 0.250-in.-diameter stainless steel tubing, which is vacuum sealed to the back flange by a CVC linear feedthrough, model SR-25. We vacuum sealed the end of this tubing to a 0.120-in.-diameter stainless steel rod by a linear feedthrough similar to the CVC feedthrough. The crystal is attached to the center rod which can be moved independently of the outer tubing. This outer tubing pulls the wedge through the incline in a cleaving mechanism similar to the one described by KINDIG and SPICER (1965b). A steel strap holds the center rod in a fixed position while the tubing is moved to cleave the crystal.

To perform a low-vacuum experiment, the low-vacuum sample chamber is sealed to the exit housing of the McPherson vacuum monochromator, model 225. The monochromator's diffusion pump evacuates the sample chamber as well as the monochromator. Since gas from the Hinteregger-type discharge lamp is continuously pumped through the monochromator, and since there is no window between the monochromator and the low-vacuum chamber, a low-vacuum-cleaved sample is exposed to a pressure of about 10^{-4} torr.

In the introduction to this chapter we showed that the high-vacuum photoemission data are characteristic of the individual solids, since the surface contamination is negligible in these high-vacuum experiments. For the materials studied here, most of the features of the low-vacuum data are also characteristic of the individual solids. Features of the high-vacuum data are also observed in the low-vacuum data. However, the low-vacuum data differ from the high-vacuum data in two important ways:

1. For the low-vacuum-cleaved sample the electron affinity is more than a volt lower than for the high-vacuum-cleaved sample. Hence a larger region of the conduction band is exposed in the low-vacuum experiments.
2. The electron-electron scattering is stronger in the low-vacuum-cleaved sample than in the high-vacuum-cleaved sample. This difference in scattering is discussed in detail in Chapter VII, Sec. A.

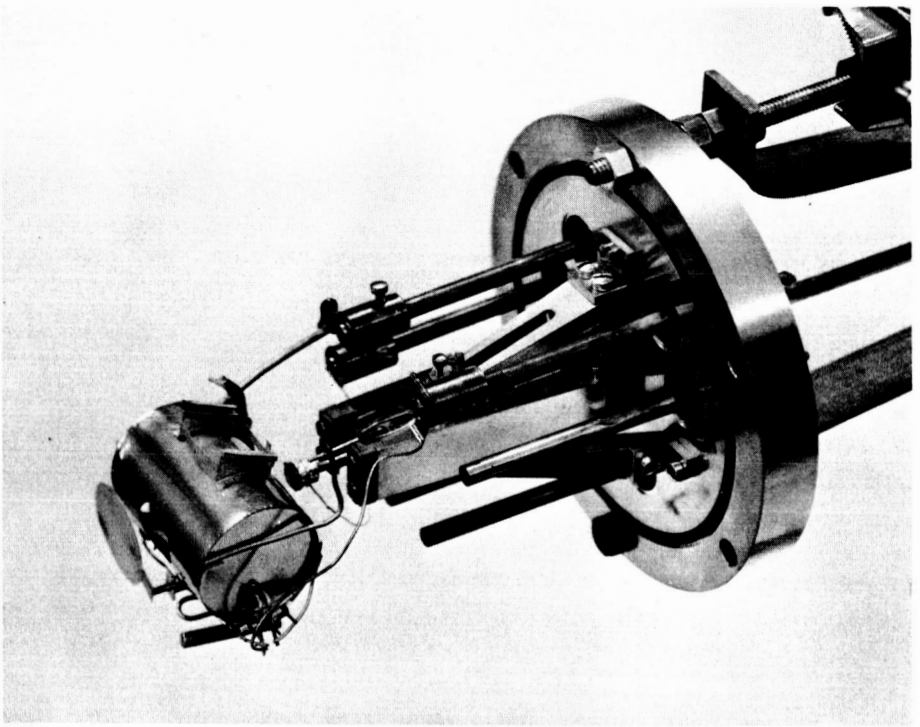

(a) Low-vacuum cleaving mechanism and collector for photoemission measurements

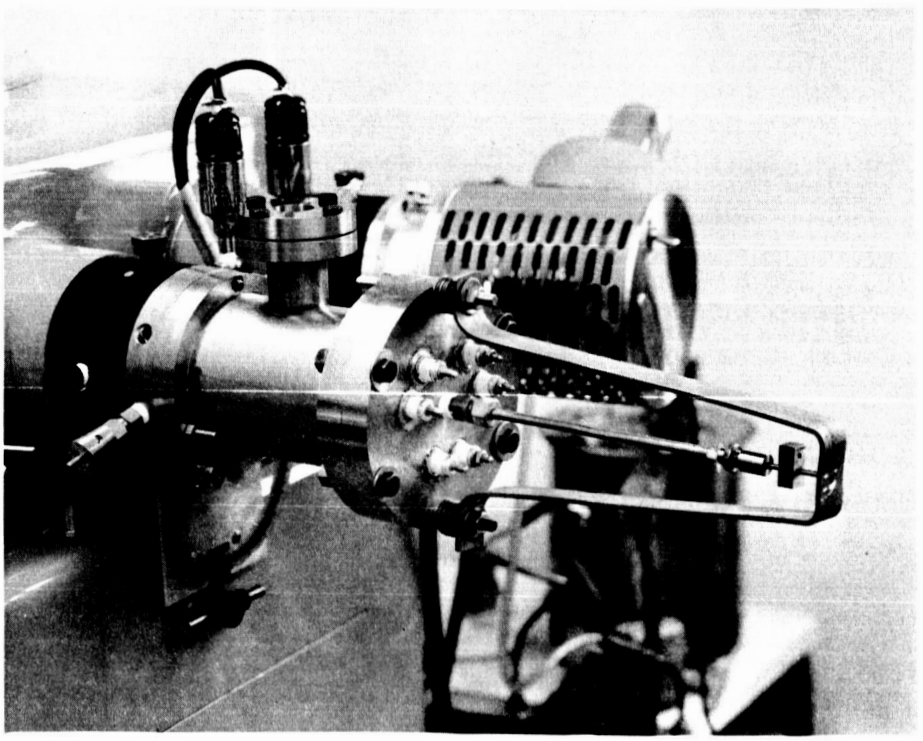

(b) Low-vacuum experiment in progress

FIG. 7. LOW-VACUUM CHAMBER.

3. Sample Mount

The mechanical support used by KINDIG and SPICER (1965a) to support CdS crystals was found inadequate to support CdTe crystals. KINDIG and SPICER used indium to bond a small nickel plate to the crystal surface. When we attempted to use this method to support CdTe crystals, the bond was too weak, and the crystal separated from the nickel plate. The crystal mount shown in Fig. 8 was developed to support the CdTe, CdSe, and CdS crystals studied in this work. This mount also provides electrical contact to the crystals.

The lips of the molybdenum spring clip provide some mechanical support for the crystal. The molybdenum also provides a support for the nickel sheet which is spot welded to the clip. This construction was used because the nickel readily alloys with indium, which bonds to the II-VI materials studied. After evaporating a thick film of indium onto the crystal, a piece of indium was placed between the sample and the spring clip. The entire assembly was placed in an oven at 400 ^{o}C for about 5 minutes in an atmosphere of forming gas. During this time the indium bonded to the crystal and also alloyed with the nickel. After the assembly cooled, it formed an extremely durable structure.

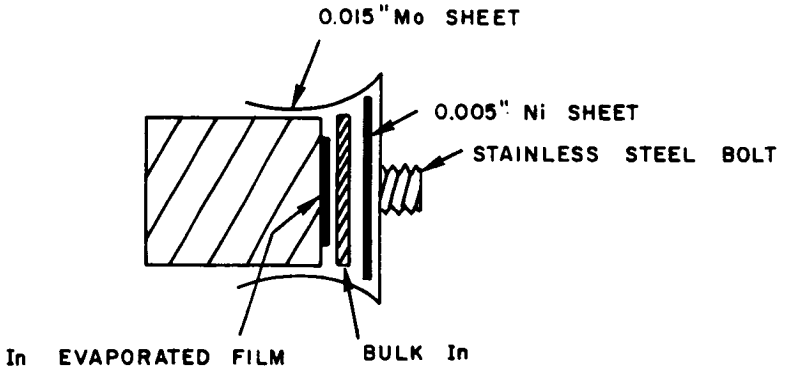

FIG. 8. CRYSTAL MOUNT TO SUPPORT CdTe, CdSe, AND CdS CRYSTALS.

4. Crystal Orientation for Cleavage

The orientation used to cleave wurtzite crystals in a $(1\bar{2}10)$ plane is shown in Fig. 9. An alternate though inferior arrangement is obtained by rotating the crystal by 90^{o} about the C axis. With this

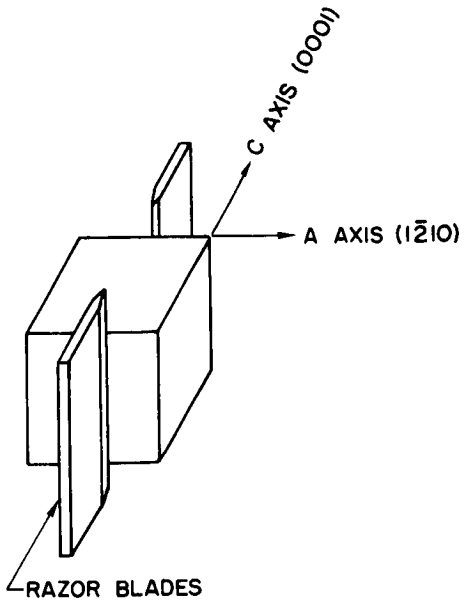

FIG. 9. ORIENTATION FOR CLEAVING WURTZITE CRYSTALS.

latter orientation the crystal is cleaved in a (10$\bar{1}$0) plane. Commercial stainless steel razor blades squeeze the crystal to effect cleavage. Typical crystals were about 1 cm^3, and a typical cleavage removed 2 to 3 mm; three to four cleavages were obtained from each crystal. The wurtzite materials studied in this work are CdSe and CdS. About 50 percent of the cleavages had large regions that were highly perfect to visual inspection; the others usually resulted from attempts to cleave off a slab thinner than 2 mm.

The orientation used to cleave CdTe is shown in Fig. 10. All attempts to cleave CdTe resulted in cleavages having large regions that were highly perfect to visual inspection. The photograph in Fig. 11 shows a typical cleavage.

B. ELECTRICAL MEASUREMENTS

In this section we discuss the principles involved in the photoemission measurements. Details of the electrical circuits used in these measurements have been given elsewhere (BERGLUND, 1964; SPICER and BERLGUND, 1964; KINDIG, 1964). We have used the geometry shown in Fig. 12. Electrical feedthroughs, which are mounted on the back flange of

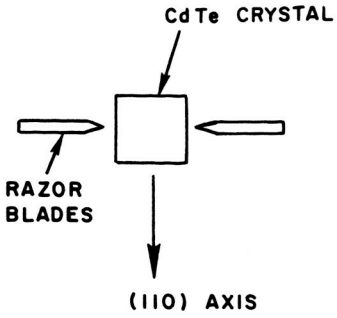

FIG. 10. ORIENTATION FOR CLEAVING CdTe CRYSTALS.

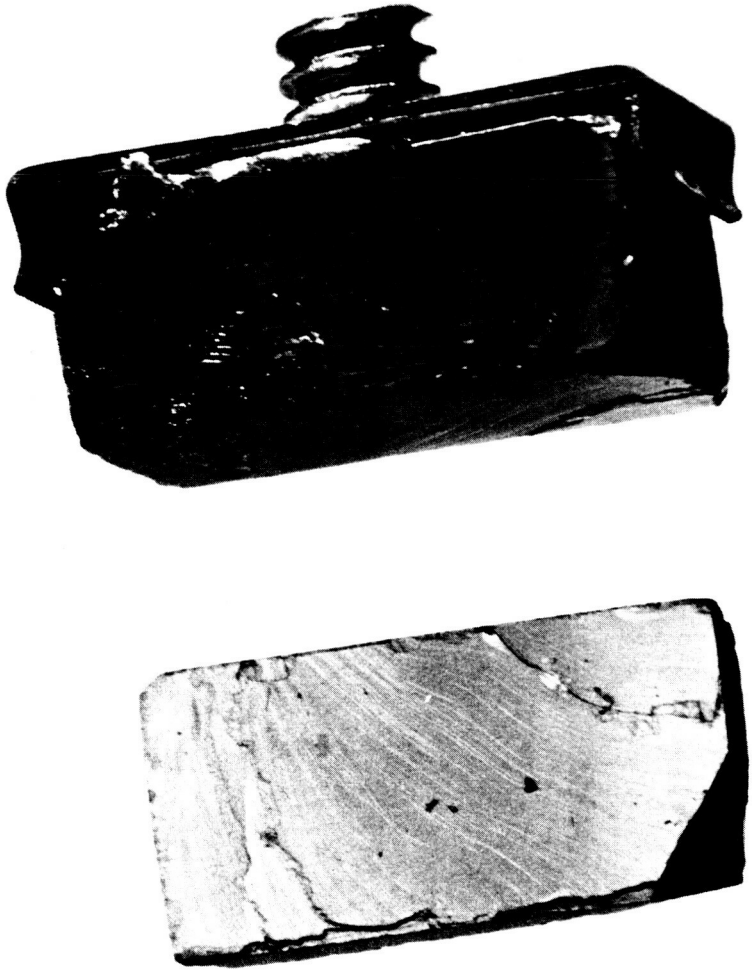

FIG. 11. CRYSTAL MOUNT AND TYPICAL CdTe CLEAVAGE.

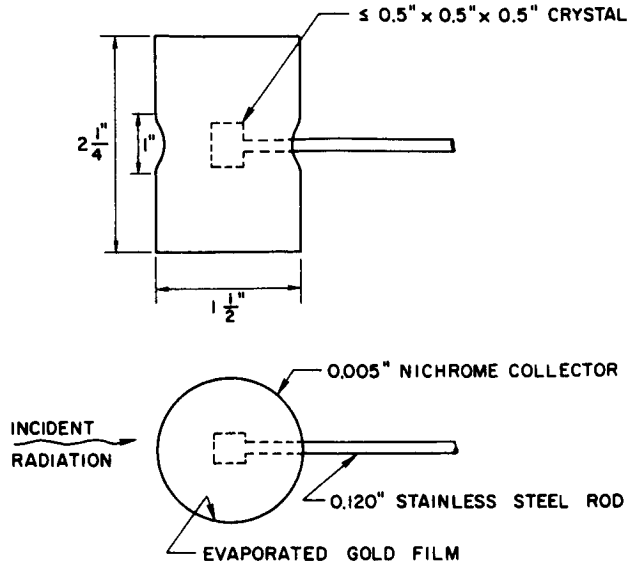

FIG. 12. GEOMETRY FOR PHOTOEMISSION MEASUREMENTS.

the vacuum chambers (see Secs. A1 and A2), support the collector can as well as provide electrical contact to it.

A film of gold is evaporated onto the inside of the collector to provide a uniform collector work function. Earlier studies (KINDIG and SPICER, 1965a) used a film of aluminum on the collector. We find that photoemission from the aluminum (due to light reflected from the crystal) becomes excessive in the low-vacuum experiments. Apparently the pressure of 10^{-4} torr contaminates the aluminum and causes it to have a yield much larger than for pure aluminum. When the gold film was used, the maximum reverse current was never more than about 3 percent of the maximum forward current emitted from the semiconductor.

The phenomenon of photoemission from semiconductors can be understood in terms of the energy level scheme shown in Fig. 13. Radiation incident onto the semiconductor excites electrons from the filled valence band to the empty conduction band. The photoexcited electrons have energies greater than the conduction band minimum but less than an energy $\hbar\omega$ above the top of the valence band. For convenience, we shall state energies relative to the top of the valence band; hence electrons are photoexcited to energies E in the range $E_g < E < \hbar\omega$, where E_g is the semiconductor band gap.

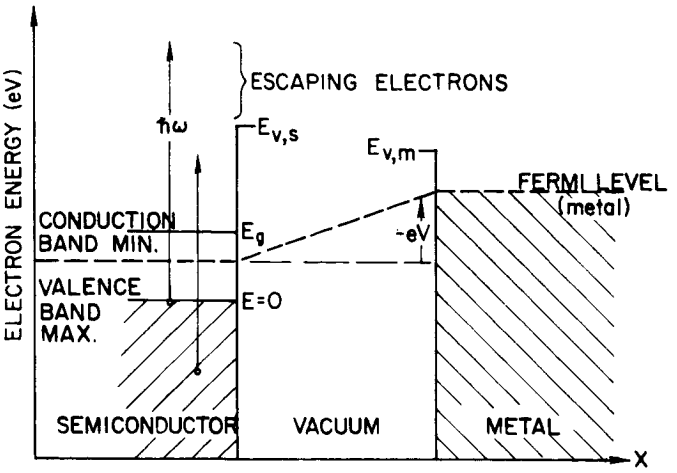

FIG. 13. ELECTRON ENERGY-LEVEL SCHEME FOR A SEMICONDUCTOR PHOTOEMITTER. V is the voltage applied between emitter and collector. E_g is the semiconductor bandgap. $E_{v,s}$ is the vacuum level at the semiconductor surface. $E_{v,m}$ is the vacuum level at the metal surface.

Photoexcited electrons travel to the semiconductor surface and escape into the vacuum if they have energies greater than the semiconductor vacuum level. Electrons having energies less than the semiconductor vacuum level are unable to escape the crystal. If $\hbar\omega$ exceeds the semiconductor vacuum level, some electrons are photoemitted from the solid. Whether or not the photoemitted electrons reach the collector depends upon the voltage V applied between the emitter and the collector. A typical volt-ampere characteristic is shown in Fig. 14, for photons of energy $\hbar\omega$ incident upon the semiconductor. Referring to Figs. 13 and 14, for V negative and sufficiently large, the vacuum level at the collector surface lies above the energies of all photoexcited electrons so that no electrons are able to enter the collector. Those electrons that have escaped the semiconductor encounter a potential barrier in the vacuum and return to the semiconductor. On the other hand, for V large and positive, the vacuum level at the metal surface lies below the energies of all electrons escaping the semiconductor, and all photoemitted electrons are collected.

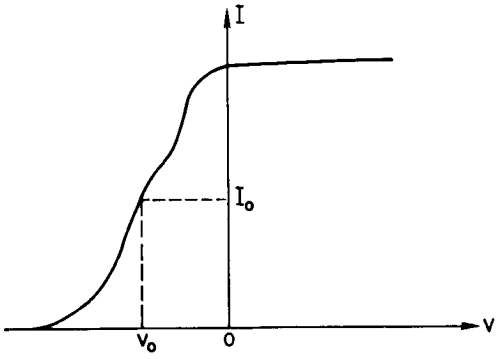

FIG. 14. TYPICAL VOLT-AMPERE CHARACTERISTIC FOR A PHOTODIODE.

1. Measurement of Quantum Yield

The quantum yield is defined as the total number of photoemitted electrons per absorbed photon. One obtains the quantum yield at a given photon energy by measuring the steady photocurrent for a given light intensity and with V large and positive

A Cs_3Sb phototube was used as a standard for measuring light intensity. The relative response of the standard was calibrated using a sodium salicylate film. It was assumed that the conversion efficiency (number of photons at 3.4 eV per photon at $\hbar\omega$) of this phosphor was independent of photon energy in the region $6.0 < \hbar\omega < 12$ eV (ALLISON et al, 1964). The absolute yield of the Cs_3Sb standard was measured at $\hbar\omega = 7.8$ eV using a Reeder thermopile.

Different sodium salicylate films resulted in different calibrations of the relative response of the Cs_3Sb standard (KOYAMA, 1966). One calibration was chosen and used for all high- and low-vacuum CdSe experiments (Chapter V), all high- and low-vacuum CdS experiments (Chapter VI), and the low-vacuum CdTe experiments (Chapter IV). The uncertainty in the response of a sodium salicylate film results in an uncertainty in the yield measurement. Other calibrations of the standard agreed with the present one at $\hbar\omega = 6$ eV but dropped below the present calibration at higher photon energies. The yield reported at $\hbar\omega = 12$ eV may be high by as much as a factor of 2 relative to the yield at $\hbar\omega = 6$ eV. Different calibrations vary smoothly over the range of 6 eV in photon energy, so that the maximum uncertainty in the yield is about 15 percent over a range of 1 eV.

2. Measurement of Energy Distribution of Photoemitted Electrons

Photoemitted electrons have energies between the semiconductor vacuum level and an energy $\hbar\omega$ above the top of the valence band. The distribution in energy of the photoemitted electrons is related to the small-signal conductance of the emitter-collector diode. The energy distributions have been obtained using the ac method described by SPICER and BERGLUND (1964); we now discuss the principles involved in this measurement.

If the applied voltage V_o is such that the current I_o is less than the maximum current, then some of the photoemitted electrons have encountered a potential barrier in the vacuum and have been returned to the emitter. If the applied voltage is increased by a small amount dV, then some energies which had been above the collector vacuum level now are below it. Electrons at these energies are now unable to be collected and are returned to the semiconductor. This situation is shown in Fig. 15. The change in the number of electrons collected per second is dI/e, where dI is the change in current due to the change in voltage dV, and e is the magnitude of the electronic charge. In Fig. 15, $n(E_{v,m})$ is the density of electrons (electrons/photon/eV)

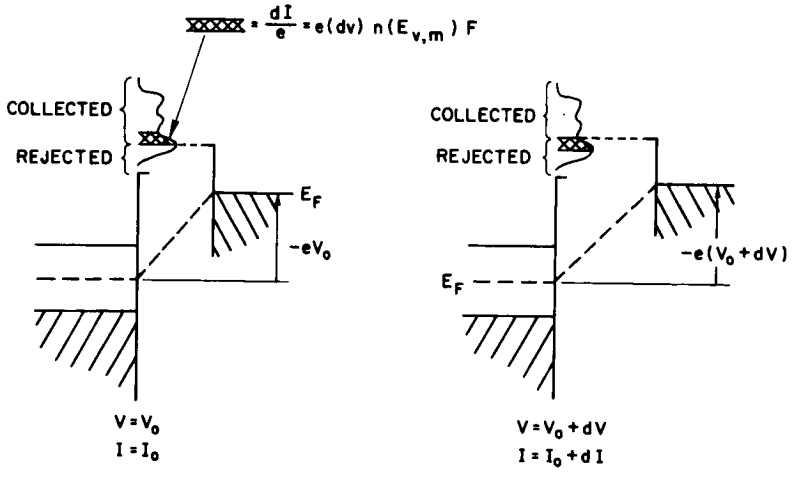

FIG. 15. EFFECT OF A SMALL CHANGE dV IN THE APPLIED VOLTAGE. The status of electrons in the crosshatched section changes from collected to rejected. The change in current is proportional to $n(E_{v,m})$, the density of electrons emitted at the metal vacuum level, and to F, the number of photons per second incident onto the semiconductor.

photoemitted at the energy of the collector vacuum level; F is the number of photons absorbed in the semiconductor per second. The change in the number of electrons collected per second is therefore given by $n(E_{v,m})e(dV)F$. By equating the two expressions, the energy distribution of the photoemitted electrons per absorbed photon is

$$n(E_{v,m}) = \frac{dI}{dV}\frac{1}{e^2F} = \frac{g(V_o)}{e^2F} \tag{27}$$

where $g(V_o)$ is the small-signal conductance of the diode for an applied voltage V_o.

Unless otherwise noted, all energy distributions have been normalized to the quantum yield; the area under a given energy distribution is equal to the quantum yield at that photon energy. The advantage of presenting the data in this way is that after the normalization, the vertical scale of an energy distribution is calibrated in electrons per eV per absorbed photon. Hence we may compare the number of electrons excited to a given final energy for various photon energies.

3. Calibration of Energy Scale

For the V-I characteristic in Fig. 14, the energy distribution in Fig. 16 would be measured. As measured in the laboratory, this curve is the small-signal conductance of the photodiode as a function of the applied voltage V. As explained earlier, this is equivalent to the density of photoemitted electrons as a function of their energy. We are

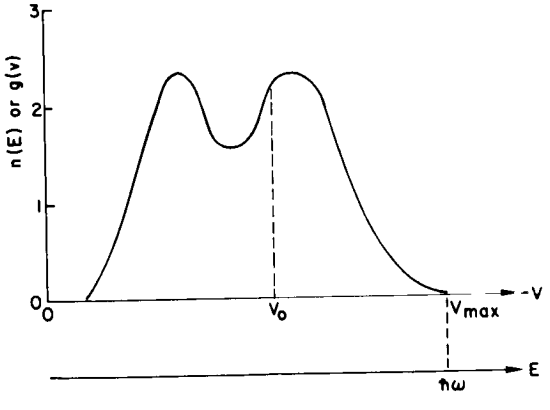

FIG. 16. TYPICAL ENERGY DISTRIBUTION FOR THE VOLT-AMPERE CHARACTERISTIC OF FIG. 14. The calibration of the energy scale is discussed in the text.

able to establish a reference energy level for this curve in the following manner. For a photon energy $\hbar\omega$, the largest energy a photoexcited electron may have is $\hbar\omega$. For convenience, we state electron energies E relative to the top of the semiconductor valence band. Therefore, for an energy distribution measured at a photon energy $\hbar\omega$, the energy of the highest energy electron is $\hbar\omega$. Having established the energy for one point in Fig. 16, the energies at all other points are also determined.

If the conduction and valence bands are not bent significantly within a few absorption depths of the surface, then a check of this calibration is possible if one knows the following: W, the collector work function; V_{max}, the applied potential corresponding to an energy $\hbar\omega$ in Fig. 16; and E_F, the location of the Fermi level within the semiconductor band gap at the surface. It is apparent from Fig. 13 that the relation $\hbar\omega = E_F - V_{max} + W$ must be satisfied.

4. Experimental Uncertainties

The simplified explanation of the photoemission experiment given above has implicitly assumed that the electron trajectory is everywhere parallel to the electric field. We have assumed that the electrostatic potential difference necessary to prevent collection of an electron is equal to its kinetic energy at the semiconductor surface. An ideal geometry for the photoemission experiment would place a small emitter at the center of a spherically symmetric potential field. Then the electric field would be parallel to the electron trajectory and the simplified discussion would be valid. In practice we use cylindrical collectors as shown in Fig. 12. This geometry gives surprisingly good results despite the departure from ideal geometry (for discussion see SPICER and BERGLUND, 1964, and references therein).

Stray magnetic fields distort the energy distributions. If an electron exits normally from the semiconductor surface with a kinetic energy equal to the potential difference between emitter and collector, then it has just enough energy to be collected in the absence of the magnetic field. The electron's trajectory is curved by any stray magnetic field and the electron is not collected. Hence a smaller retarding potential is sufficient to prevent electrons from entering the metal.

Consequently, electrons contribute to the energy distributions at energies below their true energies.

The accuracy of the energy scale calibration is estimated at ±0.2 eV. The principal contributions to this uncertainty are (1) magnitude of ac voltage (0.25 volts, peak to peak), (2) monochromator bandwidth (less than 0.2 eV), and (3) difficulty in locating high-energy intercepts on energy distributions.

IV. PHOTOEMISSION FROM CdTe

In this chapter the data obtained from photoemission studies of CdTe are presented and interpreted. The sharp features of these data are due to direct transitions, which we assign to specific regions of the Brillouin zone.

In Secs. A and B of this chapter, the CdTe quantum yield and energy distributions are presented and discussed. In Sec. C the pseudopotential band structure (COHEN and BERGSTRESSER, 1966) and ultraviolet reflectivity of CdTe (CARDONA and GREENAWAY, 1963) are discussed in light of the photoemission data. Several of the direct transitions observed in the photoemission data are assigned to specific regions of the Brillouin zone, and several reflectivity peaks are given new assignments.

In Sec. D the density of states analysis (Chapter II, Sec. D) is applied to the CdTe photoemission data. We show explicitly that the nondirect constant-matrix-elements (NDCME) model is not sufficient to explain the photoemission data. The degree of failure of the NDCME model provides a quantitative measure of the variation of the matrix elements that cause electronic transitions.

A. QUANTUM YIELD

We present in Fig. 17 the spectral distribution of the quantum yield for a sample of CdTe cleaved in high vacuum and for a sample cleaved in low vacuum. In the low-vacuum experiment the sample was exposed to a pressure of 10^{-4} torr (for details see Sec. A of Chapter III). This resulted in an electron affinity more than a volt lower than for the sample cleaved at a pressure of 10^{-9} torr. The low-vacuum yield is everywhere greater than the high-vacuum yield. This is due to the lower electron affinity for the low-vacuum-cleaved sample. There also resulted a rise in yield for photon energies greater than about 9 eV for the low-vacuum-cleaved sample. We believe that the rise in yield is due to the escape of scattered electrons; however, we defer to Chapter VII a discussion of the evidence for this interpretation.

The two curves of Fig. 17 were measured using different standards for measuring light intensity. The low-vacuum yield was measured using the

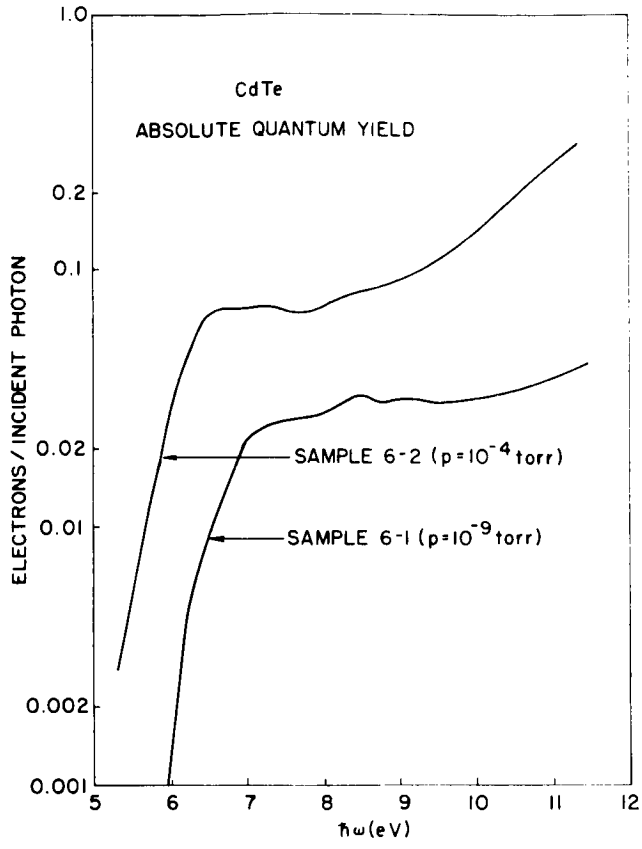

FIG. 17. ABSOLUTE QUANTUM YIELD OF CdTe FOR A PHOTON ENERGY $\hbar\omega$.

same Cs_3Sb standard that was used for both CdSe experiments (Chapter V) and both CdS experiments (Chapter VI). The calibration of this standard is discussed in Chapter III, Sec. B1. For the high-vacuum yield measurement, the relative light intensity was measured using a sodium salicylate film. The absolute yield was measured at $\hbar\omega$ = 7.8 eV using the Cs_3Sb standard.

B. ENERGY DISTRIBUTIONS OF PHOTOEMITTED ELECTRONS

1. Low-Vacuum Experiments

In Figs. 18 through 23 we present energy distributions of the photoemitted electrons for the sample cleaved at a pressure of 10^{-4} torr. Except for $\hbar\omega$ = 16.8 eV and 21.2 eV, all energy distributions have been normalized to the quantum yield. Electron energies are stated relative to the valence band maximum; the calibration of the energy scale was

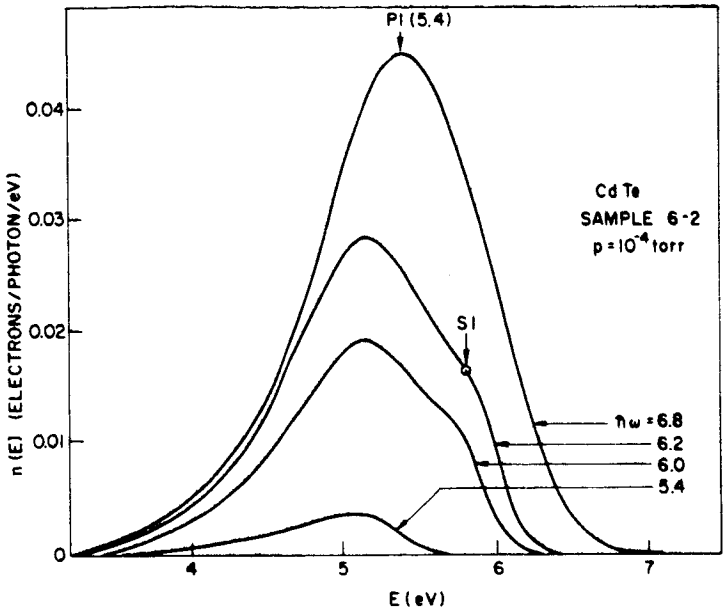

FIG. 18. NORMALIZED ENERGY DISTRIBUTION OF PHOTOEMITTED ELECTRONS FROM CdTe FOR $5.4 \leq \hbar\omega \leq 6.8$ eV. Electron energy E is measured relative to the valence band maximum.

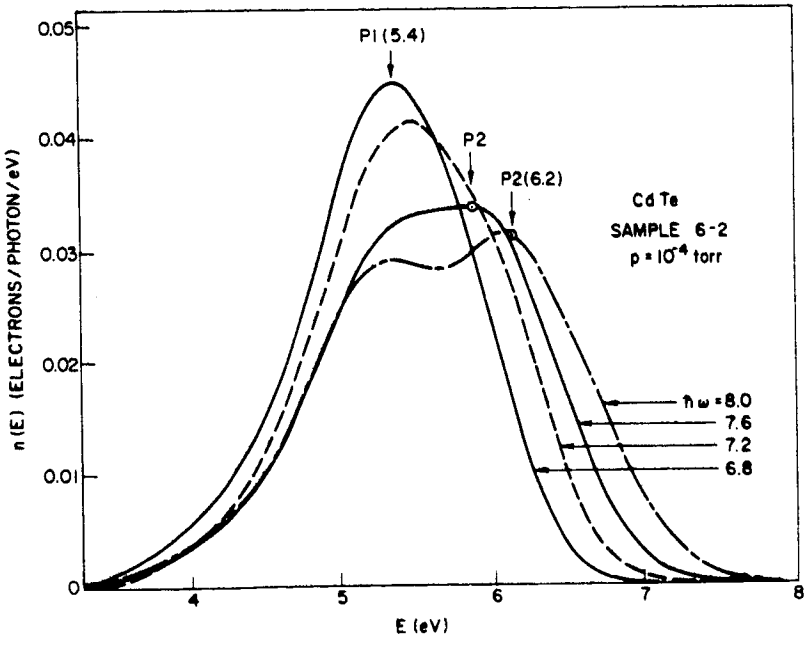

FIG. 19. NORMALIZED ENERGY DISTRIBUTIONS OF PHOTOEMITTED ELECTRONS FROM CdTe FOR $6.8 \leq \hbar\omega \leq 8.0$ eV. Electron energy E is measured relative to the valence band maximum.

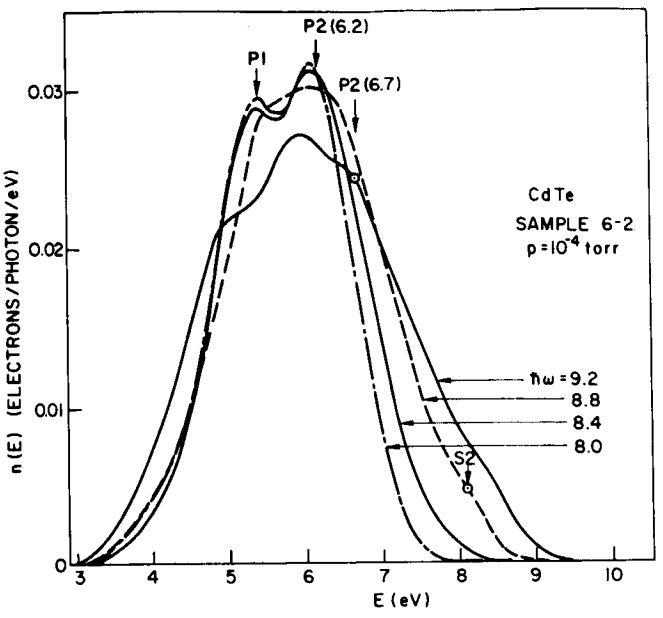

FIG. 20. NORMALIZED ENERGY DISTRIBUTIONS OF PHOTO-EMITTED ELECTRONS FROM CdTe FOR $8.0 \leq \hbar\omega \leq 9.2$ eV. Electron energy E is measured relative to the valence band maximum.

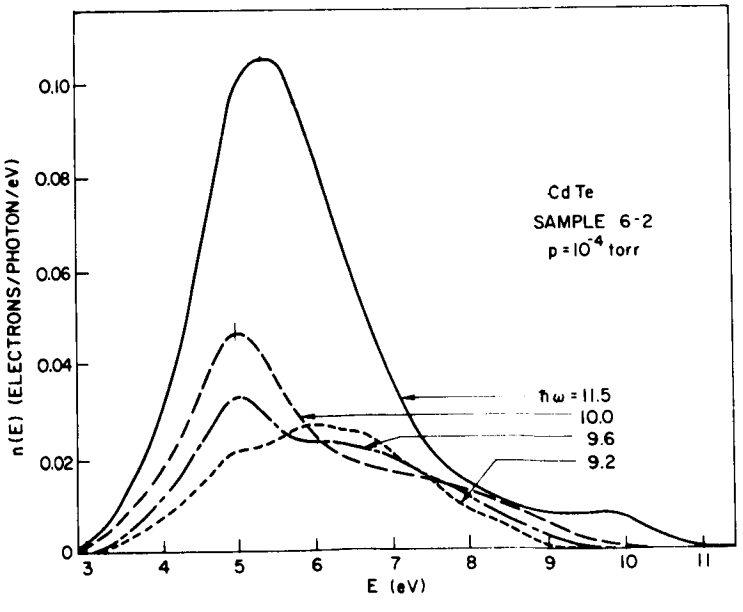

FIG. 21. NORMALIZED ENERGY DISTRIBUTIONS OF PHOTO-EMITTED ELECTRONS FROM CdTe FOR $\hbar\omega \geq 9.2$ eV. Electron energy E is measured relative to the valence band maximum.

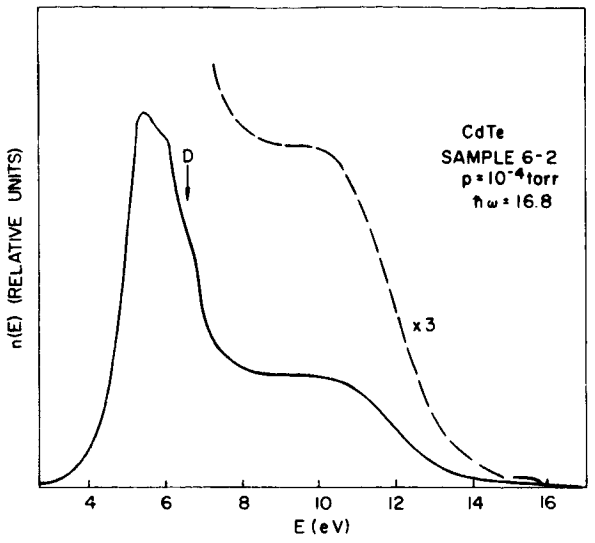

FIG. 22. ENERGY DISTRIBUTION OF PHOTOEMITTED ELECTRONS FROM CdTe FOR $\hbar\omega$ = 16.8 eV. Electron energy E is measured relative to the valence band maximum.

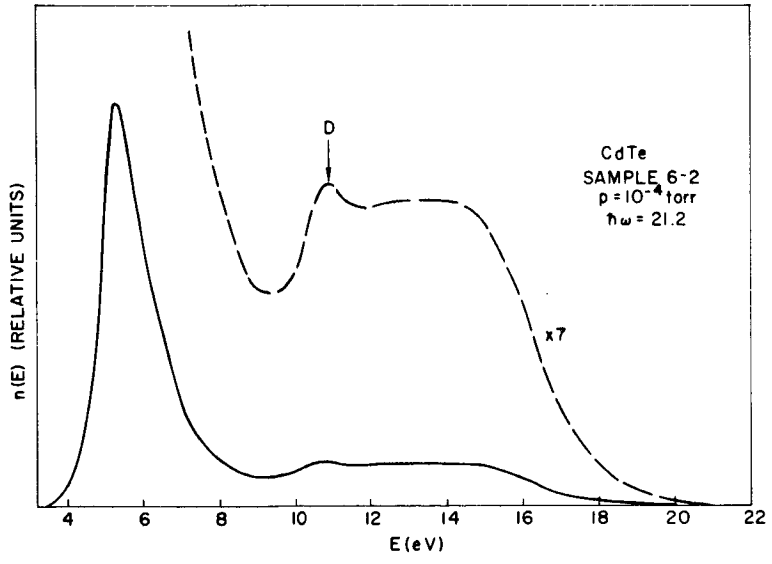

FIG. 23. ENERGY DISTRIBUTION OF PHOTOEMITTED ELECTRONS FROM CdTe FOR $\hbar\omega$ = 21.2 eV. Electron energy E is measured relative to the valence band maximum.

discussed in Sec. B3 of Chapter III. The large number of low-energy electrons appearing in the energy distributions for $\hbar\omega > 9.2$ eV are believed to be electron-electron-scattered electrons; the relevant experimental data are discussed in Chapter VII. Additional data are presented in Appendix A.

There are three prominent features of the energy distributions in Figs. 18 through 21: (1) shoulders S1 and S2 due to transitions from initial states near the top of the valence band, (2) peak P1, which appears at an electron energy of 5.4 eV, and (3) peak P2, which slowly moves to higher energies until it reaches an energy of 6.2 eV. This structure is due to direct transitions; the evidence for this conclusion is presented below. In this section we discuss the qualitative features of the low-vacuum photoemission data; in Sec. C these data will be used to discuss the electronic band structure and ultraviolet reflectivity of CdTe.

For photon energies greater than 5.8 eV, a shoulder S1 appears in the energy distributions (Fig. 18) at high-electron energies. When S1 first appears, the electrons contributing to this shoulder have initial states within a few tenths of a volt of the top of the valence band. The shoulder S1 is only apparent for $5.8 < \hbar\omega < 6.8$ eV, and for most of this interval it remains fixed in energy near 5.8 eV.

For photon energies greater than 8.8 eV, another shoulder S2 appears in the energy distributions (Fig. 20) at high electron energies. When S2 first appears, the electrons contributing to this shoulder also have initial states within a few tenths of a volt of the top of the valence band. The structure in the energy distributions is very similar when the two shoulders appear at $\hbar\omega = 5.8$ and 8.8 eV.

The manner in which the shoulders S1 and S2 appear in the energy distributions cannot be explained by a NDCME model of electronic excitation. The characteristics of NDCME, direct, and other matrix-element-dependent transitions are discussed in Chapter II. S1 cannot be due to NDCME transitions from a peak in the valence band density of states, for then the change in its location would equal the changes in photon energy. S1 also cannot be due to NDCME transitions to a peak at 5.8 eV in the conduction band density of states, for then there would be a peak at 5.8 eV for all $\hbar\omega > 5.8$ eV. We see that this is not the case in Fig. 19

since for $\hbar\omega$ near 8.0 eV, there are peaks of electrons at 5.4 eV and at 6.2 eV, but none at 5.8 eV. We conclude that S1 is due to direct transitions to final states near 5.8 eV. The features of the shoulder S2 are generally the same as those of S1. We conclude that S2 is due to direct transitions to final states near 8.8 eV.

For $\hbar\omega > 6.2$ eV, peak P1 appears in the energy distributions (Figs. 18, 19, and 20) and remains fixed in energy at 5.4 eV. The amplitude of this peak is a maximum for $\hbar\omega = 6.8$ eV, and the peak drops out of the energy distributions for $\hbar\omega > 8.4$ eV. This disappearance is probably due to the small valence-band width. From these data we estimate that the valence band is 3.5 to 4 eV wide.

The peak P1 is primarily due to direct transitions; however, the evidence for this conclusion is not as definitive as the evidence indicating that peak P2 and shoulders S1 and S2 are due to direct transitions. Nonetheless, the manner in which this peak "pops" into the energy distributions and dominates the other structure for $\hbar\omega$ near 6.8 eV is characteristic of direct transitions.

The electrons contributing to peak P1 have not been electron-electron scattered from higher energies. For $\hbar\omega = 6.8$ eV there are no scattered electrons at 5.4 eV, since 5.4 eV is less than a band gap (1.6 eV) below $\hbar\omega$. The minimum energy loss through electron-electron scattering is equal to the band gap (Chapter II, Sec. B2). The disappearance of peak P1 for $\hbar\omega > 8.4$ eV is further evidence that a negligible fraction of this peak is due to scattered electrons. However, the low-energy peak which appears in Fig. 20 for $\hbar\omega > 9.2$ eV is believed to be due to scattered electrons (for a detailed discussion of the effects of electron-electron scattering, see Chapter VII, Sec. A).

For $\hbar\omega > 6.8$ eV, peak P2 appears in the energy distributions. This peak is primarily due to direct transitions. For $6.8 < \hbar\omega < 8$ eV, a range of 1.2 eV, P2 moves from 5.4 to 6.2 eV, a difference of only 0.8 eV. This motion to higher energies with increments in energy less than the increments in photon energy is characteristic of direct transitions (Chapter II). For $8.0 < \hbar\omega < 8.4$ eV, P2 remains at 6.2 eV, and for $\hbar\omega > 8.4$ eV, P2 splits into two peaks, one of which moves to higher energies with increments in energy less than the increments in photon

energy, and another peak which "falls" back to lower energies. The motion of both peaks is characteristic of direct transitions.

In Figs. 22 and 23 we present the energy distributions of the photoemitted electrons for $\hbar\omega = 16.8$ eV and $\hbar\omega = 21.2$ eV. Many of the photoemitted electrons have been electron-electron scattered from higher energies. For $\hbar\omega = 21.2$ eV the peak of electrons labeled D at 10.9 eV is believed to be due to transitions from a high density of states at -10.3 eV in the valence band. We suggest that these valence band states are derived from cadmium 4d states. The location of the d-band is discussed in more detail in Chapter VII, Sec. C.

It is not possible to follow the motion of peak D over a wide range of photon energy to confirm its origin in the valence band; however, if the peak were due to conduction band structure near 10.9 eV, then we would expect to see a peak at 10.9 eV for $\hbar\omega = 16.8$ eV. No such peak is seen in Fig. 22. If the peak at 10.9 eV for $\hbar\omega = 21.2$ eV is in fact due to excitation from valence band states near -10.3 eV, then for $\hbar\omega = 16.8$ eV this peak of electrons should be seen at 6.5 eV. The structure labeled D at 6.5 eV in Fig. 22 is believed to be due to these transitions.

2. High-Vacuum Experiments

In Figs. 24 through 29 we present energy distributions for a sample of CdTe cleaved at a pressure of 10^{-9} torr. The striking difference between these curves and the energy distributions for the sample cleaved in the poor vacuum is that the electron affinity is more than one volt larger for this high-vacuum cleavage than for the sample cleaved in the poor vacuum. Due to the larger electron affinity for the high-vacuum-cleaved sample, much of the structure seen in the low-vacuum energy distributions is not observed here. In addition, the number of electron-electron-scattered electrons appearing in the energy distributions is much smaller than for the low-vacuum-cleaved sample. Much new structure is resolved in the high-vacuum data, since we no longer have the large number of scattered electrons which obscured the structure in the low-vacuum energy distributions for $\hbar\omega > 9$ eV. Although this difference in the number of secondary electrons is not understood in detail, the relevant experimental data are discussed in Chapter VII, Sec. A.

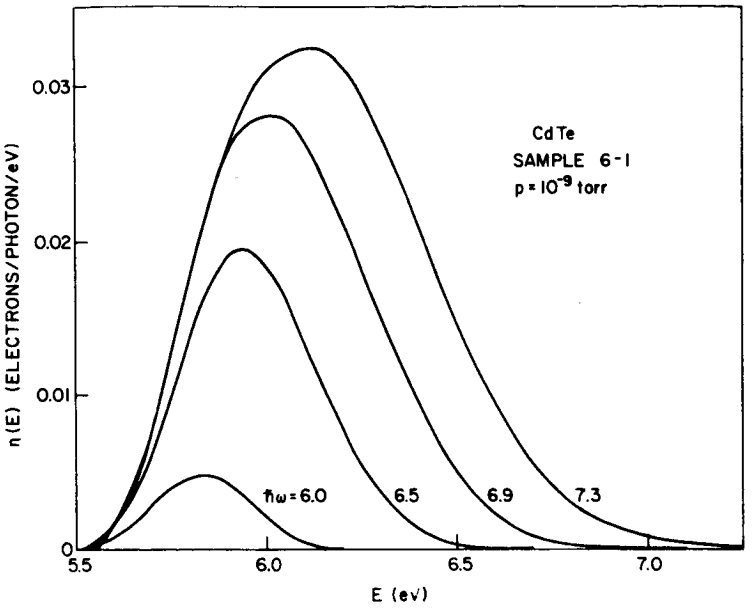

FIG. 24. NORMALIZED ENERGY DISTRIBUTIONS OF PHOTOEMITTED ELECTRONS FROM CdTe FOR $6.0 \leq \hbar\omega \leq 7.3$ eV. Electron energy E is measured relative to the valence band maximum.

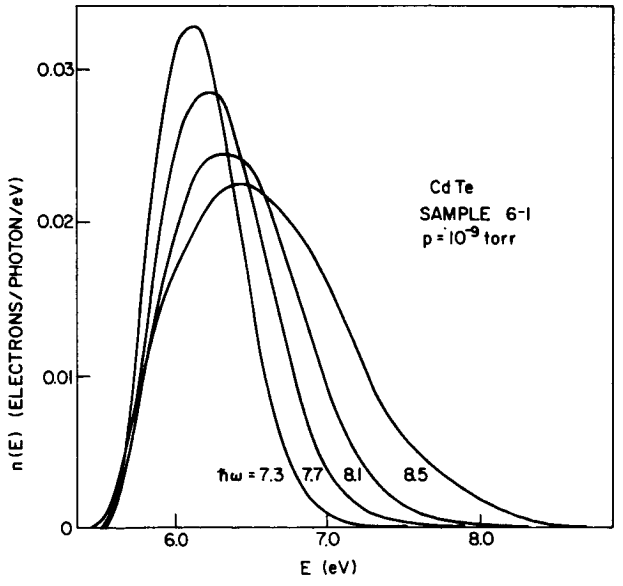

FIG. 25. NORMALIZED ENERGY DISTRIBUTIONS OF PHOTOEMITTED ELECTRONS FROM CdTe FOR $7.3 \leq \hbar\omega \leq 8.5$ eV. Electron energy E is measured relative to the valence band maximum.

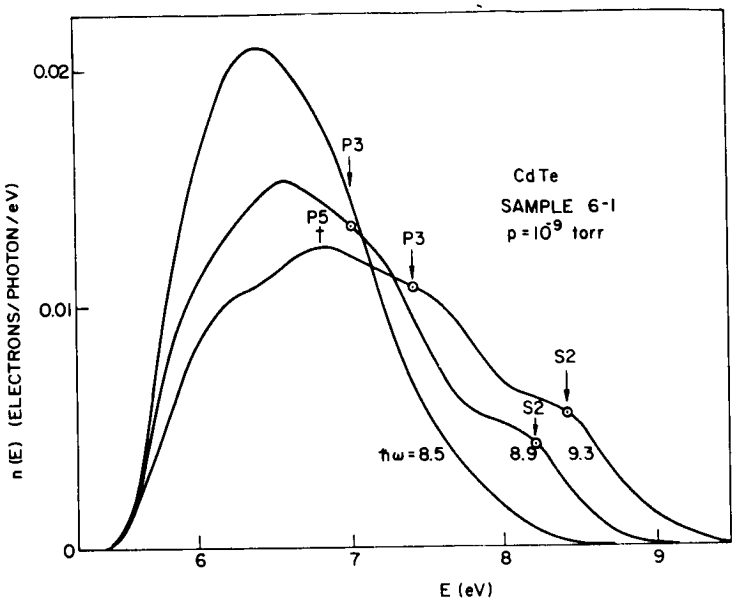

FIG. 26. NORMALIZED ENERGY DISTRIBUTIONS OF PHOTOEMITTED ELECTRONS FROM CdTe FOR $8.5 \leq \hbar\omega \leq 9.3$ eV. Electron energy E is measured relative to the valence band maximum.

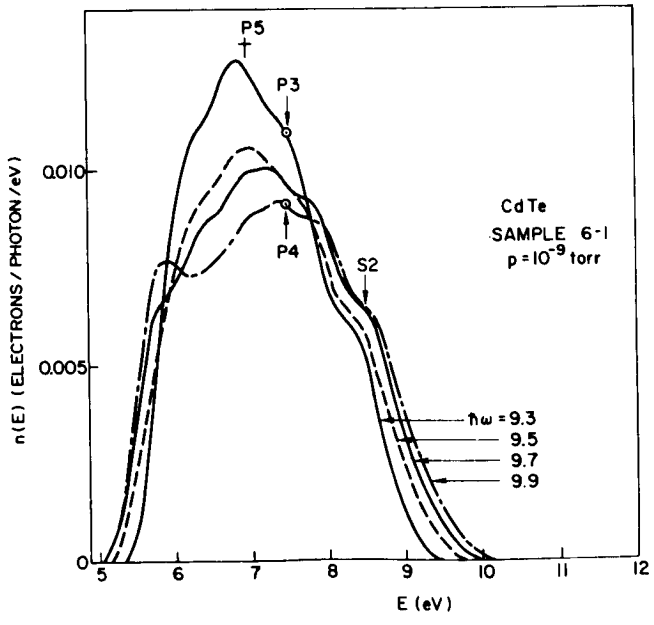

FIG. 27. NORMALIZED ENERGY DISTRIBUTIONS OF PHOTOEMITTED ELECTRONS FROM CdTe FOR $9.3 \leq \hbar\omega \leq 9.9$ eV. Electron energy E is measured relative to the valence band maximum.

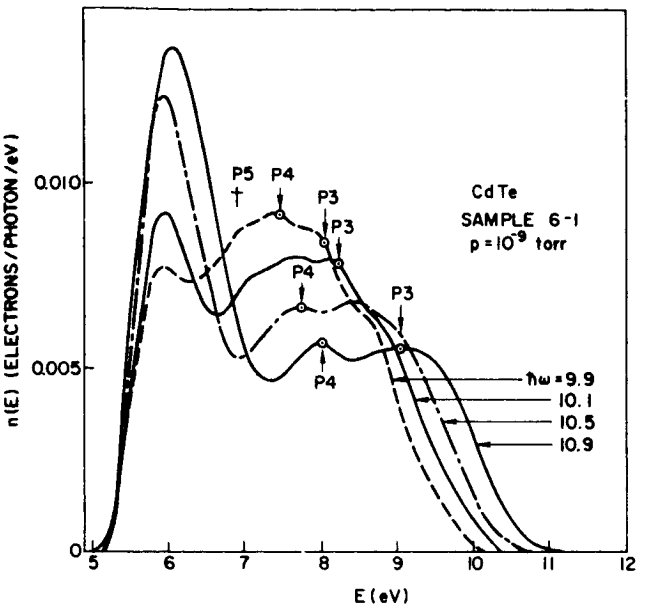

FIG. 28. NORMALIZED ENERGY DISTRIBUTIONS OF PHOTOEMITTED ELECTRONS FROM CdTe FOR $9.9 \leq \hbar\omega \leq 10.9$ eV. Electron energy E is measured relative to the valence band maximum.

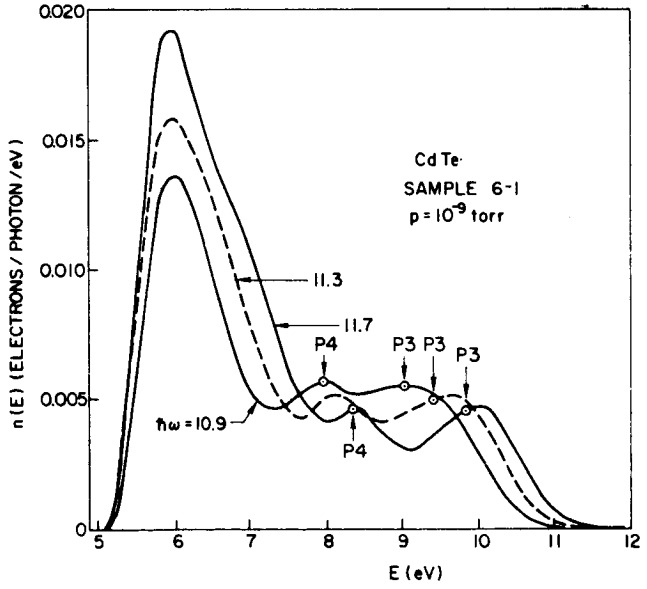

FIG. 29. NORMALIZED ENERGY DISTRIBUTIONS OF PHOTOEMITTED ELECTRONS FROM CdTe FOR $\hbar\omega \geq 10.9$ eV. Electron energy E is measured relative to the valence band maximum.

Structure due to both direct transitions (shoulder S2, peak P4) and NDCME transitions (peak P3) is observed in the high-vacuum energy distributions. The nature of the transitions causing other structure (peak P5) is not certain. In this section we discuss the qualitative features of the photoemission data; in Sec. C these data will be used to discuss the electronic band structure and ultraviolet reflectivity of CdTe.

For photon energies greater than 8.7 eV, a shoulder S2 appears at high electron energies in the energy distributions (Figs. 26 to 28). When S2 first appears the electrons contributing to this shoulder have initial energies within a few tenths of a volt of the top of the valence band. This shoulder moves to higher electron energies only slightly with increasing photon energy, and it is never more than a few tenths of a volt away from 8.4 eV. This shoulder S2 has the same features as the shoulder S2 observed in the low-vacuum experiment (Fig. 20). It appears at the same photon energy, and it has about the same shape. As discussed in Sec. B1, the features of S2 are characteristic of direct transitions.

Both direct and NDCME transitions are observed in the same high-vacuum energy distributions. P3 appears for $\hbar\omega > 8.5$ eV (Figs. 26 to 29), and the energy of this peak is approximately given by

$$E = \hbar\omega - 1.9 \text{ eV} \tag{28}$$

The motion of a peak in accordance with Eq. (28) is characteristic of NDCME transitions from a peak at -1.9 eV in the valence band density of states. The motion in accordance with Eq. (28) indicates that conservation of $\bar{K}$ is not an important selection rule for the transitions associated with peak P3.

Peak P4 appears for $\hbar\omega > 9.5$ eV (Figs. 27 to 29). The energy of this peak is approximately given by

$$E = 0.5\ \hbar\omega + 2.5 \text{ eV} \tag{29}$$

The motion of a peak in accordance with Eq. (29) is characteristic of direct transitions. It is apparent in Fig. 29 that peak P4 is moving much more slowly than peak P3 since the valley between the two peaks is deepening as the photon energy increases. Peak P3 is "walking away" from

peak P4. This is a striking example of the simultaneous presence of direct and NDCME transitions in the same sample for the same photon energies.

The structure discussed above can be separated into distinct portions due to direct and NDCME transitions. The nature of the transitions causing peak P5 is not as clear; however, its motion indicates that it is at least partially due to direct transitions. After moving to higher energies for $\hbar\omega < 9.5$ eV, P5 splits into two peaks, one of which (P5) remains at $E = 6.9$ eV, and one (P4) which moves to higher energies in accordance with Eq. (29). As discussed above, peak P4 is due to direct transitions; the portion which remains at 6.9 eV may be due to NDCME transitions to final states near 6.9 eV. For $\hbar\omega > 10.1$ eV, P5 drops out of the energy distributions. This is probably due to the small valence-band width. From these data we estimate that the valence band is 3.5 to 4.0 eV wide.

The peak of low-energy electrons appearing in the energy distributions for $\hbar\omega > 9.7$ eV is believed to be due to secondary electrons. A stationary peak lying just above the vacuum level is characteristic of scattered electrons (APKER, 1953; SPICER, 1961; BERGLUND and SPICER, 1965). For a semiconductor, the scattering peak cannot appear until $\hbar\omega$ exceeds the vacuum level by at least the band gap (for further details see Chapter VII, and Sec. B2 of Chapter II).

C. DISCUSSION OF BAND STRUCTURE AND REFLECTIVITY

In this section we use the photoemission data presented in Sec. B to determine the energies of the initial and final states for several of the strong electronic transitions observed in the optical data. The present work provides the absolute energies of several levels in the CdTe band structure. Most of our values lie within ~ 0.5 eV of the pseudopotential band structure calculated by COHEN and BERGSTRESSER (1966), hereafter referred to as CB. However, we find that the valence band is not as flat as predicted by the pseudopotential band structure, and we suggest a possible explanation for this disagreement. By correlating structure in the reflectivity with structure in the photoemission data, we compare our interpretation of the photoemission and optical data with the general

interpretation of the reflectivity suggested for all zinc blende materials. We find that several of the usual assignments of structure in the reflectivity are not valid for CdTe. On the basis of the photoemission data we propose new assignments for this structure.

It is important that the reader understand the spirit in which we determine energies of symmetry points in the Brillouin zone. Since a large volume in $\bar{k}$-space is necessary for a sizable electronic transition probability, electronic transitions take place in a large volume about a symmetry point. Hence the energy of the final state (or initial state) for an electronic transition associated with a symmetry point is not necessarily equal to the energy of the symmetry point itself. For silicon, KANE (1966b) has analyzed the distribution in $\bar{k}$-space of contributions to $\epsilon_2(\omega)$, the imaginary part of the dielectric function, and finds that peaks in $\epsilon_2(\omega)$ are poorly described by contributions from the symmetry points at Γ, X, and L. Nevertheless, KANE finds that the optical gaps at Γ, X, and L in silicon are fairly close in energy to the three prominent peaks in $\epsilon_2(\omega)$.

In the photoemission data for CdTe we find structure associated with various symmetry points. In each instance the identity of the symmetry point involved is determined by correlating the photoemission data with reflectivity data (CARDONA and GREENAWAY, 1963, hereafter referred to as CG) and a pseudopotential band structure (CB). We then deduce the energies at the symmetry point by assuming that the energies of the initial and final states for the strong electronic transition (as determined by photoemission data) are equal to the energies at the symmetry point. If this assumption is in error (as it must be to some extent), then the energy gap at the symmetry point is not equal to the photon energy of the strong electronic transition probability. This equality has been assumed in most energy band calculations.

When it first appears for $\hbar\omega > 5.8$ eV, the high-energy shoulder S1 in the low-vacuum energy distributions (Fig. 18) has initial states near the top of the valence band at Γ_{15}^{v}. The calculation of CB shown in Fig. 30 suggests that these transitions are to conduction band states near Γ_{15}^{c}. Therefore the photoemission data locate the conduction band state

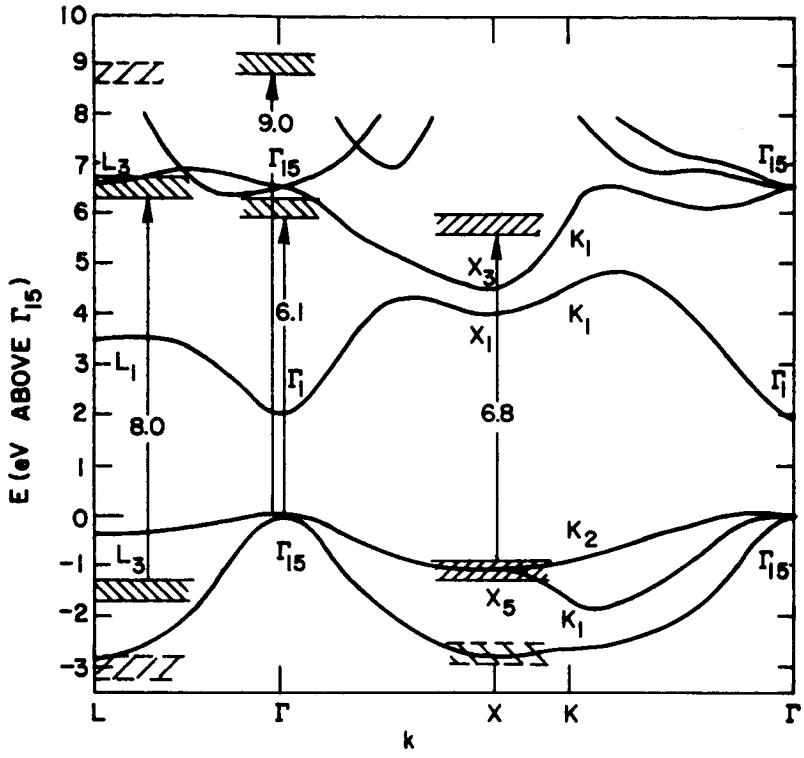

FIG. 30. COMPARISON OF PHOTOEMISSION RESULTS FOR CdTe AND THE PSEUDOPOTENTIAL BAND STRUCTURE CALCULATED BY COHEN AND BERGSTRESSER (1966). The solid lines are the calculated bands: the crosshatched areas indicate states located experimentally. For this figure alone, the effects of spin-orbit splitting of the valence band have been subtracted out of the experimental results.

Γ_{15}^{c} at 5.8 eV above Γ_{15}^{v}. CB calculate* a $\Gamma_{15}^{v} - \Gamma_{15}^{c}$ separation of 6.3 eV, 0.5 eV larger than our experimental value.

CG assigned the small reflectivity peak at 5.2 eV (E_o' in Fig. 31) to $\Gamma_{15}^{v} - \Gamma_{15}^{c}$ transitions. This assignment is not consistent with the photoemission data since transitions to Γ_{15}^{c} only occur for $\hbar\omega \geq 5.8$ eV.

*COHEN and BERGSTRESSER (1966) fit their pseudopotential band structure to experimental values which were corrected for spin-orbit splitting of the valence band. In the text we have added to the calculated values the effects of this spin-orbit splitting by raising the uppermost of the spin-orbit-split levels at Γ_{15}^{v} by 0.3 eV relative to its position in the absence of spin-orbit splitting, and by splitting the L_3^{v} levels +0.3 and -0.3 eV relative to their position in the absence of spin-orbit splitting.

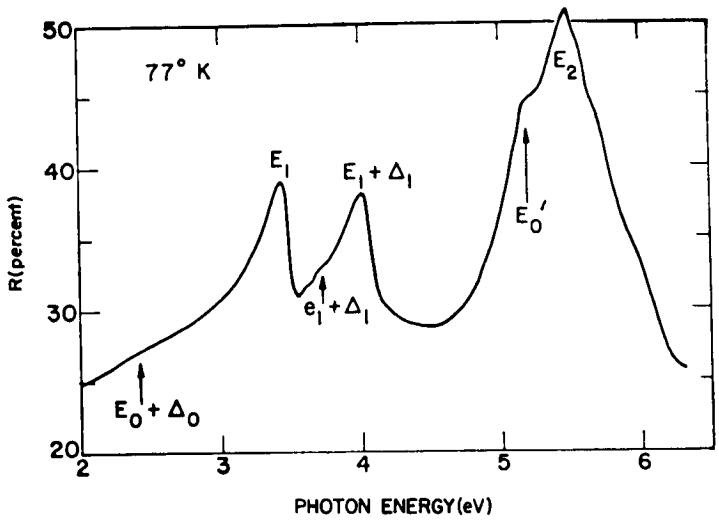

FIG. 31. CdTe REFLECTIVITY MEASURED BY CARDONA AND GREENAWAY (1963) FOR $2 < \hbar\omega < 6$ eV.

Rather we suggest that structure which CG observed in the reflectivity near 5.7 or 6.0 eV (Fig. 31) is due to $\Gamma_{15}^{V} - \Gamma_{15}^{C}$ transitions.

When it first appears for $\hbar\omega > 8.7$ eV, the high-energy shoulder S2 in both high- and low-vacuum energy distributions (Figs. 20 and 26) has initial states near the top of the valence band at Γ_{15}^{V} and final states near 8.7 eV. The final states for these transitions are probably near either Γ_1 or Γ_{12}. The photoemission data therefore locate either Γ_1 or Γ_{12} at 8.7 eV. CB have not published levels above 8 eV, but extending their curves (Fig. 30), one would estimate that Γ_1 lies at about 9 eV. The reflectivity (Fig. 32) is dropping sharply in this region but there is a slight peak d_1 which begins near 8.5 eV and peaks near 10 eV. The beginning of this peak near 8.5 eV corresponds to the appearance of S2 in the energy distributions for $\hbar\omega \geq 8.7$ eV.

This d_1 reflectivity peak was assigned by CG to transitions from d-bands. PHILLIPS (1964) finds this assignment unlikely and has assigned this reflectivity peak to $L_3^V - L_1^C$ transitions. For $\hbar\omega = 10$ eV, S2 is located at 8.5 eV (Figs. 27 and 28). If Phillips' interpretation is correct, then the photoemission data locate L_1^C at 8.5 eV in the conduction band and L_3^V at -1.5 eV in the valence band.

We showed in Sec. B2 that peak P4 in Figs. 26 to 29 is due to direct transitions, since it moves in accordance with Eq. (29). For $\hbar\omega$ = 12 eV, P4 is located at 8.5 eV. Since we have just located L_1^c at 8.5 eV, we suggest that the initial states for P4 are also at L for $\hbar\omega$ = 12 eV. The photoemission data therefore locate an L valence band state (probably L_1^v) at -3.5 eV.

We showed in Sec. B1 that peak P1 at 5.4 eV (Figs. 18, 19 and 20) is due to direct transitions. The amplitude of P1 is a maximum for $\hbar\omega$ = 6.8 eV and, for this same photon energy, there is a peak in the reflectivity (Fig. 32). We suggest that these transitions are to final states near X_3 from initial states near X_5. The photoemission data therefore locate X_3 at 5.4 eV in the conduction band, and X_5 at -1.4 eV in the valence band. CB calculate X_5 at -1.4 eV in excellent agreement with the photoemission data. However, they calculate X_3 at 4.2 eV, which disagrees with our value of 5.4 eV. We also suggest that for $\hbar\omega$ near 8.4 eV (Fig. 20), peak P1 is due to transitions to final states near X_3 from initial states near X_1^v. The photoemission data therefore locate X_1^v at about -3.0 eV, close to the value of -3.2 eV calculated by CB. For $\hbar\omega > 8.4$ eV, P1 drops out of the energy distributions due to small valence-band width.

In Sec. B1 we showed that peak P2 is also due to direct transitions. The ordering of the conduction-band levels calculated by CB (Fig. 30) suggests that P2 is due to transitions to conduction band states near L_3^c. The photoemission data therefore locate L_3^c at 6.2 eV. For $\hbar\omega$ = 8 eV, P2 is due to transitions from initial states at -1.8 eV to final states at 6.2 eV. Corresponding to this structure in the photoemission data there is a peak in the reflectivity at 7.6 eV. This reflectivity peak has been assigned by CG to $L_3^v - L_3^c$ transitions. If this assignment is correct, the photoemission data locate L_3^v at -1.8 eV. This value is close to our earlier estimate of -1.5 eV based on the shoulder in the energy distribution S2 and the d_1 reflectivity peak. Our location for L_3^c (6.2 eV) is close to the value of 6.3 eV calculated by CB; however, our location for L_3^v (-1.8 eV) is in marked disagreement with the calculation by CB (-0.4 and -1.0 eV, spin-orbit splitting included).

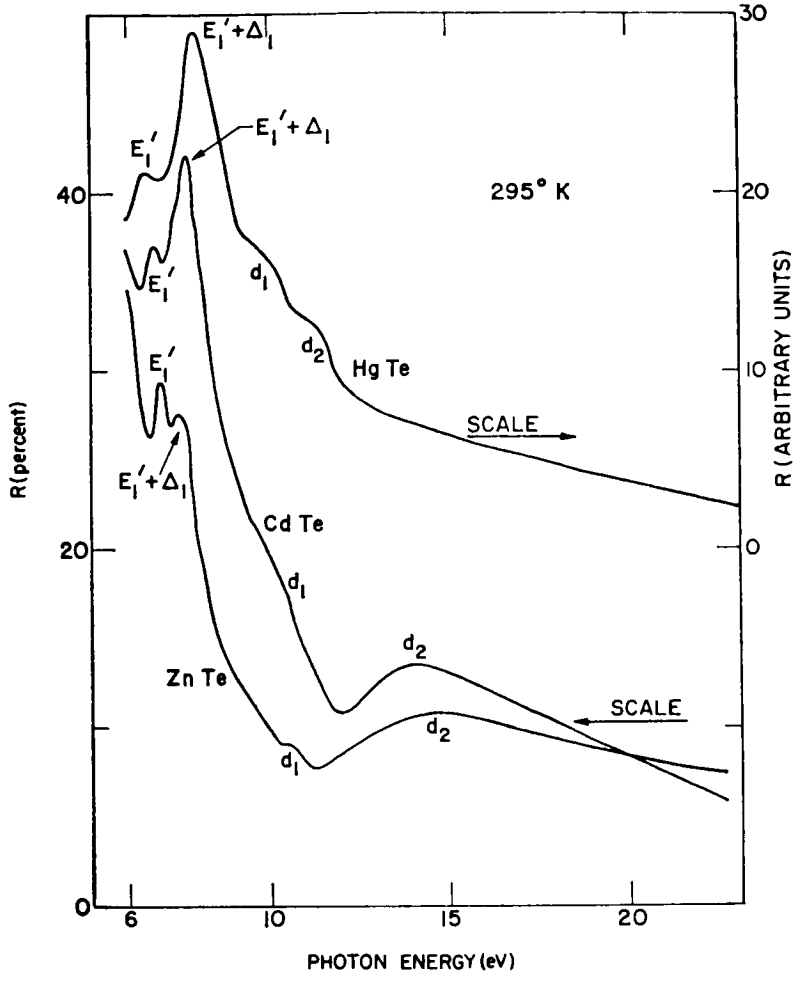

FIG. 32. ZnTe, CdTe, AND HgTe REFLECTIVITIES MEASURED BY CARDONA AND GREENAWAY (1963) FOR $\hbar\omega > 6$ eV.

The reflectivity peaks at 6.8 and 7.6 eV (Fig. 32) were assigned by CG to $L_3^v - L_3^c$ transitions (these reflectivity peaks were labeled E_1' by CG). The splitting of the peaks (0.8 eV) is supposedly due to a spin-orbit splitting of L_3^v. The photoemission data are not compatible with this interpretation, since we do not observe a splitting due to a split valence band, even though the splitting of the reflectivity peaks is much larger than our resolution (Chapter III, Sec. B4). Spin-orbit splitting of the same magnitude has been observed in other photoemission studies (SPICER, 1963; SPICER and LAPEYRE, 1965). Rather, we feel that the interpretation of the E_1' doublet needs revision. We have suggested

above that the 6.8 reflectivity peak is due to transitions near X, and that the 7.6 eV reflectivity peak is due to transitions near L.

There are other strong arguments that suggest that the 6.8 and 7.6 eV reflectivity peaks (E_1' and $E_1' + \Delta_1$ in Fig. 32) are not due to spin-orbit splitting. Whereas the spin-orbit splittings of L_3^v as deduced from $\Lambda_3 - \Lambda_1$ transitions (CARDONA and GREENAWAY, 1963) are nearly the same for ZnTe (0.56), CdTe (0.56), and HgTe (0.62), the splittings of the E_1' peaks (Fig. 32) are vastly different in the three materials (0.59, 0.88, and 1.25 eV). If the E_1' peaks were due to spin-orbit splitting, then we would expect the splittings to be the same in ZnTe, CdTe, and HgTe, since the spin-orbit splitting is primarily due to the Te ion. If the E_1' peaks had initial states near L_3^v, then in a given material the splitting of the E_1' peaks should be nearly the same as the splitting deduced from the $\Lambda_3 - \Lambda_1$ transitions. Also, the shapes of the E_1' peaks vary considerably among the three compounds, whereas if the doublet nature were due to spin-orbit splitting, the shapes would be similar in the three materials as they are for the Λ transitions.

In Table 2 we summarize our interpretation of the photoemission and optical data for CdTe. We compare the results of the present work and the pseudopotential calculation by COHEN and BERGSTRESSER (CG). The estimated uncertainty in the experimental values is ±0.2 eV. We have adjusted the calculated values (CB) to include the effects of spin-orbit splitting of Γ_{15}^v (0.9 eV) and L_3^v (0.6 eV). All levels are given relative to the uppermost of the spin-orbit-split levels Γ_{15}^v.

Our value for L_3^v disagrees with the pseudopotential band structure. We have located L_3^v at -1.8 eV, whereas CB find the spin-orbit-split levels L_3^v at -0.4 and -1.0 eV. The photoemission data say emphatically that the electronic transitions causing the peak P2 (Figs. 19 and 20) for $\hbar\omega = 8.0$ eV (corresponding to the reflectivity peak at 7.6 eV) have initial states near -1.8 eV and final states near 6.2 eV. There are only two alternatives: (1) L_3^v is much deeper than the pseudopotential calculation suggests, or (2) this transition for $\hbar\omega = 8.0$ eV does not occur in the immediate vicinity of L.

TABLE 2. COMPARISON OF PHOTOEMISSION RESULTS AND PSEUDOPOTENTIAL CALCULATION (CB) FOR CdTe (All energies in electron volts above Γ_{15}^{v}.)

Level	Present Work	CB
Γ_1 (or Γ_{12})	8.7	---
L_1^c	8.5	---
L_3^c	6.2	6.3
Γ_{15}^c	5.8	6.3
X_3	5.4	4.2
X_5	-1.4	-1.4
L_3^v	-1.8	-0.4, -1.0
X_1^v	-3.0	-3.2
L_1^v	-3.5	-3.2

D. DENSITY OF STATES ANALYSIS OF CdTe PHOTOEMISSION DATA

We have shown that the sharp features of the photoemission data are due to direct transitions. The density of states analysis (Chapter II, Sec. D) must therefore find that the nondirect constant-matrix-elements (NDCME) model is not sufficient to explain the photoemission data. A unique density of states cannot be determined, but general features of the density of states are usually apparent. Comparison of the valence band and effective conduction band densities of states seen by various conduction band and valence band states allows an estimate of the matrix element variation required to explain the photoemission data.

In this analysis we have not used any of the optical data for CdTe. It was shown in Chapter II, Sec. D1, that we are in effect assuming that $\epsilon_2\omega^2$ is approximately independent of ω if $\alpha L \gg 1$, and that $n\omega$ is approximately independent of ω if $\alpha L \ll 1$. As shown in Chapter VII, Sec. B, the very low yield of about 3 percent for the high-vacuum sample indicates that the escape depth is much shorter than the absorption depth

($\alpha L \ll 1$). We are therefore assuming that $n\omega$ is approximately independent of ω. The large yield observed in the low-vacuum experiment is due to the escape of secondary electrons (Chapter VII). Using published optical data (CARDONA, 1965), we estimate that for $6 < \hbar\omega < 12$, $n\omega$ varies by at most 40 percent over the entire region, and by at most 20 percent over any 1 eV range in photon energy. The analysis below shows that the matrix-element variation required to explain the photoemission data is much larger than this error due to the neglect of optical data.

Uncertainty in the yield measurement will also introduce error into the density of states analysis. Since the maximum uncertainty in the yield is 15 percent over a region of 1 eV in photon energy (Chapter III, Sec. B), the maximum distortion of the density of states analysis due to an error in yield is about 15 percent over a region of 1 eV.

1. High-Vacuum Data

In Figs. 33 and 34 we present the valence band and effective conduction band densities of states derived from the high-vacuum data. The values of the density of states used to derive these results are shown in Table 3. E_f indicates the energy of the final state used in deriving the valence band density of states. Similarly, E_i indicates the energy of the initial state used in deriving the effective conduction band density of states. Recall that if the valence band densities of states seen by various final energies superimpose and if the effective conduction band densities of states seen by various initial energies superimpose, then one must conclude that the NDCME model is sufficient to explain the photoemission from CdTe. In some regions of Figs. 33 and 34, two curves differ by as much as a factor of 3.

Although the NDCME model fails in detail, the density of states analysis allows us to make qualitative statements about the density of states. The valence band density of states peaks at about -1.6 eV. The rise in the valence band density of states in Fig. 33 for $E < -3.8$ eV is probably due to the escape of scattered electrons. From Fig. 33 we therefore estimate that the valence band is about 3.8 eV wide. The effective conduction band density of states drops steadily for $E > 6.5$ eV. Since $\alpha L \ll 1$, the energy distribution of the photoemitted electrons is proportional to the energy distribution of the photoexcited electrons, to

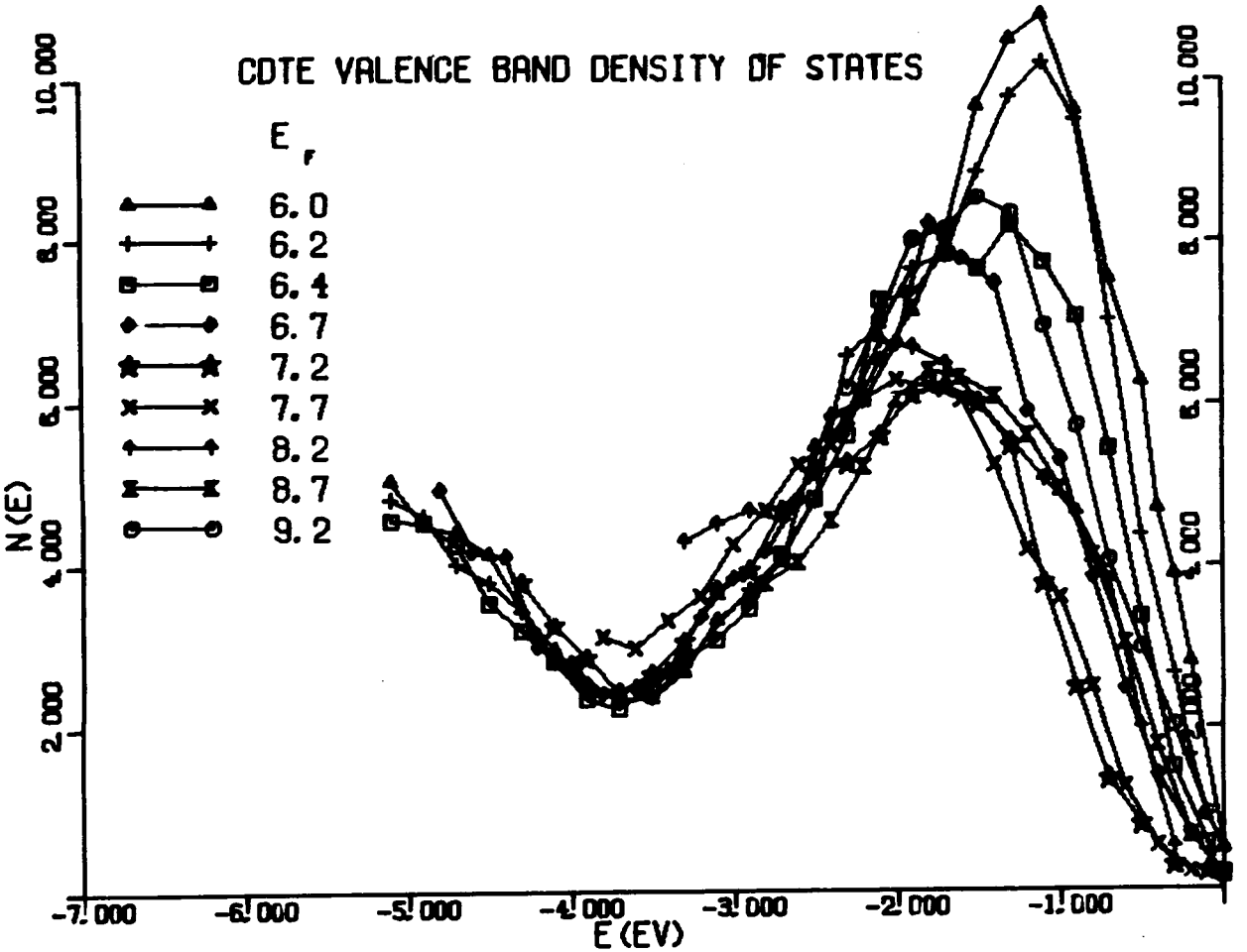

FIG. 33. CdTe VALENCE BAND DENSITY OF STATES DETERMINED BY DENSITY OF STATES ANALYSIS OF HIGH-VACUUM PHOTOEMISSION DATA. E_f is the energy of the conduction band state used to derive the valence band density of states.

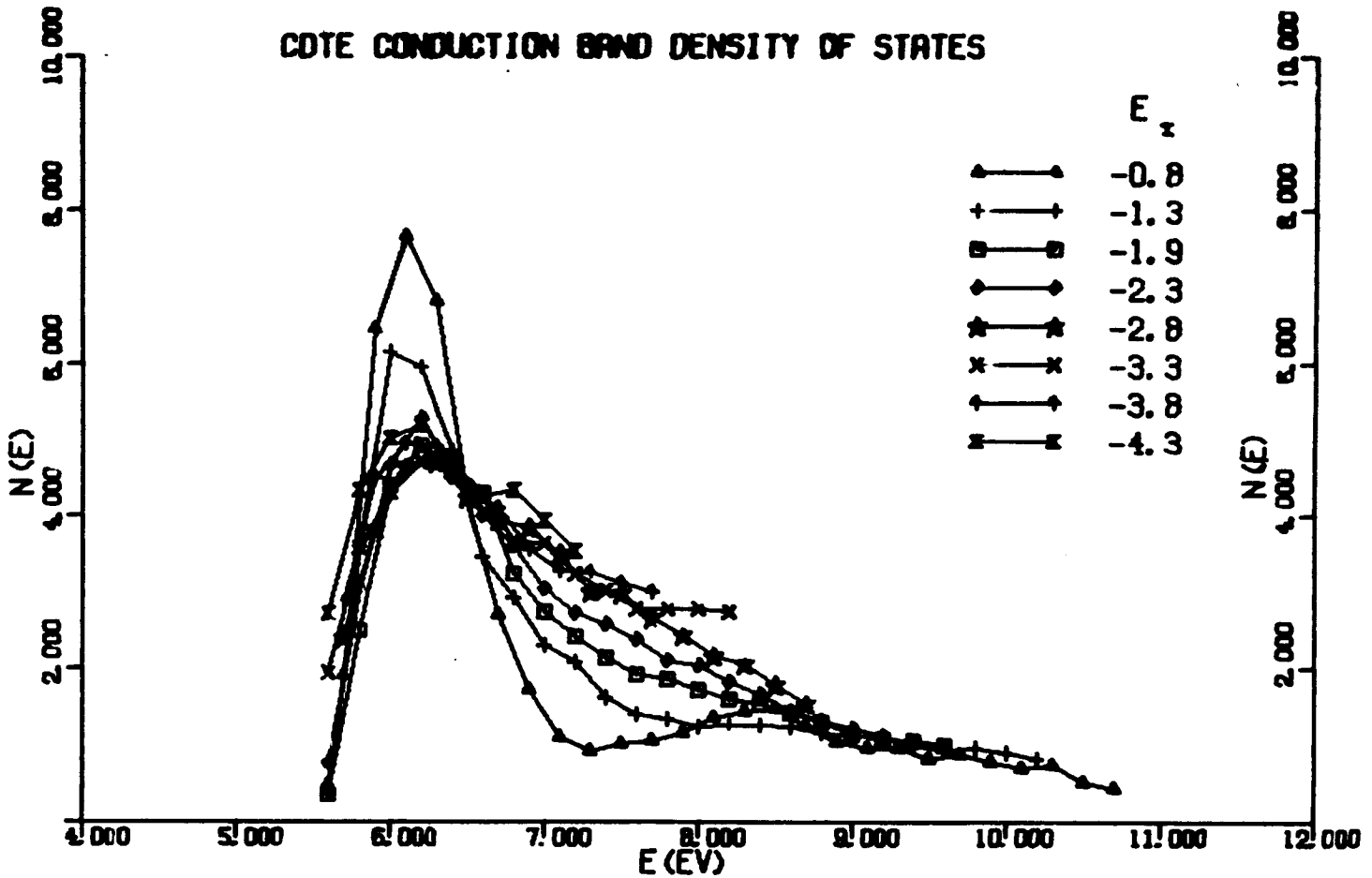

FIG. 34. CdTe EFFECTIVE CONDUCTION BAND DENSITY OF STATES DETERMINED BY DENSITY OF STATES ANALYSIS OF HIGH-VACUUM PHOTOEMISSION DATA. E_i is the energy of the initial state used to derive the effective conduction band density of states.

TABLE 3. SCALE FACTORS FOR DENSITY OF STATES ANALYSIS OF HIGH-VACUUM PHOTOEMISSION DATA FOR CdTe

E_i	$N_v(E_i)$	E_f	$N_c^{eff}(E_f)$
-0.8	5.3	6.0	4.68
-1.3	7.8	6.2	4.86
-1.9	7.4	6.4	4.73
-2.4	5.7	6.7	3.78
-2.8	3.9	7.2	3.02
-3.3	2.8	7.7	2.27
-3.8	2.3	8.2	1.83
-4.3	3.15	8.7	1.63
		9.2	1.35

L(E), the escape depth for an electron at energy E, and to T(E), the surface transmission probability (Chapter II, Sec. D1). The steady drop in the effective conduction band densities of states (Fig. 34) is probably due to a decrease in escape depth with increasing electron energy.

Figures 33 and 34 contain a wealth of information about the direct transitions observed in the photoemission data. It can be seen in Fig. 33 that initial states near the top of the valence band are more strongly coupled to conduction band states near 6.2 eV than are deeper valence band states. In other words, for transitions to final states near 6.2 eV, the enhancement due to matrix elements is strongest for initial states near the top of the valence band.

This feature of the density of states analysis of high-vacuum data is due to the same transitions as cause peak P2 in the photoemission data (Figs. 19 and 20). We showed earlier (Sec. B1) that P2 is due to direct transitions, and in Sec. C we used these data to locate L_3^c at 6.2 eV and L_3^v at -1.8 eV. However, the density of states analysis suggests that the "spirit" in which we locate L_3^v (see Sec. C) is in error, and the strongest enhancement of transitions to final states near

6.2 eV actually occurs for initial states closer to the top of the valence band. Hence, L_3^v may actually be much closer to the top of the valence band than we suggested in Sec. D. Then the 7.6 eV reflectivity peak ($E_1' + \Delta_1$ in Fig. 32) also is not due to states close to L.

The direct transitions causing the shoulder S2 in the energy distributions (Figs. 26 to 28) are also apparent in Fig. 33. It can be seen there that initial states above -1.5 eV are more strongly coupled to final states near 8.2 and 8.7 eV than to final states near 7.2 and 7.7 eV.

2. Low-Vacuum Data

In Figs. 35 and 36 we present the valence band and effective conduction band densities of states derived from the low-vacuum data. Table 4 contains the values of the scale factors used in this analysis. As shown in Sec. B1, the effects of the poorer vacuum are a lowering of the electron affinity by more than one volt, and the appearance of a large number of secondary electrons in the energy distributions. The latter effect has a large influence on the derived valence band density of states below about -2.8 eV. Comparing the valence band density of states for the high-vacuum cleavage (Fig. 33) with that for the low-vacuum cleavage (Fig. 35), we find that for energies less than about -2.8 eV there is a large apparent valence band density of states for the low-vacuum cleavage that is not seen in the high-vacuum data. These effects are believed to be due to the appearance of secondary electrons in the energy distributions. Although this difference in scattering is not understood in detail, the relevant experimental data are discussed in Chapter VII.

The direct transitions observed in the energy distributions have a pronounced effect on the density of states analysis. We see in Fig. 35 that initial states within ~ 0.5 eV of the top of the valence band are most strongly coupled to final states near 5.9 eV. The corresponding feature of the energy distributions is the shoulder S1 (Fig. 18) which we assigned in Sec. C to direct transitions to final states near Γ_{15}^c at 5.8 eV.

Also in Fig. 35, initial states near -1.5 eV are most strongly coupled to final states between 5.1 and 5.5 eV. The corresponding feature of the energy distributions is peak P1 at 5.4 eV for $\hbar\omega = 6.8$ eV (Figs.

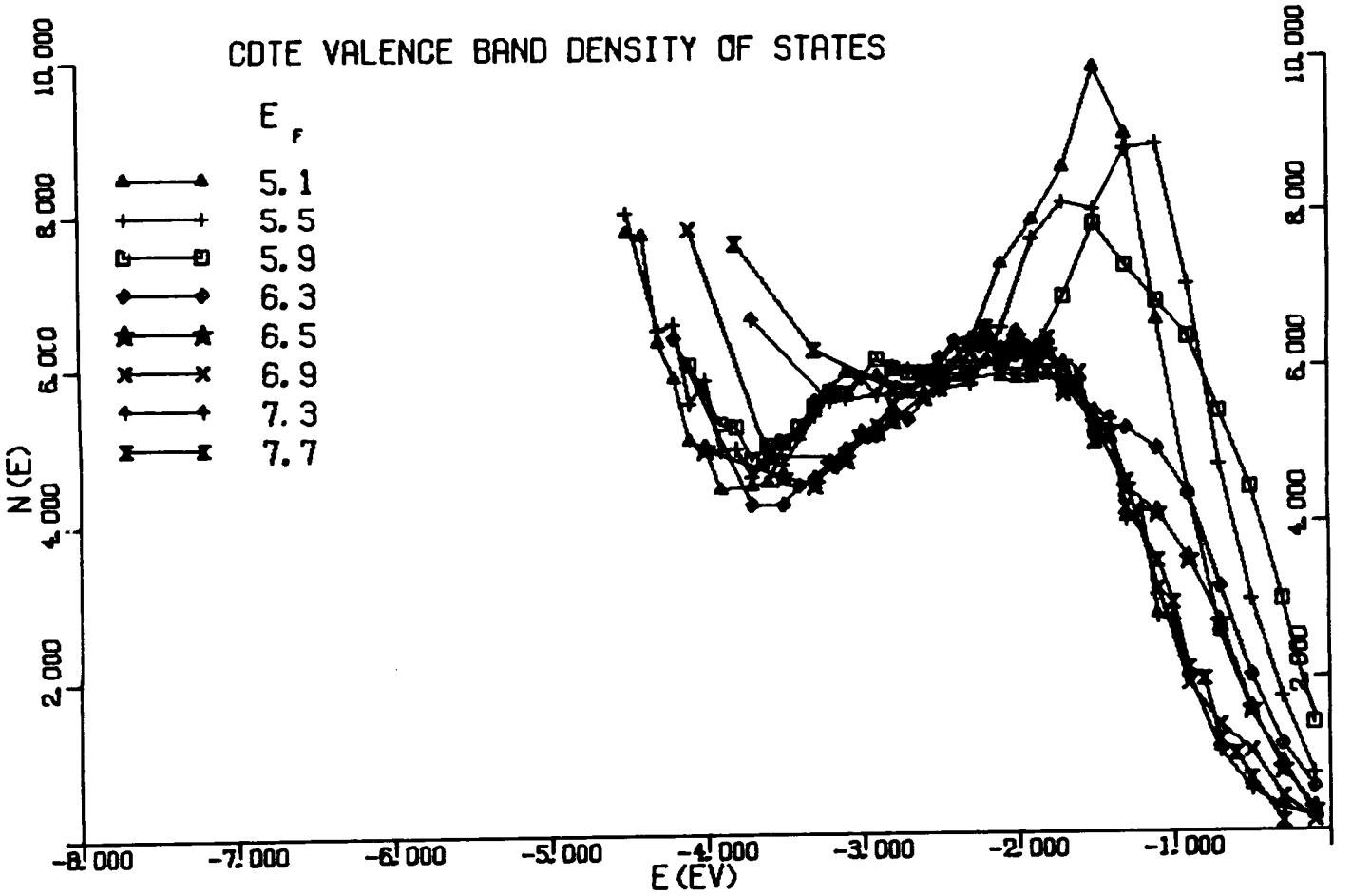

FIG. 35. CdTe VALENCE BAND DENSITY OF STATES DETERMINED BY DENSITY OF STATES ANALYSIS OF LOW-VACUUM PHOTOEMISSION DATA. E_f is the energy of the conduction band state used to derive the valence band density of states.

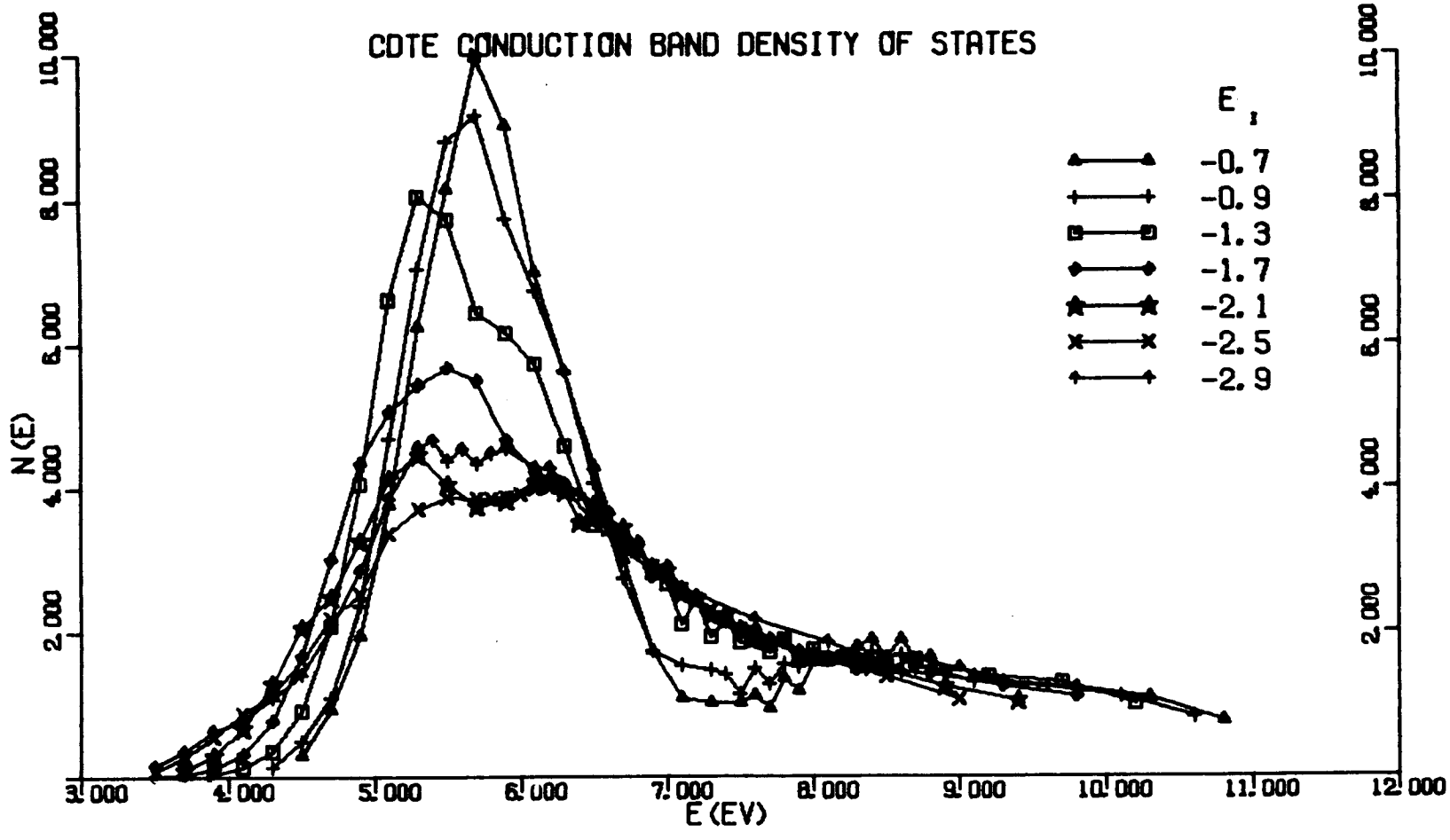

FIG. 36. CdTe EFFECTIVE CONDUCTION BAND DENSITY OF STATES DETERMINED BY DENSITY OF STATES ANALYSIS OF LOW-VACUUM PHOTOEMISSION DATA. E_i is the energy of the initial state used to derive the effective conduction band density of states.

TABLE 4. SCALE FACTORS FOR DENSITY OF STATES ANALYSIS OF LOW-VACUUM PHOTOEMISSION DATA FOR CdTe

E_i	$N_v(E_i)$	E_f	$N_c^{eff}(E_f)$
-0.7	2.32	5.1	3.44
-0.9	3.20	5.5	4.06
-1.3	4.64	5.9	3.90
-1.7	5.80	6.3	4.10
-2.1	6.14	6.5	3.70
-2.5	5.97	6.9	2.90
-2.9	5.22	7.3	2.24
		7.7	1.92

18 and 19) which we assigned in Sec. C to direct transitions to final states near X_3 (5.4 eV) from initial states near X_5 (-1.4 eV).

For $E > -1.5$ eV in Fig. 35, transitions to final states near 6.2 eV are enhanced above the prediction of the NDCME model. The corresponding feature of the photoemission data is peak P2 (Figs. 19 and 20). In Sec. C we assigned P2 to direct transitions to L_3^c at 6.2 eV from initial states near L_3^v at -1.8 eV. However, it is apparent in Fig. 35 (as it was in the high-vacuum density of states analysis) that the enchancement of transitions to final states near 6.2 eV is greatest for initial states closer to the top of the valence band. Hence L_3^v may be much closer to the top of the valence band than we suggested in Sec. C.

Although the effects of scattering obscure most of the valence band structure in Fig. 35 for valence band energies below about -2.8 eV, there is a bulge between -3.6 and -2.6 eV in the valence band density of states seen by final states in the region $5.1 < E_f < 5.9$ eV. This bulge indicates that transitions from valence band states between -3.6 and -2.6 eV to conduction band states between 5.1 and 5.9 eV are enchanced above the predictions of the NDCME model. These transitions are probably due to initial states near X_1 in the valence band and final states near X_3 in the conduction band.

E. OTHER RESULTS

1. Gunn Oscillations

The location of L_3^v required to explain the photoemission data suggests a possible explanation for the recent observation (FOYT, 1966) of Gunn oscillations (GUNN, 1963) in CdTe. The analysis in Sec. C locates L_3^v at about -1.8 eV. This is probably the center of gravity* of the spin-orbit-split levels. If we use the splitting of 0.56 eV deduced from $\Lambda_3 - \Lambda_1$ reflectivity peaks, the two L_3^v levels lie at -2.08 and -1.52 eV. The $\Lambda_3 - \Lambda_1$ reflectivity peaks at 3.32 and 3.88 eV probably place upper bounds on the $L_3^v - L_1$ separation. This locates L_1 at 1.8 eV, only 0.2 eV above the minimum at Γ.

It is not likely that Gunn oscillations would occur in n-type CdTe if the band structure of Fig. 30 were correct, since the satellite conduction band minima at X_1 and L_1 are at least 1.5 eV above the minimum at Γ_1. It is presently believed (HILSUM, 1962; HUTSON et al, 1965) that Gunn oscillations require the existence of a satellite minimum a fraction of a volt above the absolute conduction band minimum. Our results indicate that the satellite minimum at L_1 is actually much lower than shown in Fig. 30. It is therefore likely that the Gunn oscillations observed in n-type CdTe involve hot carriers in (111) minima.

2. Agreement with Other Calculations

We have located Γ_{15}^c at 5.8 eV in the conduction band (Sec. C), whereas COHEN and BERGSTRESSER have calculated this level at 6.3 eV (Table 2). We present here a possible explanation for this disagreement. In spite of the difficulties involved in extracting the energies of critical points from photoemission or optical data (Sec. C), we are especially confident of our location of Γ_{15}^c. The Γ_{15}^v valence band state is an absolute maximum; hence the $\Gamma_{15}^v - \Gamma_{15}^c$ separation can be accurately measured by determining the photon energy for which these transitions first occur.

---

*Note, however, that we do not observe this splitting in the photoemission data, although this splitting is much larger than the experimental resolution.

The pseudopotential band structure of CdTe is calculated by adding an antisymmetric potential to the symmetric potential appropriate to tin. In other words, the Hamiltonian which is diagonalized contains the same symmetric pseudopotential that is used for tin, and in addition an antisymmetric potential. Any error in either symmetric or antisymmetric potential will lead to errors in the calculated band structure. There is some evidence that the symmetric potential is slightly in error.

HERMAN et al (1966) have calculated the band structures of Sn, Ge, and Si using the OPW method. These authors find that their largest discrepancies with the pseudopotential calculations (COHEN and BERGSTRESSER, 1966) occur at Γ_{15}^{c}. The pseudopotential values for Γ_{15}^{c} are consistently at least 0.5 eV above the OPW values. It appears that the pseudopotential used for Sn is incorrect in that it causes Γ_{15}^{c} to be too high. It therefore seems likely that when the same symmetric potential is used for the calculation of CdTe's band structure, the Γ_{15}^{c} level for CdTe will also be too high.

F. CONCLUSIONS

Most of the sharp features of the CdTe energy distributions require direct transitions for an explanation. However, for photon energies above 10.9 eV it was clearly shown that both direct and NDCME transitions occur in the same high-vacuum-cleaved sample for the same photon energies.

By comparing the results of our photoemission studies with the calculated band structure for CdTe (COHEN and BERGSTRESSER, 1966) and with reflectivity data (CARDONA and GREENAWAY, 1963), we have determined the energies of the conduction band states X_3, Γ_{15}^{c}, L_3^{c}, L_1^{c}, and Γ_1 (or Γ_{12}), and of the valence band states L_3^{v}, X_5, X_1, and L_1^{v}. These results were summarized in Table 2. Also, a valence band, believed to be due to cadmium 4d levels, has been located at -10.3 eV.

In most cases, our results agree with the pseudopotential calculation within $\sim$ 0.5 eV; however, we find L_3^{v} much deeper than do CB. We located L_3^{v} using the features of peak P2 in the energy distributions (Figs. 19 and 20). The density of states analysis (Sec. D) indicates that direct transitions to final states near 6.2 eV (L_3^{c}) are strongest for initial states much closer to the top of the valence band. Hence L_3^{v} may be

much closer to the top of the valence band than we indicated in Sec. C.

We suggest new interpretations for several reflectivity peaks (Figs. 31 and 32). We find that the 5.2 eV peak (E_o') is not due to $\Gamma_{15}^v - \Gamma_{15}^c$ transitions as earlier thought (CG). It is more likely that structure which CG observed in the reflectivity near 5.7 or 6.0 eV is due to $\Gamma_{15}^v - \Gamma_{15}^c$ transitions. We also find that the doublet nature of the E_1' peaks is not due to spin-orbit splitting. Instead we suggest that the 6.8 eV peak is due to transitions near X and the 7.6 eV peak is due to transitions near L. Finally, the photoemission data is compatible with the assignment of the d_1 reflectivity peak to transitions near L.

V. PHOTOEMISSION FROM CdSe

In this chapter the data obtained from photoemission studies of CdSe are presented and interpreted. The photoemission experiments have been performed on single crystals cleaved in high vacuum (pressure = 10^{-9} torr) and in low vacuum (pressure = 10^{-4} torr). For experimental details see Chapter III. A larger region of the conduction band is exposed in the low-vacuum experiments, since the electron affinity is more than a volt lower than in the high-vacuum experiments.

In Secs. A and B of this chapter, the CdSe quantum yield and energy distributions are presented and discussed. In Sec. C the density of states analysis (Chapter II, Sec. D) is applied to the CdSe photoemission data. We explicitly show that the NDCME model is sufficient to explain most of the high-vacuum data. The NDCME model is not sufficient to explain the transitions to conduction band states exposed only in the low-vacuum experiments. We determine the matrix-element variation required to explain this low-vacuum photoemission data. In Sec. D we discuss the band structure and optical properties of CdSe in light of the photoemission data.

A. QUANTUM YIELD

We present in Fig. 37 the spectral distribution of the quantum yield for a CdSe crystal cleaved in high vacuum, and for the same crystal cleaved in low vacuum. In the low-vacuum experiment the sample was exposed to a pressure of 10^{-4} torr, which resulted in an electron affinity more than a volt lower than for the sample cleaved at a pressure of 10^{-9} torr. There also resulted a rise in yield for photon energies greater than 9.6 eV, with a maximum low-vacuum yield about four times as large as the maximum high-vacuum yield. We believe that the rise in yield is due to the escape of secondary electrons; however, we defer to Chapter VII a discussion of the evidence for this interpretation.

The two curves of Fig. 37 were measured using the Cs_3Sb standard for measuring light intensity (Sec. B1, Chapter III). This same standard was used for both high- and low-vacuum CdS experiments (Chapter VI), and for

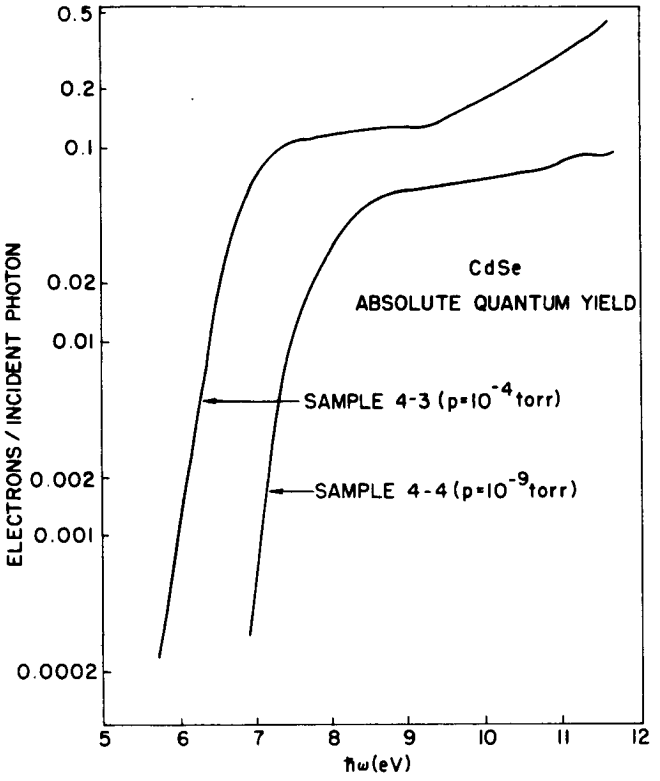

FIG. 37. ABSOLUTE QUANTUM YIELD OF CdSe FOR A PHOTON ENERGY $\hbar\omega$.

the CdTe low-vacuum experiment (Chapter IV). As discussed in Chapter III, the relative response of the standard as a function of photon energy was determined assuming that the efficiency of sodium salicylate is independent of photon energy. The detailed shapes of the curves of Fig. 37 will therefore depend upon the uniformity of the response of sodium salicylate. Although the yield is uncertain by at most 15 percent over any 1 eV range in $\hbar\omega$, for a given photon energy the ratio of the high-vacuum yield to the low-vacuum yield should be correct to within a few percent, since both measurements used the same standards.

B. ENERGY DISTRIBUTIONS OF PHOTOEMITTED ELECTRONS

1. Low-Vacuum Experiments

In Figs. 38 through 43 we present the energy distributions of the photoemitted electrons for the sample cleaved at a pressure of 10^{-4}

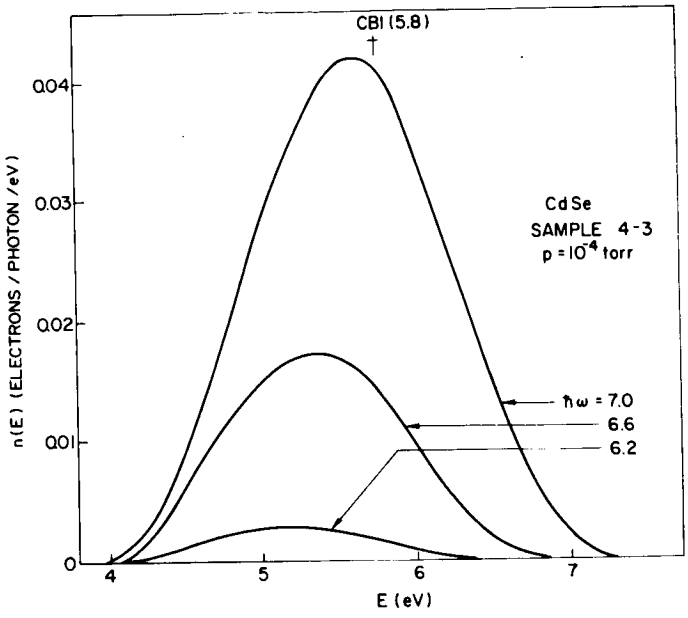

FIG. 38. NORMALIZED ENERGY DISTRIBUTIONS OF PHOTOEMITTED ELECTRONS FROM CdSe FOR $6.2 \leq \hbar\omega \leq 7.0$ eV. Electron energy E is measured relative to the valence band maximum.

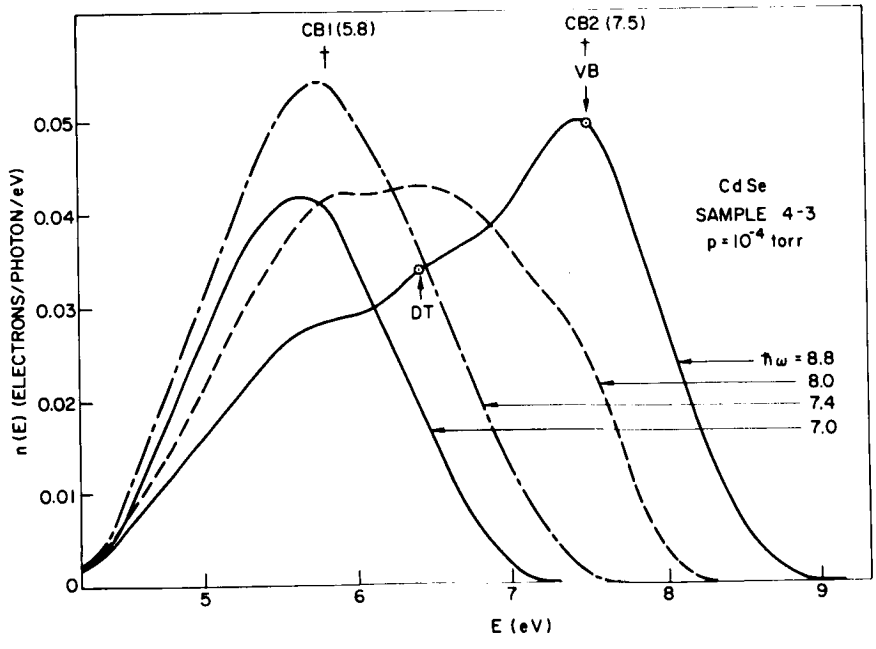

FIG. 39. NORMALIZED ENERGY DISTRIBUTIONS OF PHOTOEMITTED ELECTRONS FROM CdSe FOR $7.0 \leq \hbar\omega \leq 8.8$ eV. Electron energy E is measured relative to the valence band maximum.

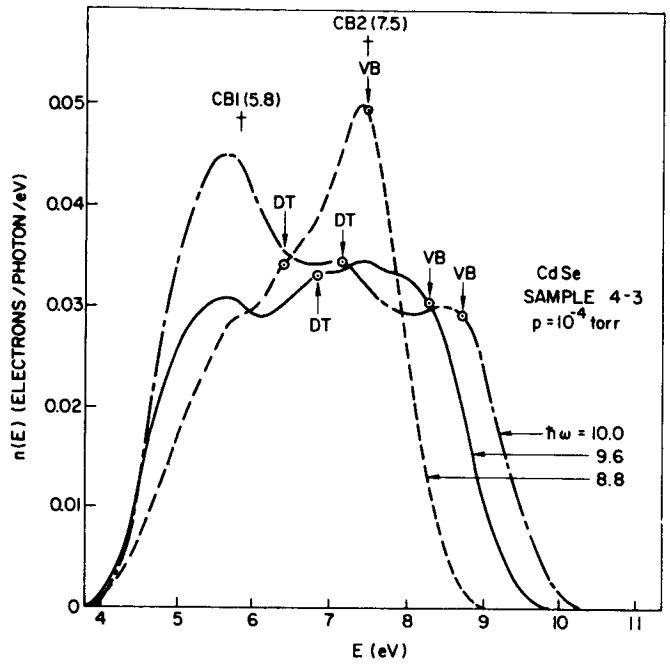

FIG. 40. NORMALIZED ENERGY DISTRIBUTIONS OF PHOTOEMITTED ELECTRONS FROM CdSe FOR $8.8 \leq \hbar\omega \leq 10.0$ eV. Electron energy E is measured relative to the valence band maximum.

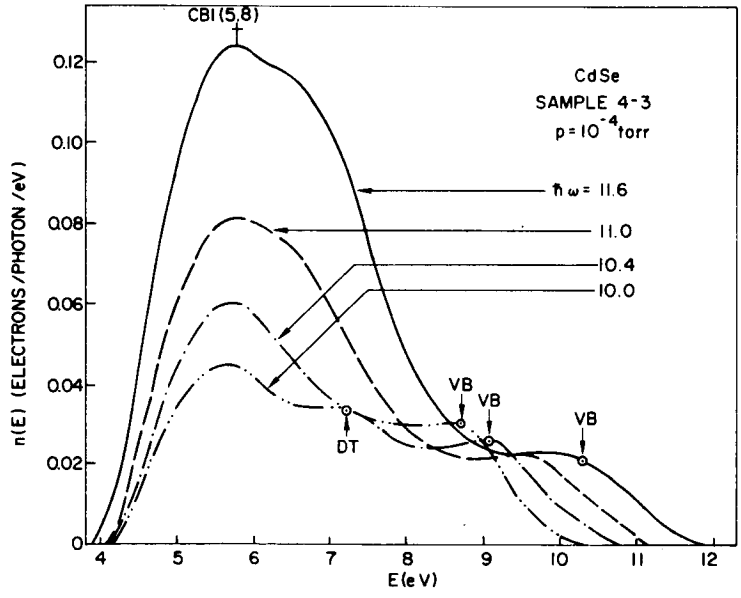

FIG. 41. NORMALIZED ENERGY DISTRIBUTIONS OF PHOTOEMITTED ELECTRONS FROM CdSe FOR $\hbar\omega \geq 10.0$ eV. Electron energy E is measured relative to the valence band maximum.

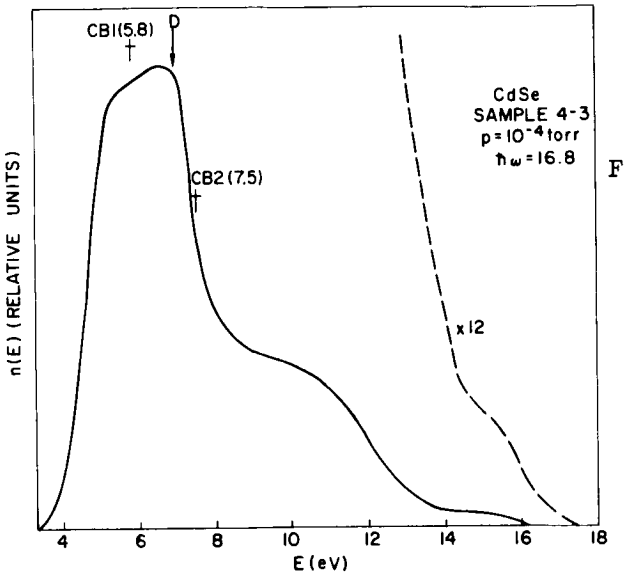

FIG. 42. ENERGY DISTRIBUTION OF PHOTOEMITTED ELECTRONS FROM CdSe FOR $\hbar\omega$ = 16.8 eV. Electron energy E is measured relative to the valence band maximum. The "× 12" curve is slightly distorted due to the large amount of filtering necessary for this curve.

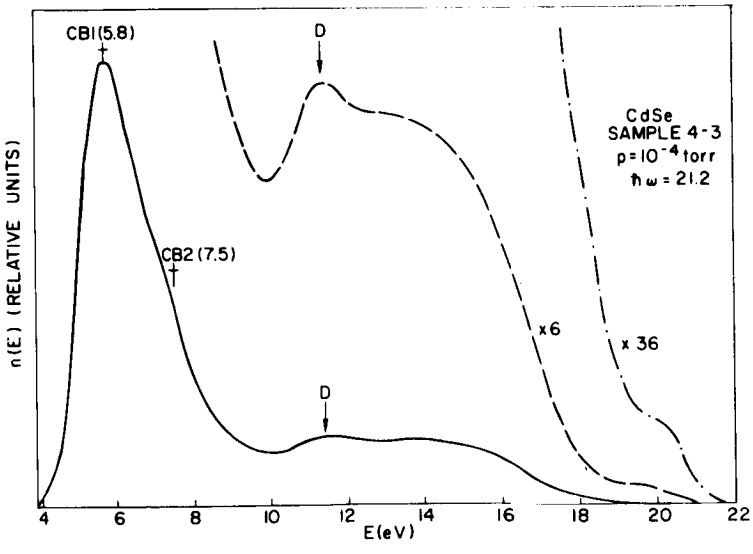

FIG. 43. ENERGY DISTRIBUTION OF THE PHOTOEMITTED ELECTRONS FROM CdSe FOR $\hbar\omega$ = 21.2 eV. Electron energy E is measured relative to the valence band maximum. The "× 36" curve is slightly distorted due to the large amount of filtering necessary for this curve.

torr. Except for $\hbar\omega$ = 16.8 and 21.2 eV, all energy distributions are normalized to the quantum yield. Electron energies are stated relative to the valence band maximum; the calibration of the energy scale was discussed in Chapter III, Sec. B3. We show in Chapter VII that the large number of low-energy electrons appearing in the energy distributions for $\hbar\omega > 9.6$ eV are secondary electrons.

Both direct and NDCME transitions are observed in the low-vacuum photoemission data (the characteristics of direct and NDCME transitions are discussed in Chapter II, Secs. C1 and C2). Other matrix-element-dependent transitions are also observed, but these are not necessarily direct transitions.

For $\hbar\omega \geq 8.8$ eV, a peak of electrons labeled VB appears in the energy distributions (Figs. 39 to 41). For a photon energy $\hbar\omega$, this peak is indicated by an arrow at an energy

$$E = \hbar\omega - 1.3 \text{ eV} \qquad (30)$$

The motion of the peak of electrons VB in accordance with Eq. (30) is characteristic of NDCME transitions from a peak at -1.3 eV in the valence band density of states (Chapter II, Sec. C2). This motion indicates that conservation of $\bar{K}$ is not an important selection rule for the transitions associated with peak VB.

For $\hbar\omega$ = 8.8 eV, valence band states near -1.3 eV are strongly coupled to conduction band states at 7.5 eV; this leads to the pronounced peak CB2 at 7.5 eV (Figs. 39 and 40). For $\hbar\omega > 8.8$ eV, the peak of electrons VB moves to higher energies, but a peak of electrons CB2 remains at 7.5 eV. For $\hbar\omega > 10$ eV, CB2 disappears from the energy distributions. This disappearance of a peak of electrons is characteristic of direct transitions (Chapter II, Sec. C2). If the peak CB2 were only due to NDCME transitions, we would expect the strength of the peak observed at 7.5 eV to be modulated by the valence band density of states, but this peak should not disappear entirely.

Other direct transitions are also observed in the low-vacuum data. For $7.4 < \hbar\omega < 10.6$ eV (Figs. 39 to 41) there is a small peak of electrons DT indicated by an arrow at an energy

$$E = 0.5\ \hbar\omega + 2.1\ \text{eV} \qquad (31)$$

The motion of the peak DT in accordance with Eq. (31) is characteristic of direct transitions (Chapter II, Sec. C2). For $\hbar\omega = 10.6$ eV, DT is located at 7.5 eV, the same energy as the conduction band states CB2, and DT is not seen for photon energies greater than 10.6 eV. The disappearance of this peak may result from details of the band structure, or the peak may be masked by the large number of secondary electrons appearing in the energy distributions for photon energies greater than about 9.6 eV.

Other matrix-element-dependent transitions are also observed in the low-vacuum photoemission data, but these are not necessarily direct transitions. We now discuss the qualitative features of these transitions; the matrix-element variation will be much more clearly displayed by the density of states analysis in Sec. C. In Fig. 38 we see that the number of electrons excited to 5.8 eV (CB1) from initial states at -0.4 eV ($\hbar\omega = 6.2$ eV) is 1/8 of the number excited from -0.8 eV ($\hbar\omega = 6.6$ eV) and 1/25 of the number excited from -1.2 eV ($\hbar\omega = 7.0$ eV). It is apparent from the shape of the peak VB, that the valence band density of states does not show this sharp rise. Rather, the matrix elements that couple states near the top of the valence band to final states near 5.8 eV are much weaker than the matrix elements that couple deeper valence band states to these same final states.

In Figs. 42 and 43 we present the energy distributions of the photoemitted electrons for $\hbar\omega = 16.8$ eV and 21.2 eV. Many of the photoelectrons have been electron-electron scattered to conduction band states near CB1 and CB2. The peak of electrons labeled D at an energy of 11.3 eV is believed to be due to transitions from a high density of states at -9.9 eV. We suggest that these valence band states are derived from cadmium 4d states. The location of the d-band is discussed in more detail in Chapter VII, Sec. C.

It is not possible to follow the motion of peak D over a wide range of photon energy to confirm its origin in the valence band; however, if the peak were due to conduction band structure near 11.3 eV, we would expect to see a peak at 11.3 eV for $\hbar\omega = 16.8$ eV. No such peak is seen

in Fig. 42. If peak D is in fact due to transitions from valence band states at -9.9 eV, then this peak should be seen at 6.9 eV for $\hbar\omega$ = 16.8 eV. The structure labeled D at 6.9 eV in Fig. 42 is believed to be due to these transitions.

2. High-Vacuum Experiments

In Figs. 44 through 46 we present energy distributions for a sample of CdSe cleaved in a vacuum of 10^{-9} torr. There is a striking difference between these curves and the energy distributions for the same sample cleaved in the low-vacuum experiment (Sec. B1): The electron affinity is more than one volt larger for this high-vacuum cleavage than for the same sample cleaved in the low vacuum. In addition, the number of secondary electrons appearing in the energy distributions is much smaller than for the low-vacuum-cleaved sample. As shown in Chapter VII, this decrease in the number of photoemitted secondary electrons is not due solely to the larger electron affinity for the high-vacuum-cleaved sample, but is also due to a smaller number of secondary electrons produced internally in the high-vacuum-cleaved sample.

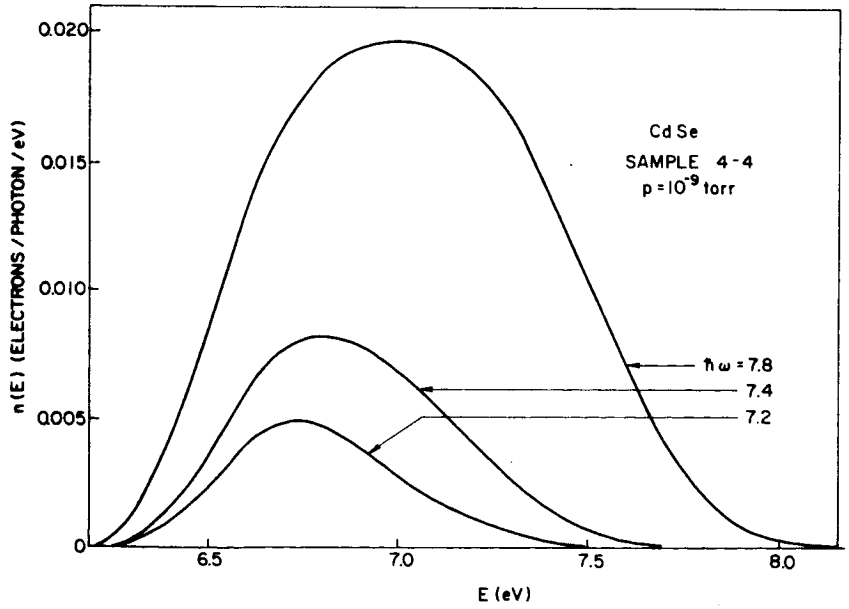

FIG. 44. NORMALIZED ENERGY DISTRIBUTIONS OF THE PHOTOEMITTED ELECTRONS FROM CdSe FOR $7.2 \leq \hbar\omega \leq 7.8$ eV. Electron energy E is measured relative to the valence band maximum.

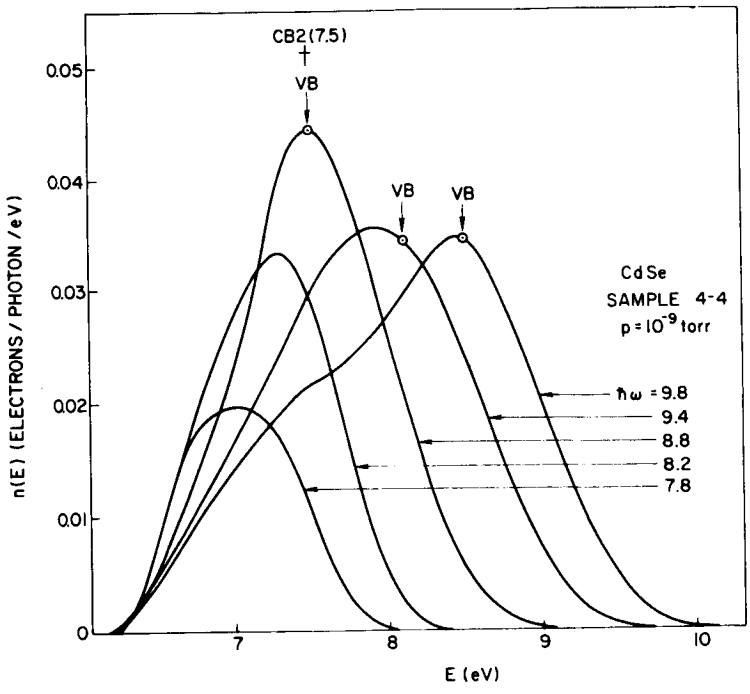

FIG. 45. NORMALIZED ENERGY DISTRIBUTIONS OF THE PHOTOEMITTED ELECTRONS FROM CdSe FOR $7.8 \leq \hbar\omega \leq 9.8$ eV. Electron energy E is measured relative to the valence band maximum.

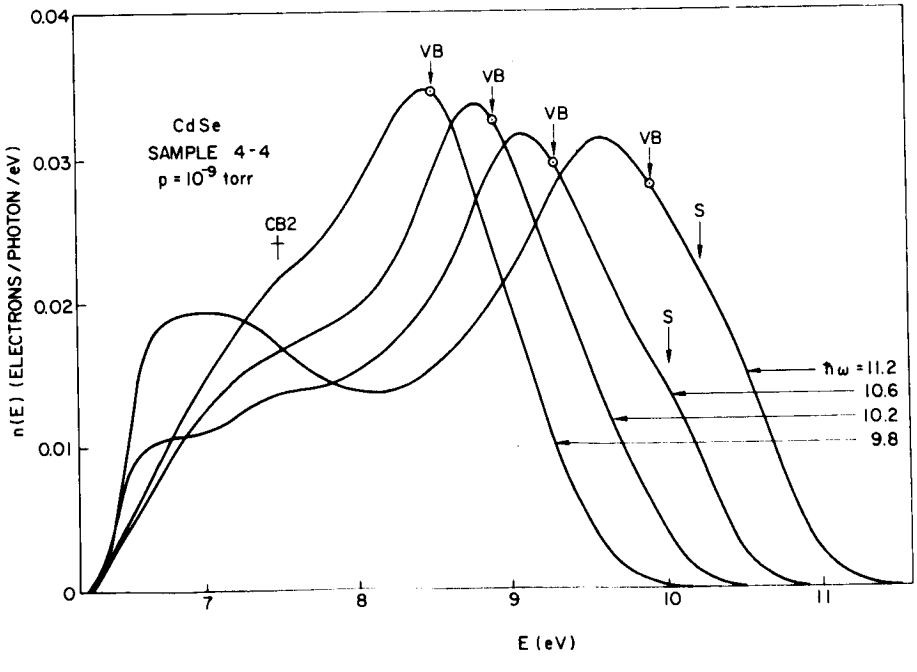

FIG. 46. NORMALIZED ENERGY DISTRIBUTIONS OF THE PHOTOEMITTED ELECTRONS FROM CdSe FOR $\hbar\omega \geq 9.8$ eV. Electron energy E is measured relative to the valence band maximum.

For the high-vacuum cleavage no structure is observed at CB1 (5.8 eV) since these states now lie below the vacuum level due to the increased electron affinity. Hence the matrix-element-dependent transitions to these final states are not observed in the high-vacuum experiments. Also, the peak of electrons DT moving in accordance with Eq. (31) for the low-vacuum experiment does not appear in the high-vacuum data due to the increase in electron affinity.

As in the low-vacuum data (Sec. B1), the peak of electrons labeled VB (Figs. 44 to 46) moves in accordance with Eq. (30). This peak is due to NDCME transitions from a peak at -1.3 eV in the valence band density of states. This motion indicates that conservation of $\bar{K}$ is not an important selection rule for the transitions associated with the peak VB. At high photon energies, the peak of electrons falls slightly behind the arrows which are determined by Eq. (30). This would result if a small portion of the peak VB were due to direct transitions. The peak VB would also fall behind Eq. (30) if the mean free path for electron-electron scattering were rapidly decreasing with increasing energy. However, this is not the case here, since the amplitude of the peak VB is not rapidly decreasing with increasing energy as it would if the mean free path for electron-electron scattering were rapidly decreasing.

As in the low-vacuum data (Sec. B1), for $\hbar\omega = 8.8$ eV the peak in the valence band density of states at -1.3 eV is strongly coupled to conduction band states near 7.5 eV (Fig. 45). We indicate with the dagger CB2 electrons photoemitted from the conduction band states near 7.5 eV.

A high-energy shoulder S appears in the energy distributions for $\hbar\omega > 10.2$ eV (Fig. 46). When it first appears, this shoulder is due to transitions from initial states near the top of the valence band to final states near 10.2 eV. The shoulder S appears to be due to direct transitions, but the data are insufficient to verify this with certainty. The features of S are very similar to the features of the shoulders S1 and S2 in the CdTe energy distributions (Chapter IV). These shoulders were shown to be due to direct transitions.

3. Effects of Hydrogen on High-Vacuum-Cleaved Surface

We have performed an experiment in which a high-vacuum-cleaved sample of CdSe was exposed to a 5-micron pressure of ultrapure Linde hydrogen in the high-vacuum chamber. The yield and energy distributions measured while the sample was exposed to the hydrogen were indistinguishable from the measurements before the high-vacuum cleavage was exposed to the hydrogen. This experiment shows conclusively that the lower electron affinity and increased number of secondary electrons which are observed in the low-vacuum measurements in the monochromator (for details, see Chapter III) are neither due to adsorbed hydrogen on the surface nor to hydrogen that has diffused into the crystal.

C. DENSITY OF STATES ANALYSIS OF CdSe PHOTOEMISSION DATA

The qualitative analysis in the previous section indicated that the photoemission from CdSe results from a mixture of NDCME and matrix-element-dependent transitions. In this section we shall use the density of states analysis to (1) explicitly demonstrate the simultaneous presence of both types of transitions, and (2) separate the effects of the NDCME transitions from the effects of the matrix-element-dependent transitions.

In this analysis we have not used any of the optical data for CdSe. It was shown in Chapter II that we are, in effect, assuming that $\epsilon_2\omega^2$ is approximately independent of ω if $\alpha L \gg 1$, and that $n\omega$ is approximately independent of ω if $\alpha L \ll 1$. As shown in Chapter VII, Sec. B, the low yield of about 6 percent for the high-vacuum-cleaved sample indicates that the escape depth is much shorter than the absorption depth ($\alpha L \ll 1$). We are therefore assuming that $n\omega$ is approximately independent of ω. The high yield observed in the low-vacuum experiment is due to the escape of secondary electrons (Chapter VII). The optical data presented in Fig. 47 shows that $n\omega$ varies by at most 17 percent in the entire region $6 < \hbar\omega < 10$ eV. The analysis given in Sec. C2 shows that the matrix-element variation required to explain the low-vacuum photoemission data is more than an order of magnitude larger than this error due to the neglect of optical data.

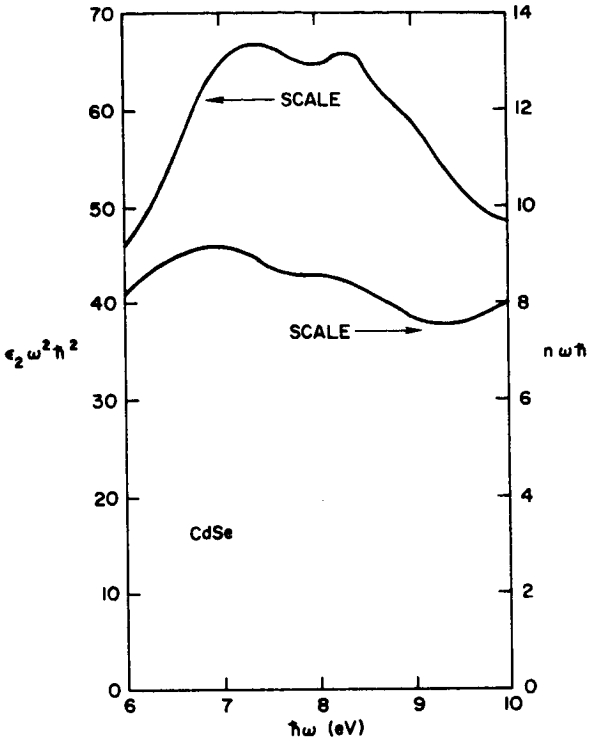

FIG. 47. OPTICAL DATA FOR CdSe DERIVED FROM DATA OF CARDONA AND HARBEKE (1965).

Uncertainty in the yield measurement will also introduce error into the density of states analysis. Since the maximum uncertainty in the yield is 15 percent over a region of 1 eV in photon energy (Chapter III, Sec. B), the maximum distortion of the density of states analysis due to the uncertainty in yield is about 15 percent over a region of 1 eV.

1. High-Vacuum Data

In Figs. 48 and 49 we present the valence band and effective conduction band densities of states derived using the data for the sample cleaved at a pressure of 10^{-9} torr. The density of states analysis is described in Chapter II, Sec. D. The scale factors used to derive the results of Figs. 48 and 49 are shown in Table 5. E_f indicates the energy of the final state used in deriving the valence band density of states. Similarly, E_i indicates the energy of the initial state used in deriving the effective conduction band density of states.

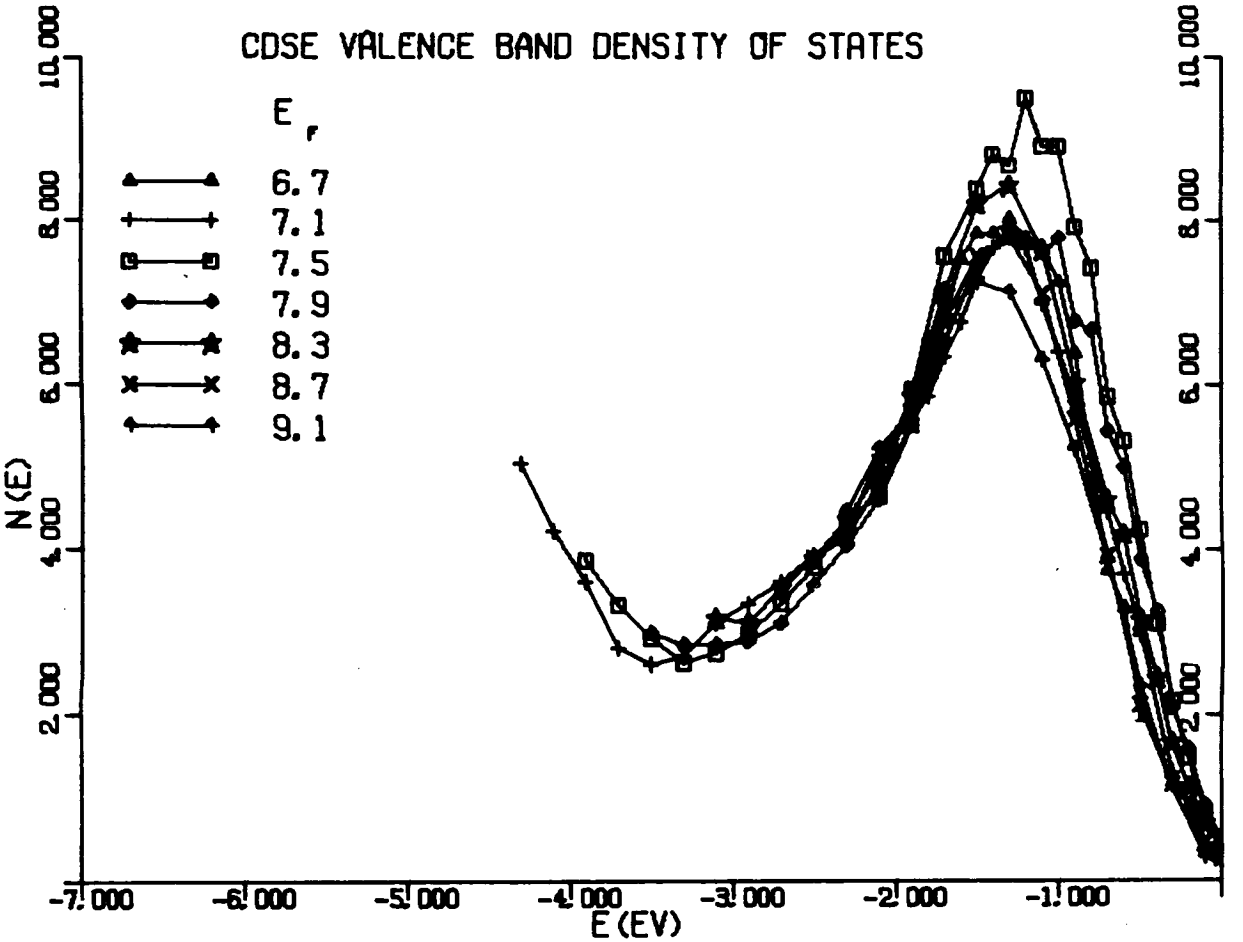

FIG. 48. CdSe VALENCE BAND DENSITY OF STATES DETERMINED BY DENSITY OF STATES ANALYSIS OF HIGH-VACUUM PHOTOEMISSION DATA. E_f is the energy of the conduction band state used to derive the valence band density of states.

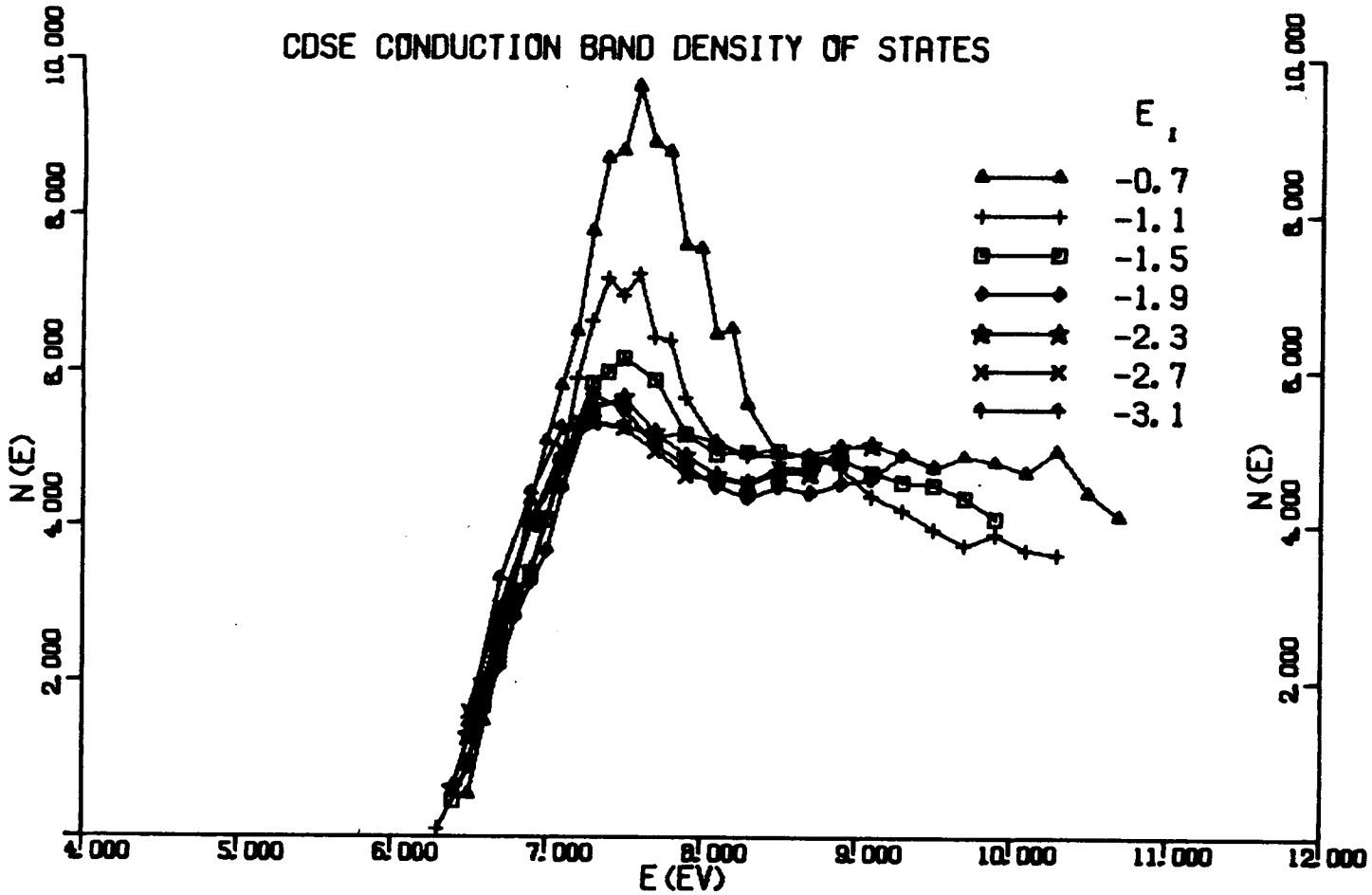

FIG. 49. CdSe EFFECTIVE CONDUCTION BAND DENSITY OF STATES DETERMINED BY DENSITY OF STATES ANALYSIS OF HIGH-VACUUM PHOTOEMISSION DATA. E_i is the energy of the initial state used to derive the effective conduction band density of states.

TABLE 5. SCALE FACTORS FOR DENSITY OF STATES ANALYSIS OF HIGH-VACUUM PHOTOEMISSION DATA FOR CdSe

E_f	$N_c^{eff}(E_f)$	E_i	$N_v(E_i)$
6.7	2.25	-0.7	3.75
7.1	4.88	-1.1	7.07
7.5	5.55	-1.5	7.57
7.9	5.26	-1.9	6.13
8.3	4.5	-2.3	4.33
8.7	4.88	-2.7	3.53
9.1	4.88	-3.1	2.88

The NDCME model explains the gross features of the photoemission from the high-vacuum-cleaved sample. Recall that if the valence band densities of states seen by various final energies superimpose and if the effective conduction band densities of states seen by various initial energies superimpose, then one must conclude that the NDCME model is sufficient to explain the photoemission data.

We can demonstrate explicitly that the NDCME model is sufficient to explain the high-vacuum photoemission data by choosing an average density of states from the results of Figs. 48 and 49 and calculating the energy distributions using

$$n(E_f) = BN_c^{eff}(E_f)N_v(E_f - \hbar\omega) \qquad (32)$$

$n(E_f)$ is the density of electrons photoemitted at an energy E_f above the top of the valence band; $N_c^{eff}(E_f)$ is the effective conduction band density of states at E_f; $N_v(E_f - \hbar\omega)$ is the valence band density of states at $E_f - \hbar\omega$; and B is an undetermined constant.

The effective density of states used to calculate the energy distributions is shown in Fig. 50. The points indicate the scale factors that were used in the density of states analysis. We compare the calculated curves with experimental curves in Fig. 51. The experimental curves have

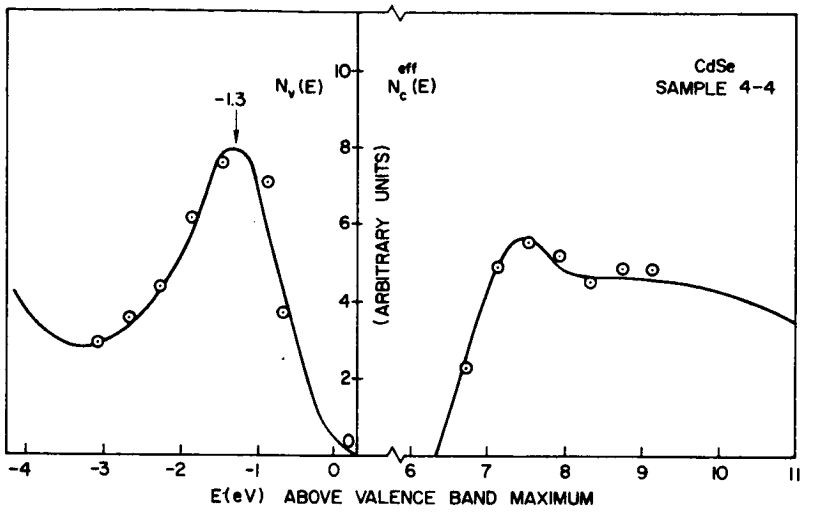

FIG. 50. CdSe EFFECTIVE DENSITY OF STATES USED TO CALCULATE ENERGY DISTRIBUTIONS FOR HIGH-VACUUM-CLEAVED SAMPLE. Points indicate the scale factors used in the density of states analysis.

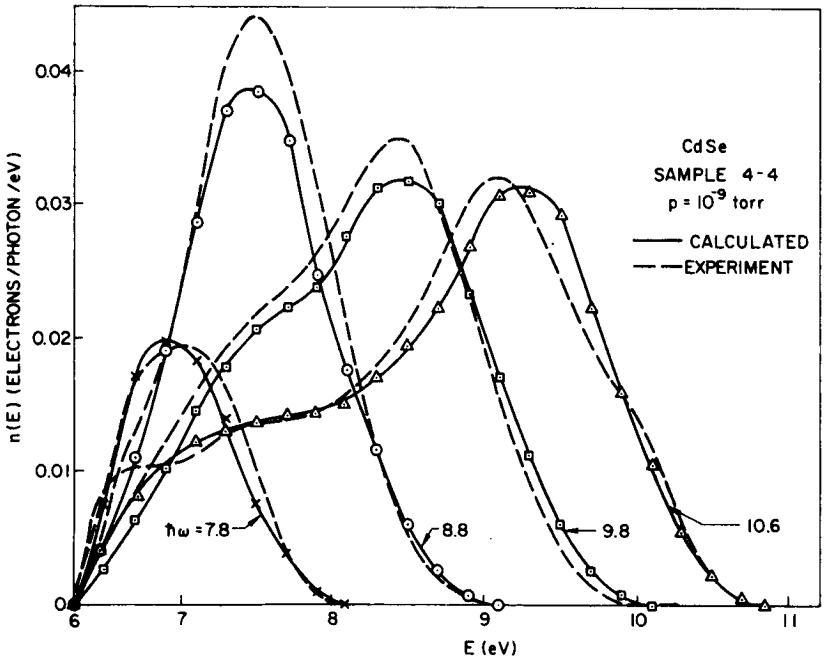

FIG. 51. COMPARISON OF CALCULATED AND MEASURED ENERGY DISTRIBUTIONS. Calculated curves result from Eq. (32) and the effective density of states in Fig. 50.

been normalized to yield but the calculated curves are identically the result of using Eq. (32) with the value of B chosen for the best fit. The very good agreement is explicit demonstration that the NDCME model is sufficient to explain most of the photoemission for the high-vacuum-cleaved sample.

Although most of the photoemission for the high-vacuum-cleaved sample is explained by the NDCME model, it remains to be explained why the conduction band density of states seen by $E_i = -0.7$ eV lies above the conduction band densities of states seen by other initial states (Fig. 49). This enhancement cannot be explained by the appearance of secondary electrons in the energy distributions, since an electron must lose at least a band gap energy (1.8 eV) in an electron-electron scattering event. We conclude that the transitions from initial states near the top of the valence band to final states near 7.5 eV are enhanced by as much as a factor of 2 over the prediction of the NDCME model alone. In other words, up to one-half of these electrons are the result of matrix-element-dependent transitions.

It is interesting to note that these matrix-element-dependent transitions are not very apparent in Fig. 51. The reason is that they actually are not very numerous. Although the enhancement is significant for initial states within about 0.7 eV of the valence band maximum, we see in Fig. 48 that the valence band density of states is quite small in this region.

2. Low-Vacuum Data

We have performed the density of states analysis on the photoemission data for the sample cleaved at a pressure of 10^{-4} torr, and the results are shown in Figs. 52 and 53. In Table 6 we present the scale factors used in this analysis. As mentioned in Sec. B1, the effects of the poorer vacuum are (1) a lowering of the electron affinity by more than one volt, and (2) the appearance of a large number of secondary electrons in the energy distributions. The latter effect has a large influence on the derived valence band density of states below about -2.2 eV. Comparing the valence band density of states for the high-vacuum sample (Fig. 48) and for the low-vacuum sample (Fig. 52), we find that for energies less than about -2.2 eV there is a large apparent valence band density of states

TABLE 6. SCALE FACTORS FOR DENSITY OF STATES ANALYSIS OF LOW-VACUUM PHOTOEMISSION DATA FOR CdSe

E_f	$N_c^{eff}(E_f)$	E_i	$N_v(E_i)$
5.1	6.2	-0.5	2.78
5.5	8.0	-0.9	5.52
5.9	8.1	-1.3	6.69
6.3	6.6	-1.7	6.57
6.7	6.6	-2.1	6.04
7.1	6.6	-2.5	5.43
7.5	6.33	-2.9	5.24
7.9	5.61		
8.3	4.82		
8.7	4.28		

for the low-vacuum data that is not seen in the high-vacuum data. This effect is due to the appearance of secondary electrons in the energy distributions. We show in Chapter VII, Sec. A, that there are more secondary electrons produced internally in the low-vacuum-cleaved sample than in the high-vacuum-cleaved sample.

The valence band densities of states seen by final states above 7.1 eV nearly superimpose (Fig. 52). The effective conduction band densities of states above 7.1 eV also nearly superimpose (Fig. 53). Therefore, the NDCME model is sufficient to explain most of the low-vacuum photoemission for final states above 7.1 eV. These results for final states above 7.1 eV agree with the results for the high-vacuum cleavage (Sec. C1).

The lower electron affinity for the low-vacuum-cleaved sample allows us to observe strong matrix-element-dependent transitions that are not observed in the high-vacuum-cleaved sample. It is apparent from Figs. 52 and 53 that transitions to final states below 7.1 eV cannot be explained by a NDCME model. The matrix elements coupling initial states near the top of the valence band to final states in the region $4.5 < E_f < 7.1$ eV are much weaker than the matrix elements coupling deeper

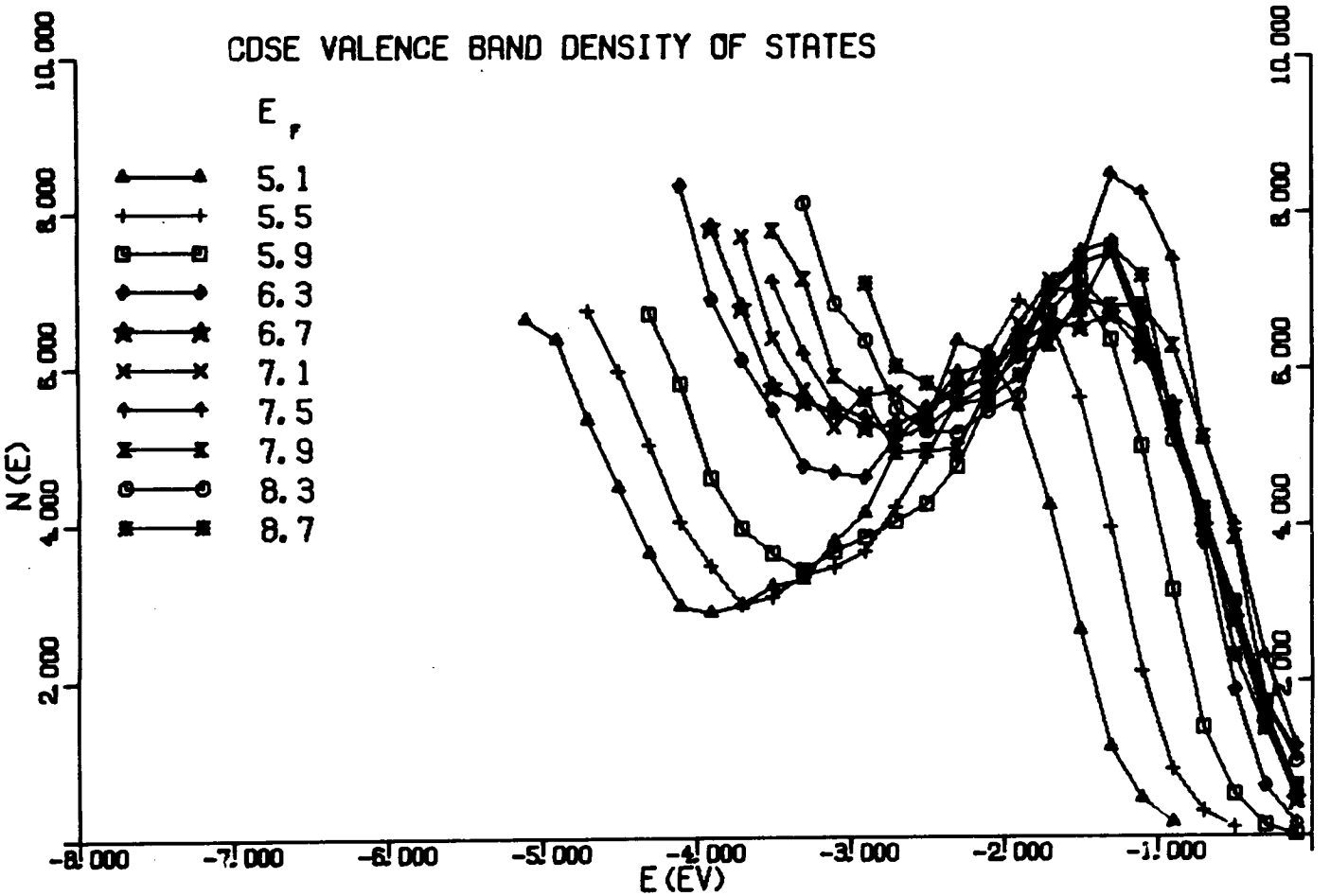

FIG. 52. CdSe VALENCE BAND DENSITY OF STATES DETERMINED BY DENSITY OF STATES ANALYSIS OF LOW-VACUUM PHOTOEMISSION DATA. E_f is the energy of the conduction band state used to derive the valence band density of states.

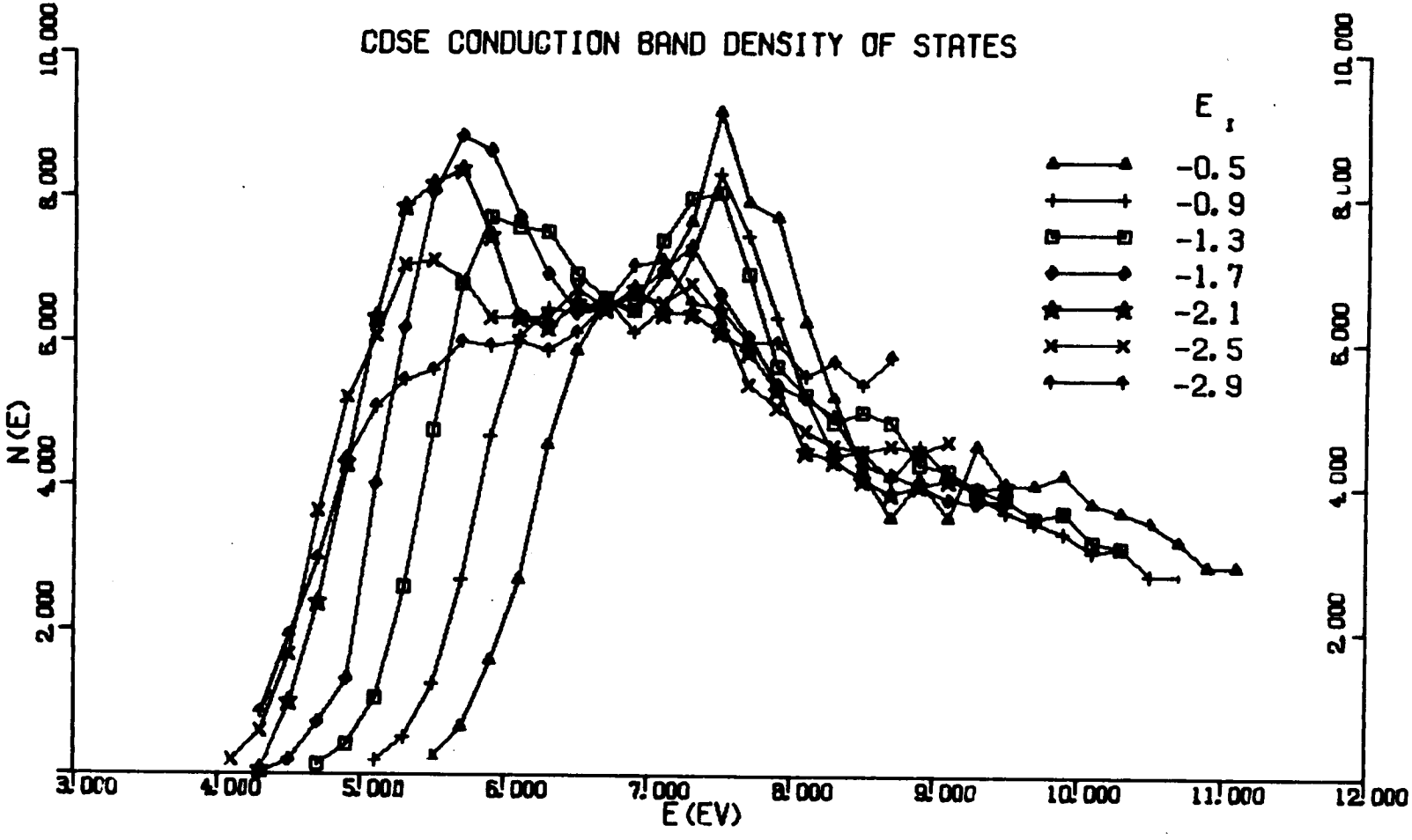

FIG. 53. CdSe EFFECTIVE CONDUCTION BAND DENSITY OF STATES DETERMINED BY DENSITY OF STATES ANALYSIS OF LOW-VACUUM PHOTOEMISSION DATA. E_i is the energy of the initial state used to derive the effective conduction band density of states.

valence band states to these same final states. Of course, for $-1.8 < E_i < 0$ the differences among the curves of Fig. 53 cannot be due to the appearance of secondary electrons in the energy distributions since the minimum energy loss through electron-electron scattering is equal to the band gap (1.8 eV).

There is a very striking feature about the low-vacuum photoemission data, but it is not at all apparent in Figs. 52 and 53. The following analysis is intended to bring out this feature. Let us define the function $f(E_f,\hbar\omega)$ by

$$n(E_f) = N_c^{eff}(E_f)N_v(E_f - \hbar\omega)f(E_f,\hbar\omega) \tag{33}$$

For a photon energy $\hbar\omega$, the density of photoemitted electrons at energy E_f is not given by $N_c^{eff}(E_f)N_v(E_f - \hbar\omega)$, but rather this product of densities of states must be multiplied by $f(E_f,\hbar\omega)$, the <u>strength of coupling</u> between initial and final states. If the NDCME model were sufficient to explain the photoemission, then $f(E_f,\hbar\omega)$ would be equal to a constant for all E_f and $\hbar\omega$. When the density of states model is not sufficient, then in general, the function f for one final energy will not be simply related to the function f for another final energy.

Obviously, there is a considerable amount of arbitrariness in the choice of N_c^{eff}, N_v, and f. For any arbitrary N_c^{eff} and N_v, a set of f's can be constructed such that Eq. (33) reproduces the photoemission data. The feature we wish to point out is that, for one particular choice of N_c^{eff} and N_v, f has a very simple form. Using the effective density of states shown in Fig. 54, we derive the strength of coupling shown in Fig. 55 by plotting the quantity

$$f(E_f,\hbar\omega) = \frac{n(E_f)}{N_c^{eff}(E_f)N_v(E_f - \hbar\omega)} \tag{34}$$

for various final energies E_f. We only use photoemission data for $E_i > -2.0$ eV; hence there are negligibly few contributions to Fig. 55 due to secondary electrons. The striking feature about Fig. 55 is that for final energies below about 7.1 eV, the strength of coupling

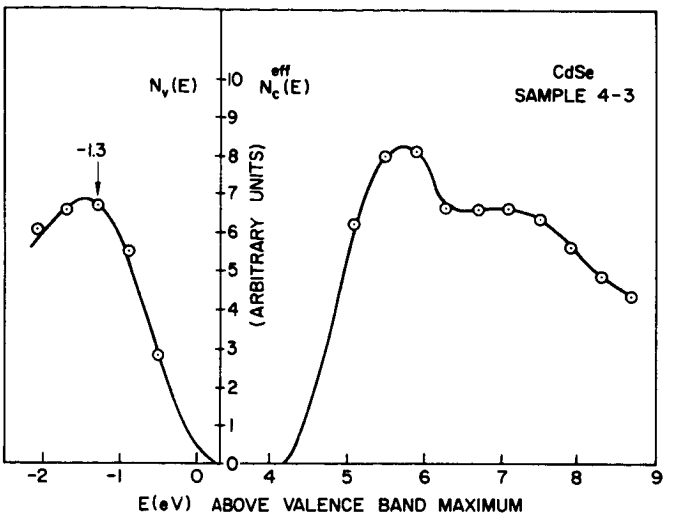

FIG. 54. CdSe EFFECTIVE DENSITY OF STATES USED IN EQ. (34) TO DERIVE THE STRENGTH OF COUPLING FOR LOW-VACUUM-CLEAVED SAMPLE (FIG. 55). Points indicate the scale factors used in the density of states analysis.

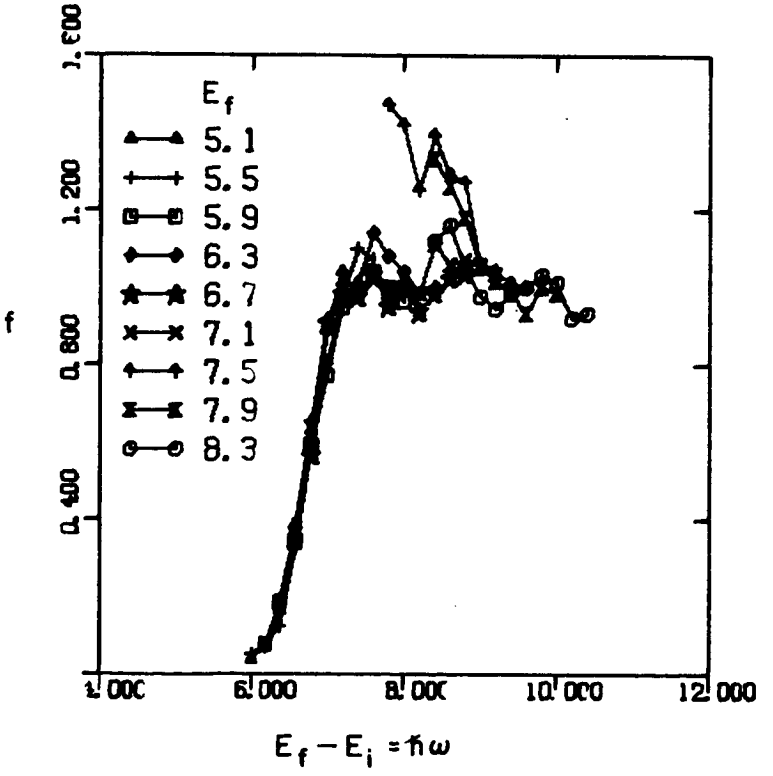

FIG. 55. STRENGTH OF COUPLING BETWEEN INITIAL AND FINAL STATES. E_f is the energy of the final state used in Eq. (34).

is a function of $\hbar\omega$ only and rises by a factor of 20 between $\hbar\omega$ = 6.0 eV and 7.2 eV. This factor of 20 is more than an order of magnitude larger than either the uncertainty in the yield measurement or any correction to the density of states analysis due to optical data (see introductory remarks in this section). Rather, states near the top of the valence band are very weakly coupled to final states between 4.5 and 7.1 eV. It can also be seen in Fig. 55 that transitions to final states near 7.5 eV are enhanced above the predictions of a NDCME model alone.

D. DISCUSSION OF BAND STRUCTURE AND OPTICAL PROPERTIES

In this section we discuss the electronic band structure and optical properties of CdSe using features of the electronic structure determined from the photoemission data. A complete understanding of the electronic properties of CdSe is hampered by the lack of a detailed band structure calculation.

In earlier sections we showed that the photoemission from CdSe is due to both NDCME and matrix-element-dependent transitions. Very few of these matrix-element-dependent transitions are necessarily direct transitions. Only the peak DT (Figs. 39 and 40) showed motion characteristic of direct transitions. As discussed in Sec. B1, the disappearance of the peak CB2 (Fig 40) may also be the result of direct transitions.

Matrix-element-dependent transitions have a large influence on the optical properties of CdSe. We present in Fig. 56 the reflectivity of CdSe (CARDONA and HARBEKE, 1965). We have already presented in Fig. 47 the quantities $\epsilon_2\omega^2$ and $n\omega$ which we have derived from the data of CARDONA and HARBEKE. The rapid rise in reflectivity and $\epsilon_2\omega^2$ for $6 < \hbar\omega < 7.2$ eV is due to the factor of 20 increase in the strength of coupling to final states near 5.8 eV (Fig. 55).

NDCME transitions also influence the optical properties of CdSe. For photon energies near 8.8 eV, there are NDCME transitions from a peak at -1.3 eV in the valence band density of states to conduction band states near 7.5 eV (Figs. 40 and 45). The corresponding features of the optical data are a peak in the reflectivity at 8.5 eV (E_1' in Fig. 56) and a peak in $\epsilon_2\omega^2$ at 8.3 eV (Fig. 47). It is clear from the density of states analysis (Sec. C) that the "background" of the optical data

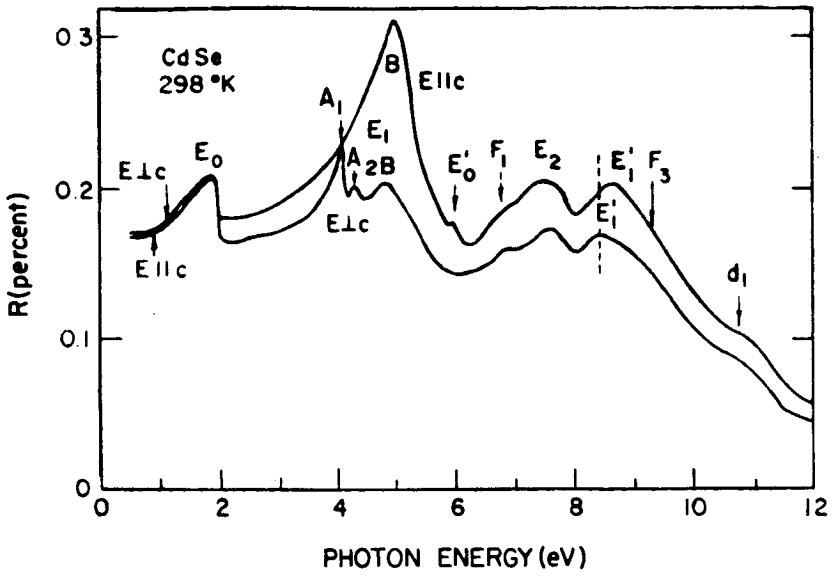

FIG. 56. REFLECTIVITY OF CdSe (CARDONA AND HARBEKE, 1965).

for photon energies near 8.8 eV is due to NDCME transitions. However, the peaks in the optical data near 8.8 eV are probably due to the matrix-element enhancement observed in the density of states analysis (Figs. 49 and 53) for transitions to final states near 7.5 eV.

When it first appears, the shoulder S in the energy distributions for $\hbar\omega > 10.2$ eV (Fig. 46) is due to transitions to final states near 10.2 eV. Although the photoemission data are not definitive, it is likely that S is due to direct transitions to final states near 10.2 eV (see Sec. B2). The corresponding feature of the reflectivity is a peak at 10.7 eV (d_1 in Fig. 56), which PHILLIPS (1964) has assigned in zinc blende materials to $L_3^v - L_1$ transitions. The corresponding transition in wurtzite materials is $\Gamma_6^v - \Gamma_3$. If this interpretation is correct, the photoemission data locate Γ_3 at about 10.2 eV above the top of the valence band.

The curves of Fig. 48 for $-3 < E < 0$ are probably quite close to the actual valence band density of states. The rise for $E < -3.5$ eV is most likely due to the appearance of secondary electrons in the energy distributions. It is more difficult to estimate the conduction band density of states. Even in the simplest case, the effective conduction band

density of states is the product of the actual conduction band density of states, a threshold function, and an escape depth (see Chapter II, Sec. D1). The last two quantities are unknown functions of electron energy. Nonetheless, special features of the effective density of states (peaks, dips, etc.) can usually be attributed to the actual conduction band density of states. Since the electron affinity is much lower for the low-vacuum-cleaved sample, the best estimate of the conduction band density of states is obtained from Fig. 53.

E. CONCLUSIONS

A principal conclusion of this study of CdSe is that the photoemission and optical properties of CdSe are due to a mixture of NDCME transitions and matrix-element-dependent transitions. However, very few of these matrix-element-dependent transitions have been positively identified as direct transitions. The rise in reflectivity and $\epsilon_2\omega^2$ for $6 < \hbar\omega < 7.2$ eV is due to the factor of 20 rise in the strength of coupling to conduction band states near 5.8 eV. Yet the peak in reflectivity at 8.5 eV (E_1') and the peak in $\epsilon_2\omega^2$ at 8.3 eV are to a large extent due to the NDCME transitions from a peak at -1.3 eV in the valence band density of states to final states near 7.5 eV. The features of the optical properties are therefore determined by both NDCME transitions and matrix-element-dependent transitions.

Most of the photoemission from the high-vacuum-cleaved sample is successfully explained by the NDCME model. Using the density of states analysis we determined the valence band density of states and the effective conduction band density of states. For the high-vacuum data the success of the NDCME model was explicitly demonstrated by comparing experimental data and energy distributions calculated from the derived density of states.

The lower electron affinity of the low-vacuum-cleaved sample allows us to observe the strong matrix-element-dependent transitions to final states below 7.1 eV. The strength of coupling to these final states rises by a factor of 20 in the region $6 < \hbar\omega < 7.2$ eV. States near the top of the valence band are very weakly coupled to final states near 5.8 eV.

For both high- and low-vacuum data, we observed that states near the top of the valence band are strongly coupled to conduction band states near 7.5 eV. In the density of states analyses we find that these transitions are enhanced up to a factor of 2 over the predictions of the NDCME model. However, since the valence band density of states is weak near the top of the valence band, there is a relatively small number of these transitions.

The small peak DT is due to direct transitions. DT moves by 1.7 eV while the photon energy changes by 3.2 eV. However, we are unable to determine where in $\bar{k}$-space these transitions occur, because we lack a detailed band structure calculation for CdSe. The shoulder S that appears in the energy distributions for $\hbar\omega > 10.2$ eV corresponds to the d_1 reflectivity peak at 10.7 eV. This structure has been tentatively assigned to transitions to conduction band states near Γ_3. If this assignment is correct, the photoemission data locate Γ_3 at 10.2 eV.

The photoemission data have located a valence band at -9.9 eV. We suggest that these valence band states are derived from cadmium 4d states.

Lastly, we have attempted to determine whether or not the lower electron affinity for the low-vacuum-cleaved sample is due to the gaseous hydrogen in the monochromator. A high-vacuum-cleaved sample of CdSe was exposed to a 5-micron pressure of ultrapure Linde hydrogen in the high-vacuum chamber. The yield and energy distributions measured while the sample was exposed to the hydrogen were indistinguishable from the measurements before the high-vacuum cleavage was exposed to the hydrogen. Therefore the lower electron affinity is not due to the hydrogen in the monochromator.

VI. PHOTOEMISSION FROM CdS

In this chapter the data obtained from photoemission studies of CdS are presented and interpreted. The photoemission experiments have been performed on single crystals cleaved in high vacuum (pressure = 10^{-9} torr) and in low vacuum (pressure = 10^{-4} torr). For experimental details see Chapter III. A larger region of the conduction band is exposed in the low-vacuum experiments, since the electron affinity is more than a volt lower than in the high-vacuum experiments.

In Secs. A and B of this chapter, the CdS quantum yield and energy distributions are presented and discussed. In Sec. C the density of states analysis (see Chapter II, Sec. D) is applied to the CdS photoemission data. We explicitly show that the NDCME model is sufficient to explain most of the high-vacuum data. However, the NDCME model is not sufficient to explain the transitions to conduction band states exposed only in the low-vacuum experiments. We determine the matrix-element variation required to explain this low-vacuum photoemission data. In Sec. D we discuss the band structure and optical properties of CdS in light of the photoemission data.

KINDIG and SPICER (1965a), hereafter referred to as KS, have presented CdS energy distributions that are indistinguishable from the present work; also their relative yield is never more than a factor of 2 different from ours. KS found that the gross features of the CdS photoemission data were explained by the NDCME model for electronic excitation (KS refer to the NDCME model as "nondirect transitions"). We find that, in addition to the NDCME transitions, there are strong matrix-element-dependent transitions in CdS. However, there is no evidence that these are direct transitions.

The features of the CdS photoemission data are remarkably similar to those of CdSe (Chapter V). Both are entirely different from the CdTe photoemission data (Chapter IV). Rather than present the CdSe and CdS results in a single chapter, we present the CdS results separately so that we may compare them to the earlier studies of CdS by KS.

A. QUANTUM YIELD

We present in Fig. 57 the spectral distribution of the quantum yield for a CdS crystal cleaved in high vacuum and for the same crystal cleaved in low vacuum. In the low-vacuum experiment the sample was exposed to a pressure of 10^{-4} torr (for details see Sec. B of Chapter III). This resulted in an electron affinity more than a volt lower than for the sample cleaved at a pressure of 10^{-9} torr. There also resulted a rise in yield for photon energies greater than about 10.2 eV, with a maximum low-vacuum yield about four times as large as the maximum high-vacuum yield. We believe that the rise in yield is due to the escape of secondary electrons; however, we defer to Chapter VII a discussion of the evidence for this interpretation.

The two curves of Fig. 57 were measured using the Cs_3Sb standard for measuring light intensity (Sec. B1, Chapter III). This same standard

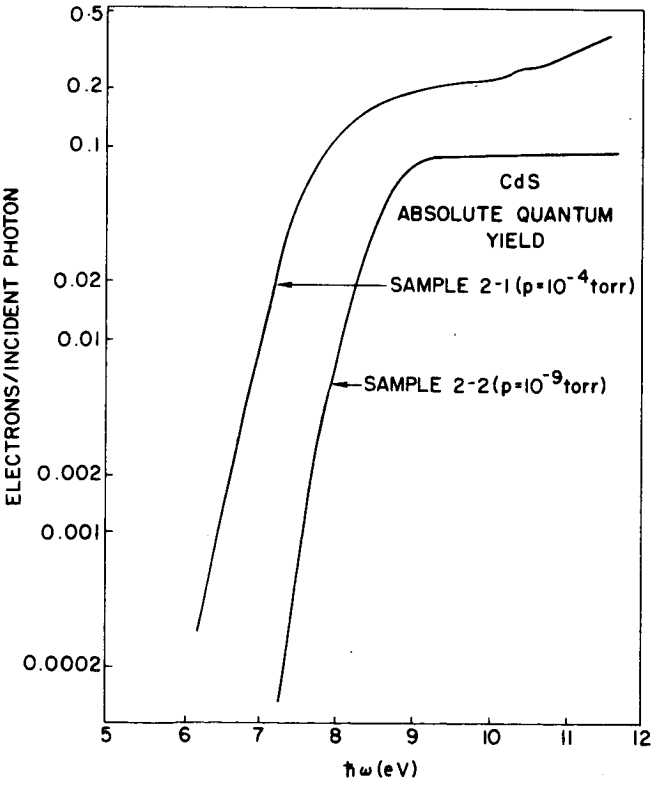

FIG. 57. ABSOLUTE QUANTUM YIELD OF CdS FOR A PHOTON ENERGY $\hbar\omega$.

was used for both high- and low-vacuum CdSe experiments (Chapter V), and for the CdTe low-vacuum experiment (Chapter IV). As discussed in Chapter III, the relative response of the standard as a function of photon energy was determined assuming that the efficiency of sodium salicylate is independent of photon energy. The detailed shapes of the curves of Fig. 57 will therefore depend upon the uniformity of the response of sodium salicylate. Although the yield is uncertain by at most 15 percent over any 1 eV range in $\hbar\omega$, for a given photon energy the ratio of the high-vacuum yield to the low-vacuum yield should be correct to within a few percent, since both measurements used the same standard.

B. ENERGY DISTRIBUTIONS OF PHOTOEMITTED ELECTRONS

1. Low-Vacuum Experiments

In Figs. 58 through 63 we present the energy distributions of the photoemitted electrons for the sample cleaved at a pressure of 10^{-4} torr. Except for $\hbar\omega$ = 16.8 and 21.2 eV, all energy distributions are

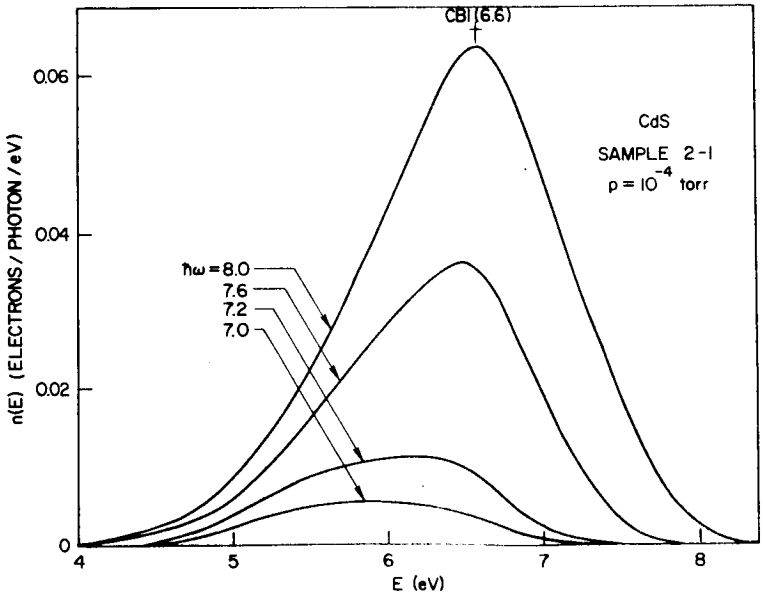

FIG. 58. NORMALIZED ENERGY DISTRIBUTIONS OF PHOTOEMITTED ELECTRONS FROM CdS FOR $7.0 \leq \hbar\omega \leq 8.0$ eV. Electron energy E is measured relative to the valence band maximum.

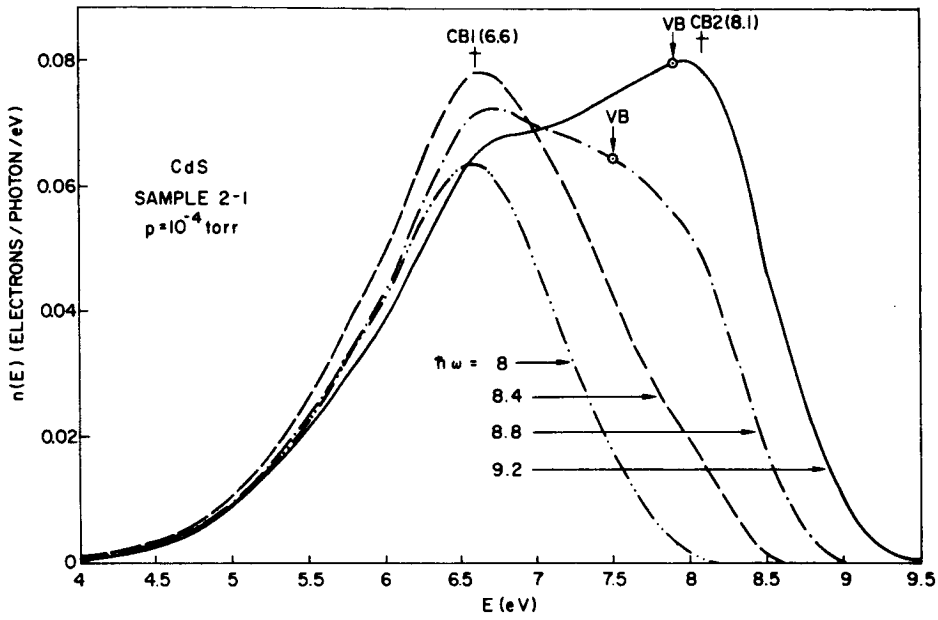

FIG. 59. NORMALIZED ENERGY DISTRIBUTIONS OF PHOTOEMITTED ELECTRONS FROM CdS FOR $8.0 \leq \hbar\omega \leq 9.2$ eV. Electron energy E is measured relative to the valence band maximum.

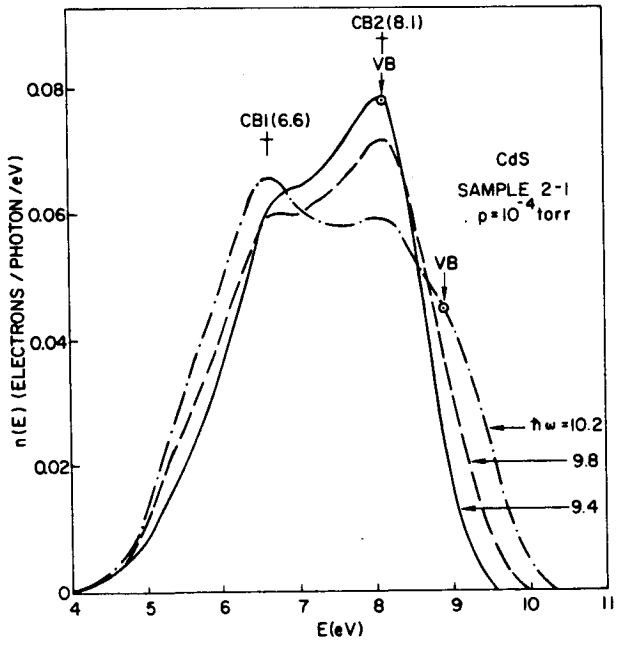

FIG. 60. NORMALIZED ENERGY DISTRIBUTIONS OF PHOTOEMITTED ELECTRONS FROM CdS FOR $9.4 \leq \hbar\omega \leq 10.2$ eV. Electron energy E is measured relative to the valence band maximum.

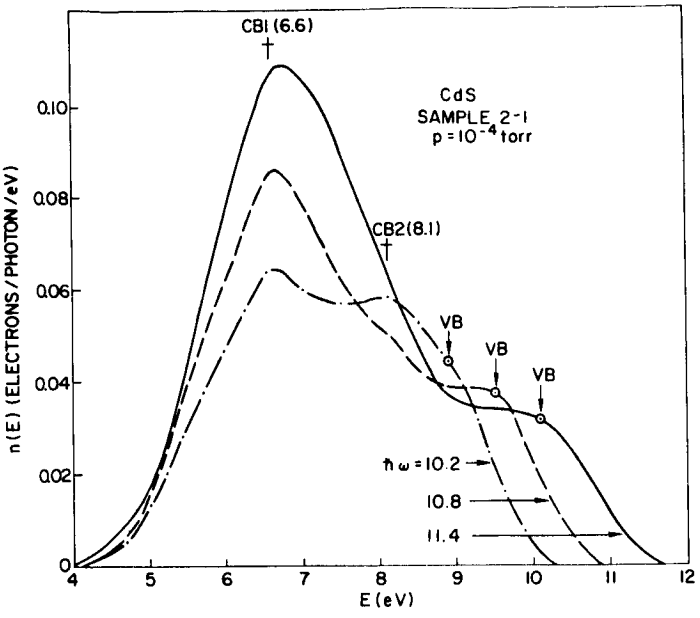

FIG. 61. NORMALIZED ENERGY DISTRIBUTIONS OF PHOTOEMITTED ELECTRONS FROM CdS FOR $\hbar\omega \geq 10.2$ eV. Electron energy E is measured relative to the valence band maximum.

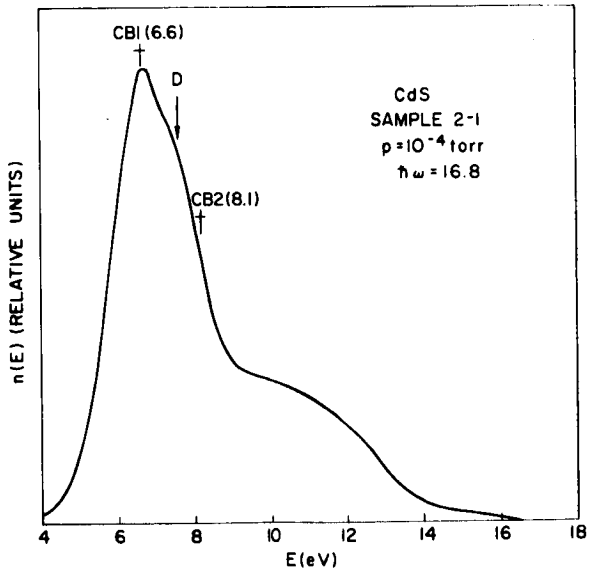

FIG. 62. ENERGY DISTRIBUTION OF PHOTOEMITTED ELECTRONS FROM CdS FOR $\hbar\omega = 16.8$ eV. Electron energy E is measured relative to the valence band maximum.

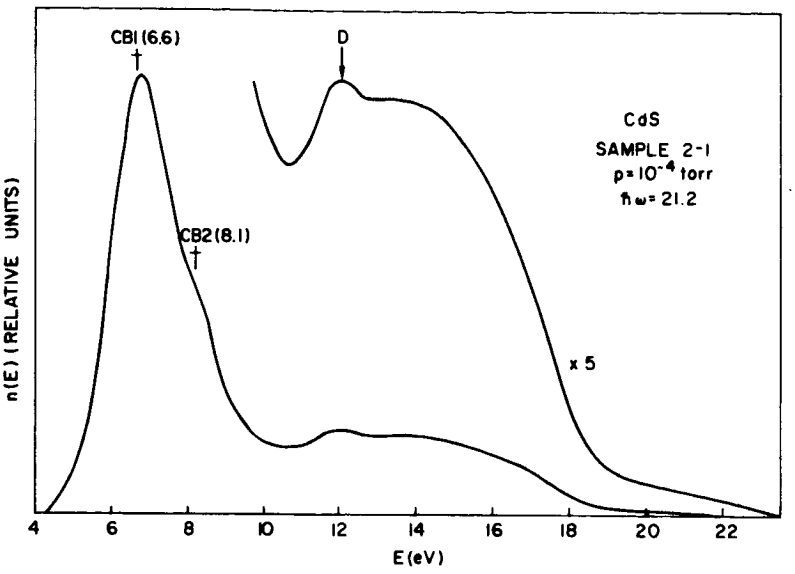

FIG. 63. ENERGY DISTRIBUTION OF PHOTOEMITTED ELECTRONS FROM CdS FOR $\hbar\omega = 21.2$ eV. Electron energy E is measured relative to the valence band maximum.

normalized to the quantum yield. Electron energies are stated relative to the valence band maximum; the calibration of the energy scale was discussed in Chapter III, Sec. B3. We show in Chapter VII that the large number of low-energy electrons appearing in the energy distributions for $\hbar\omega > 10.2$ eV are secondary electrons.

Both NDCME and matrix-element-dependent transitions are observed in the photoemission data (the characteristics of NDCME, direct, and other matrix-element-dependent transitions are discussed in Chapter II, Secs. C1 and C2). The observed matrix-element-dependent transitions are not necessarily direct transitions.

For $\hbar\omega \geq 8.8$ eV, a peak of electrons labeled VB appears in the energy distributions (Figs. 59 to 61). For a photon energy $\hbar\omega$, this peak is indicated by an arrow at an energy

$$E = \hbar\omega - 1.3 \text{ eV} \tag{35}$$

The motion of the peak of electrons VB in accordance with Eq. (35) is characteristic of NDCME transitions from a peak at -1.3 eV in the valence band density of states (Chapter II, Sec. C2). This motion indicates

that conservation of $\bar{K}$ is not an important selection rule for the transitions associated with peak VB.

For $\hbar\omega = 9.4$ eV valence band states near -1.3 eV are strongly coupled to conduction band states CB2 at 8.1 eV; this leads to the peak CB2 at 8.1 eV. For $\hbar\omega > 9.4$ eV, the peak of electrons VB moves to higher energies and a peak of electrons CB2 remains at 8.1 eV. This latter peak is due to NDCME transitions to a peak at 8.1 eV in the conduction band density of states (Chapter II, Sec. C2).

We now discuss the qualitative features of the matrix-element-dependent transitions. The matrix-element variation will be more clearly displayed by the density of states analysis in Sec. C. In Fig. 58 we see that the number of electrons excited to 6.6 eV (CB1) from initial states at -0.4 eV ($\hbar\omega = 7.0$ eV) is 1/10 of the number excited from -1.0 eV ($\hbar\omega = 7.6$ eV) and 1/20 of the number excited from -1.4 ($\hbar\omega = 8.0$ eV). It is apparent from the shape of the peak VB that the valence band density of states does not show this sharp rise. Rather, the matrix elements that couple states near the top of the valence band to final states near 6.6 eV are much weaker than the matrix elements that couple deeper valence band states to these same final states.

In Figs. 62 and 63 we present the energy distributions of the photoemitted electrons for $\hbar\omega = 16.8$ and 21.2 eV. Many of these photoelectrons have been electron-electron scattered to conduction band states near CB1 and CB2. The peak D at an energy of 12 eV for $\hbar\omega = 21.2$ eV is believed to be due to transitions from a high density of states at -9.2 eV in the valence band. KINDIG and SPICER (1965a) suggested that these valence band states are derived from cadmium 4d states. The location of the d-band is discussed in more detail in Chapter VII, Sec. C.

It is not possible to follow the motion of peak D over a wide range of photon energy to confirm its origin in the valence band; however, if the peak were due to conduction band structure near 12 eV, we would also expect to see a peak at 12 eV for $\hbar\omega = 16.8$ eV. No such peak is seen in Fig. 62. If peak D is in fact due to transitions from valence band states at -9.2 eV, then this peak should be seen at 7.6 eV for $\hbar\omega = 16.8$ eV. The structure labeled D at 7.6 eV in Fig. 62 is believed to be due to these transitions.

2. High-Vacuum Experiments

In Figs. 64 through 67 we present energy distributions for a sample cleaved in a vacuum of 10^{-9} torr. There is a striking difference between these curves and the energy distributions for the same sample

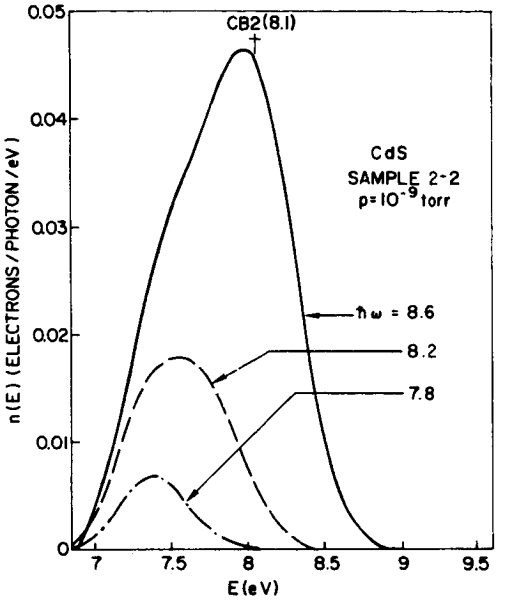

FIG. 64. NORMALIZED ENERGY DISTRIBUTIONS OF PHOTOEMITTED ELECTRONS FROM CdS FOR $7.8 \leq \hbar\omega \leq 8.6$ eV. Electron energy E is measured relative to the valence band maximum.

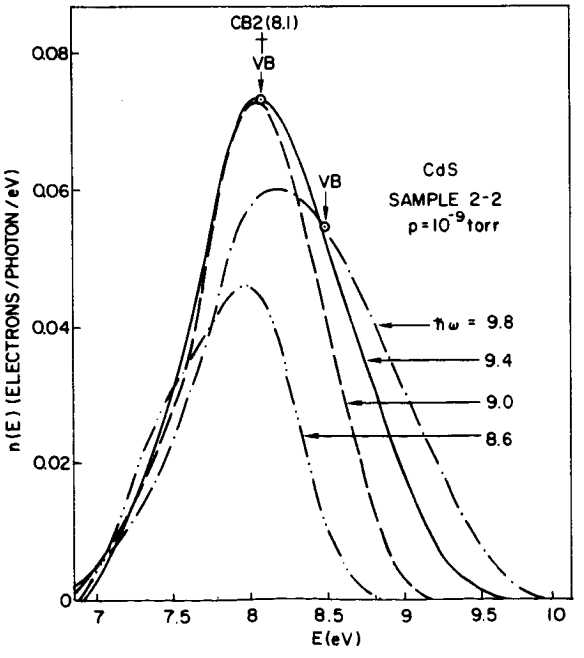

FIG. 65. NORMALIZED ENERGY DISTRIBUTIONS OF PHOTOEMITTED ELECTRONS FROM CdS FOR $8.6 \leq \hbar\omega \leq 9.8$ eV. Electron energy E is measured relative to the valence band maximum.

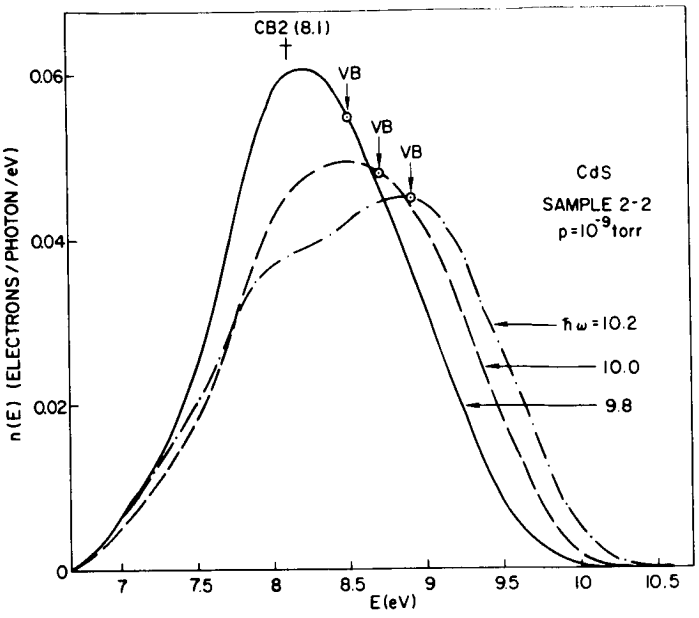

FIG. 66. NORMALIZED ENERGY DISTRIBUTIONS OF PHOTOEMITTED ELECTRONS FROM CdS FOR $9.8 \leq \hbar\omega \leq 10.2$ eV. Electron energy E is measured relative to the valence band maximum.

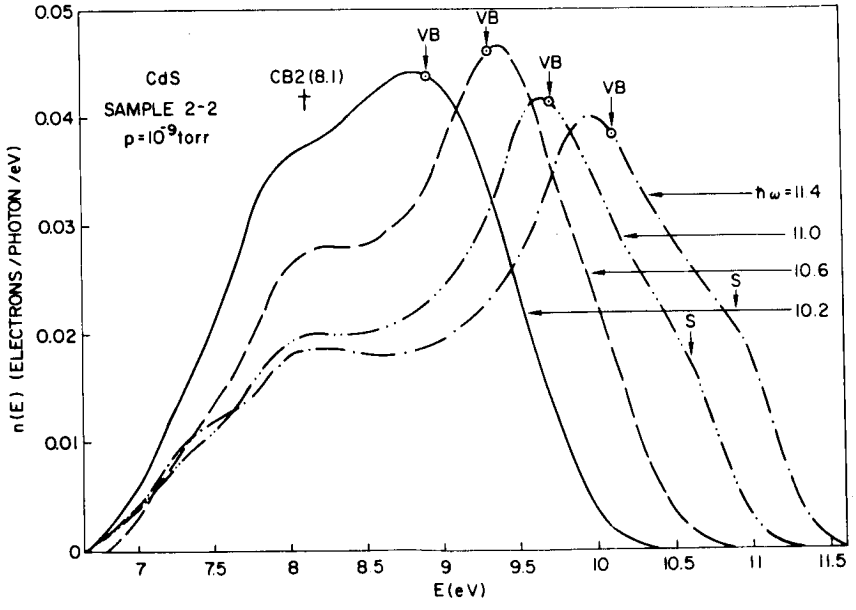

FIG. 67. NORMALIZED ENERGY DISTRIBUTIONS OF PHOTOEMITTED ELECTRONS FROM CdS FOR $\hbar\omega \geq 10.2$ eV. Electron energy E is measured relative to the valence band maximum.

cleaved in low vacuum (Sec. B1). The electron affinity is more than one volt higher for this high-vacuum cleavage than for the same sample cleaved in the low vacuum. In addition, the number of secondary electrons appearing in the energy distributions is much smaller than for the low-vacuum-cleaved sample. For the high-vacuum cleavage no structure is observed at CB1 (6.6 eV) since these states now lie below the vacuum level due to the increased electron affinity. Hence the matrix-element-dependent transitions to these final states are not observed in the high-vacuum experiments.

As in the low-vacuum data (Sec. B1), the peak of electrons labeled VB (Figs. 65 to 67) moves in accordance with Eq. (35). This peak is due to NDCME transitions from a peak at -1.3 eV in the valence band density of states. This motion indicates that conservation of $\bar{K}$ is not an important selection rule for the transitions associated with the peak VB. At high photon energies, the peak of electrons falls slightly behind the arrows which are determined by Eq. (35). This would result if a small portion of peak VB were due to direct transitions. The peak VB would also fall behind Eq. (35) if the mean free path for electron-electron scattering were rapidly decreasing with increasing energy. However, this is not the case here since the amplitude of the peak VB is not rapidly decreasing with increasing energy as it would if the mean free path for electron-electron scattering were rapidly decreasing.

As in the low-vacuum data (Sec. B1), for $\hbar\omega = 9.4$ eV the peak in the valence band density of states at -1.3 eV is strongly coupled to conduction band states near 8.1 eV. We indicate with the dagger CB2 electrons photoemitted from the conduction band states near 8.1 eV.

A high-energy shoulder S appears in the energy distributions for $\hbar\omega > 10.6$ eV (Fig. 67). When it first appears, this shoulder is due to transitions from initial states near the top of the valence band to final states near 10.6 eV. The shoulder S appears to be due to direct transitions, but the data are insufficient to verify this with certainty. The features of S are very similar to the features of the shoulders S1 and S2 in the CdTe energy distributions (Chapter IV). These shoulders were shown to be due to direct transitions.

3. Effects of Hydrogen on High-Vacuum-Cleaved Surface

We have performed an experiment in which a high-vacuum-cleaved sample of CdS was exposed to a 5-micron pressure of ultrapure Linde hydrogen in the high-vacuum chamber. The yield and energy distributions measured while the sample was exposed to the hydrogen were indistinguishable from the measurements before the high-vacuum cleavage was exposed to the hydrogen. This experiment shows conclusively that the lower electron affinity and increased number of secondary electrons that are observed in the low-vacuum measurements in the monochromator (for details see Chapter III) are neither due to adsorbed hydrogen on the surface nor to hydrogen that has diffused into the crystal.

C. DENSITY OF STATES ANALYSIS OF CdS PHOTOEMISSION DATA

The qualitative analysis in the previous section indicated that the photoemission from CdS is the result of a mixture of NDCME and matrix-element-dependent transitions. In this section we shall use the density of states analysis to (1) explicitly demonstrate the simultaneous presence of both types of transitions, and (2) separate the effects of the NDCME transitions from the effects of the matrix-element-dependent transitions.

In this analysis we have not corrected for the optical data for CdS. It was shown in Chapter II that we are, in effect, assuming that $\epsilon_2\omega^2$ is approximately independent of ω if $\alpha L \gg 1$, and that $n\omega$ is approximately independent of ω if $\alpha L \ll 1$. As shown in Chapter VII, Sec. B, the low yield of about 9 percent for the high-vacuum-cleaved sample indicates that the escape depth is much shorter than the absorption depth ($\alpha L \ll 1$). We are therefore assuming that $n\omega$ is approximately independent of ω. The higher yield observed in the low-vacuum experiment is due to the escape of secondary electrons (Chapter VII). The optical data presented in Fig. 68 shows that $n\omega$ varies by at most 23 percent in the region $6 < \hbar\omega < 11.5$ eV. The analysis given in Sec. C2 shows that the matrix-element variation required to explain the low-vacuum photoemission data is more than an order of magnitude larger than this error due to the neglect of optical data.

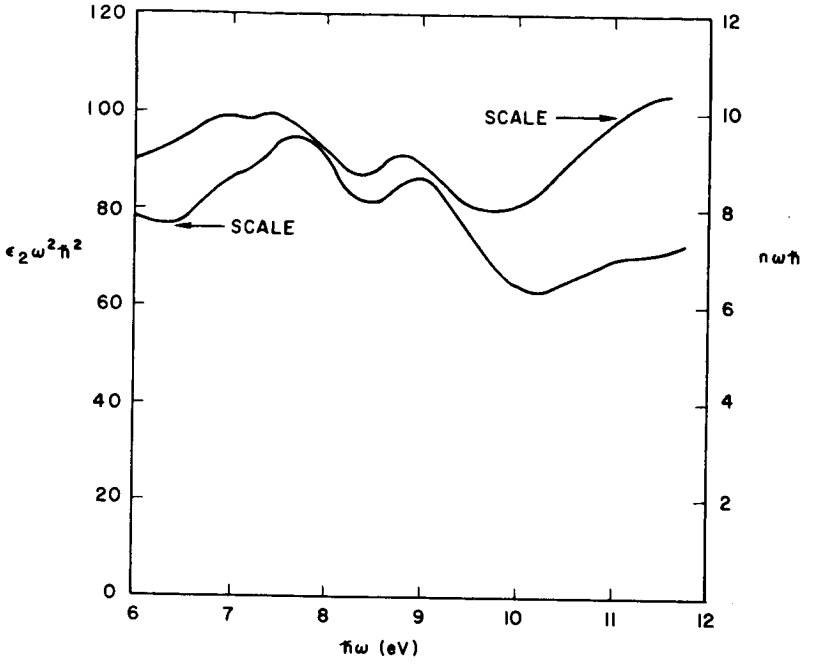

FIG. 68. OPTICAL DATA FOR CdS DERIVED FROM DATA OF CARDONA AND HARBEKE (1965).

Uncertainty in the yield measurement will also introduce error into the density of states analysis. Since the maximum uncertainty in the yield is 15 percent over a region of 1 eV in photon energy (Chapter III, Sec. B1), the maximum distortion of the density of states analysis due to the uncertainty in yield is about 15 percent over a region of 1 eV.

1. High-Vacuum Data

In Figs. 69 and 70 we present the valence band and effective conduction band densities of states derived using the data for the sample cleaved at a pressure of 10^{-9} torr. The density of states analysis is described in Chapter II, Sec. D. The scale factors used to derive the results of Figs. 69 and 70 are shown in Table 7. E_f indicates the energy of the final state used in deriving the valence band density of states. Similarly, E_i indicates the energy of the initial state used in deriving the effective conduction band density of states.

The NDCME model explains the gross features of the photoemission from the high-vacuum-cleaved sample. Recall that if the valence band densities of states seen by various final energies superimpose and the effective conduction band densities of states seen by various initial energies superimpose, then one must conclude that the NDCME model is sufficient to explain the photoemission data.

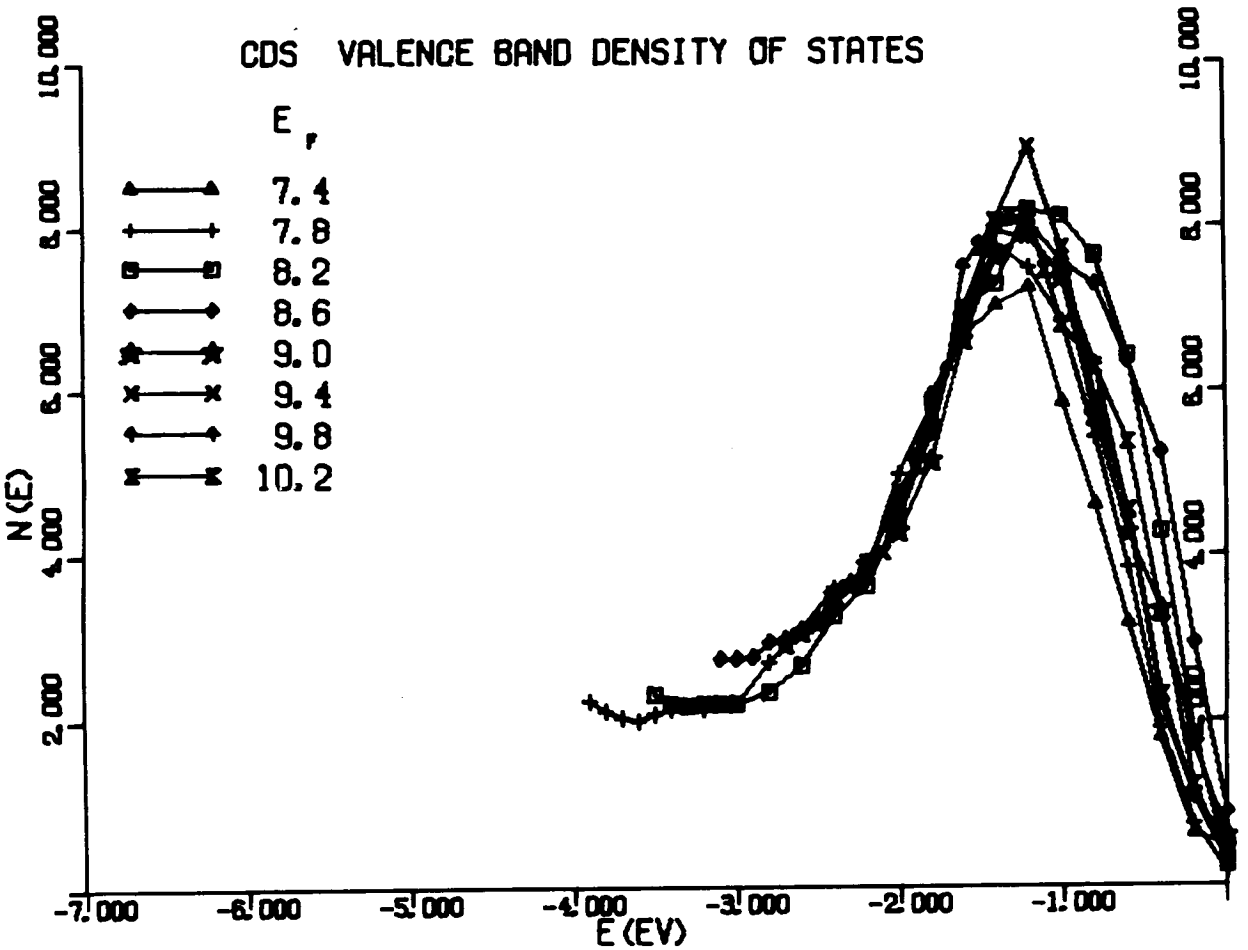

FIG. 69. CdS VALENCE BAND DENSITY OF STATES DETERMINED BY DENSITY OF STATES ANALYSIS OF HIGH-VACUUM PHOTOEMISSION DATA. E_f is the energy of the conduction band state used to derive the valence band density of states.

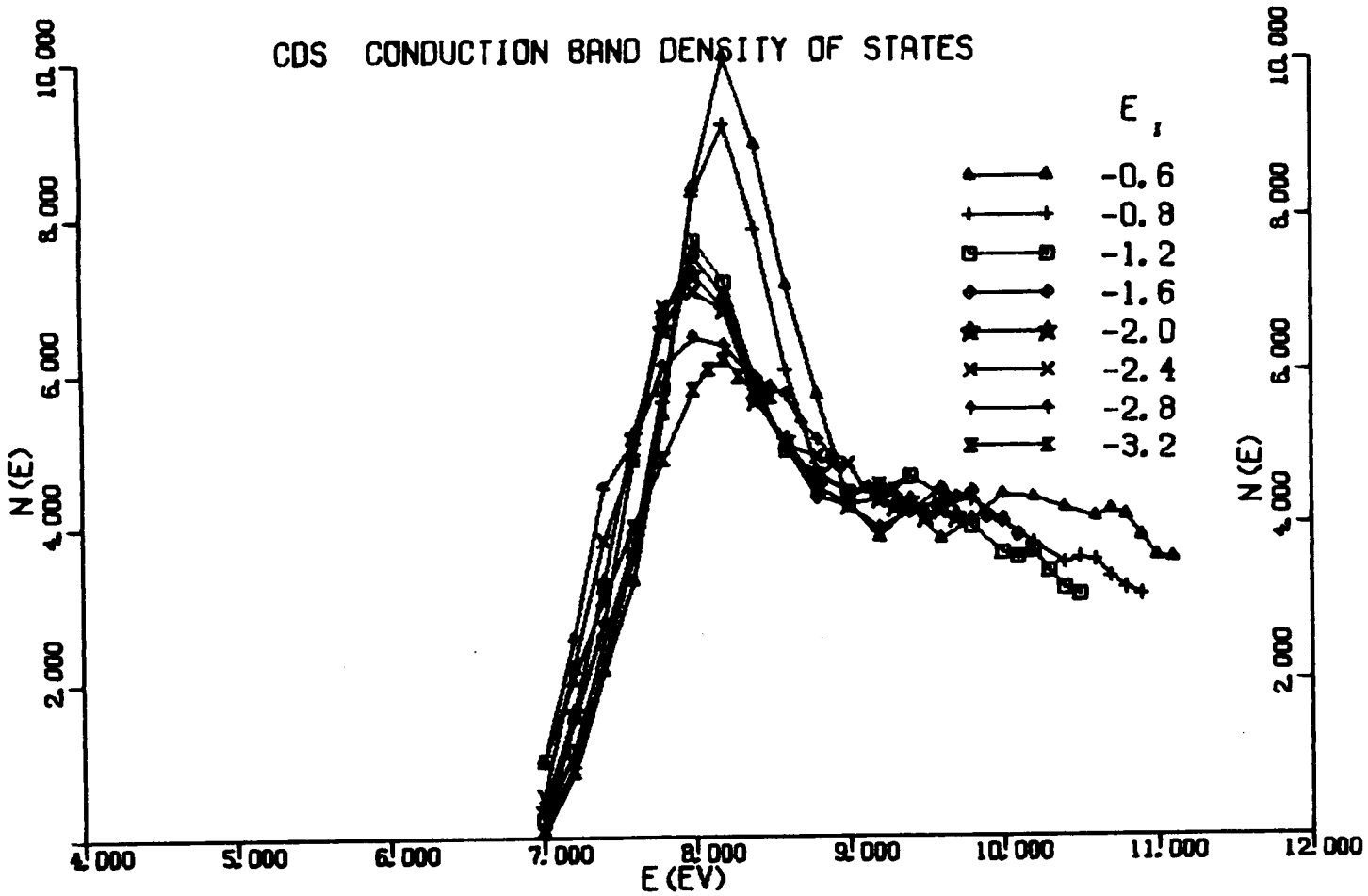

FIG. 70. CdS EFFECTIVE CONDUCTION BAND DENSITY OF STATES DETERMINED BY DENSITY OF STATES ANALYSIS OF HIGH-VACUUM PHOTOEMISSION DATA. E_i is the energy of the initial state used to derive the effective conduction band density of states.

TABLE 7. SCALE FACTORS FOR DENSITY OF STATES ANALYSIS OF HIGH-VACUUM PHOTOEMISSION DATA FOR CdS

E_i	$N_v(E_i)$	E_f	$N_c^{eff}(E_f)$
-0.6	4.44	7.4	3.0
-0.8	6.02	7.8	6.3
-1.2	8.13	8.2	7.0
-1.6	7.0	8.6	4.98
-2.0	4.55	9.0	4.5
-2.4	3.29	9.4	4.2
-2.8	2.59	9.8	4.13
-3.2	2.52	10.2	3.6

We can demonstrate explicitly that the NDCME model is sufficient to explain the high-vacuum photoemission data by choosing an average density of states from the results of Figs. 69 and 70 and calculating the energy distributions using

$$n(E_f) = BN_c^{eff}(E_f)N_v(E_f - \hbar\omega) \qquad (36)$$

$n(E_f)$ is the density of electrons photoemitted at an energy E_f above the top of the valence band; $N_c^{eff}(E_f)$ is the effective conduction band density of states at E_f; $N_v(E_f - \hbar\omega)$ is the valence band density of states at $E_f - \hbar\omega$, and B is an undetermined constant.

The effective density of states used to calculate the energy distributions is shown in Fig. 71. The points indicate the scale factors that were used in the density of states analysis. We compare the calculated curves with experimental curves in Fig. 72. The measured curves have been normalized to yield, but the calculated curves are identically the result of using Eq. (36) with the value of B chosen for the best fit. The very good agreement is explicit demonstration that the NDCME model is sufficient to explain most of the photoemission for the high-vacuum-cleaved sample.

Although most of the photoemission for the high-vacuum-cleaved sample is explained by the NDCME model, it remains to be explained why

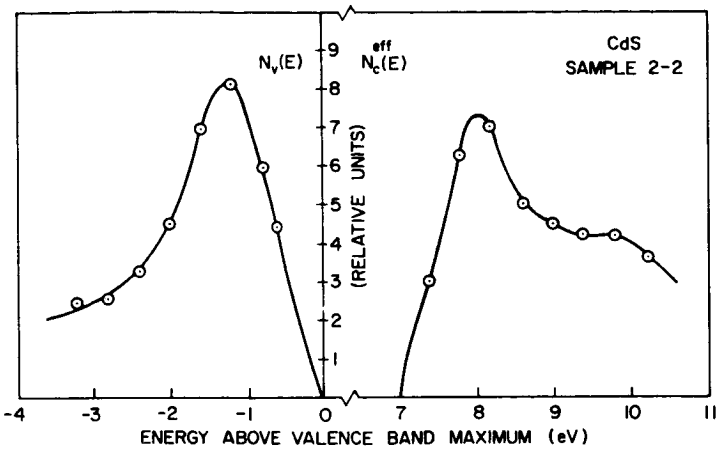

FIG. 71. CdS EFFECTIVE DENSITY OF STATES USED TO CALCULATE ENERGY DISTRIBUTIONS FOR HIGH-VACUUM-CLEAVED SAMPLE. Points indicate the scale factors used in the density of states analysis.

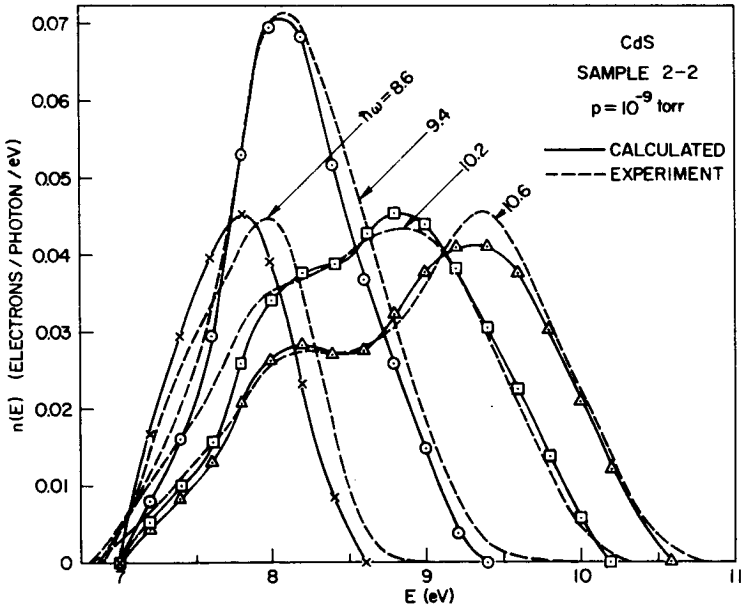

FIG. 72. COMPARISON OF CALCULATED AND MEASURED ENERGY DISTRIBUTIONS. Calculated curves result from Eq. (36) and the effective density of states in Fig. 71.

the conduction band densities of states seen by initial states near $E_i = -0.7$ eV lie above the conduction band densities of states seen by other initial states (Fig. 70). This enhancement cannot be explained by the appearance of secondary electrons in the energy distributions, since an electron must lose at least a band gap energy (2.4 eV) in an

electron-electron scattering event. We conclude that the transitions from initial states near the top of the valence band to final states near 8.1 eV are enhanced by as much as a factor of 2 over the prediction of the NDCME model alone. In other words, up to one-half of these electrons are the result of matrix-element-dependent transitions.

It is interesting to note that these matrix-element-dependent transitions are not very apparent in Fig. 72. The reason is that they actually are not very numerous. Although the enhancement is significant for initial states within about 0.7 eV of the valence band maximum, we see in Fig. 69 that the valence band density of states is quite small in this region.

2. Low-Vacuum Data

We have performed the density of states analysis on the photoemission data for the sample cleaved at a pressure of 10^{-4} torr, and the results are shown in Figs. 73 and 74. In Table 8 we present the scale factors used in this analysis. As mentioned in Sec. B1, the effects of the poorer vacuum are (1) a lowering of the electron affinity by more than one volt, and (2) the appearance of a large number of secondary electrons in the energy distributions. The latter effect has a large influence on the derived valence band density of states below about -2.6 eV. Comparing the valence band density of states for the high-vacuum sample (Fig. 69) and for the low-vacuum sample (Fig. 73), we find that for energies less than about -2.6 eV there is a large apparent valence band density of states for the low-vacuum data that is not seen in the high-vacuum data. This effect is due to the appearance of secondary electrons in the energy distributions. We show in Chapter VII, Sec. A, that there are more secondary electrons produced internally in the low-vacuum-cleaved sample than in the high-vacuum-cleaved sample.

The valence band densities of states seen by final states above 8.0 eV nearly superimpose (Fig. 73). The effective conduction band densities of states above 8.0 eV also nearly superimpose (Fig. 74). Therefore, the NDCME model is sufficient to explain most of the low-vacuum photoemission for final states above 8.0 eV. These results for final

TABLE 8. SCALE FACTORS FOR DENSITY OF STATES ANALYSIS OF LOW-VACUUM PHOTOEMISSION DATA FOR CdS

E_i	$N_v(E_i)$	E_f	$N_c^{eff}(E_f)$
-0.5	2.2	6.5	8.2
-0.7	3.3	6.9	8.15
-0.9	4.2	7.3	7.6
-1.3	5.2	7.7	7.3
-1.7	5.0	8.1	6.8
-2.1	4.35	8.5	5.9
-2.5	4.0	8.9	4.83
-2.9	4.0	9.3	4.14
		9.7	3.66

states above 8.0 eV agree with the results for the high-vacuum cleavage (Sec. C1).

The lower electron affinity for the low-vacuum-cleaved sample allows us to observe strong matrix-element-dependent transitions that are not observed in the high-vacuum-cleaved sample. It is apparent from Figs. 73 and 74 that transitions to final states below 8.0 eV cannot be explained by a NDCME model. The matrix elements that couple initial states near the top of the valence band to final states in the region $5.5 < E_f < 8.0$ eV are much weaker than the matrix elements that couple deeper valence band states to these same final states. Of course, for $-2.1 < E_i < 0$ the differences among the curves of Fig. 74 cannot be due to the appearance of secondary electrons in the energy distributions, since the minimum energy loss through electron-electron scattering is equal to the band gap (2.4 eV).

There is a very striking feature about the low-vacuum photoemission data, but it is not at all apparent in Figs. 73 and 74. The following analysis is intended to bring out this feature. Let us define the function $f(E_f, \hbar\omega)$ by

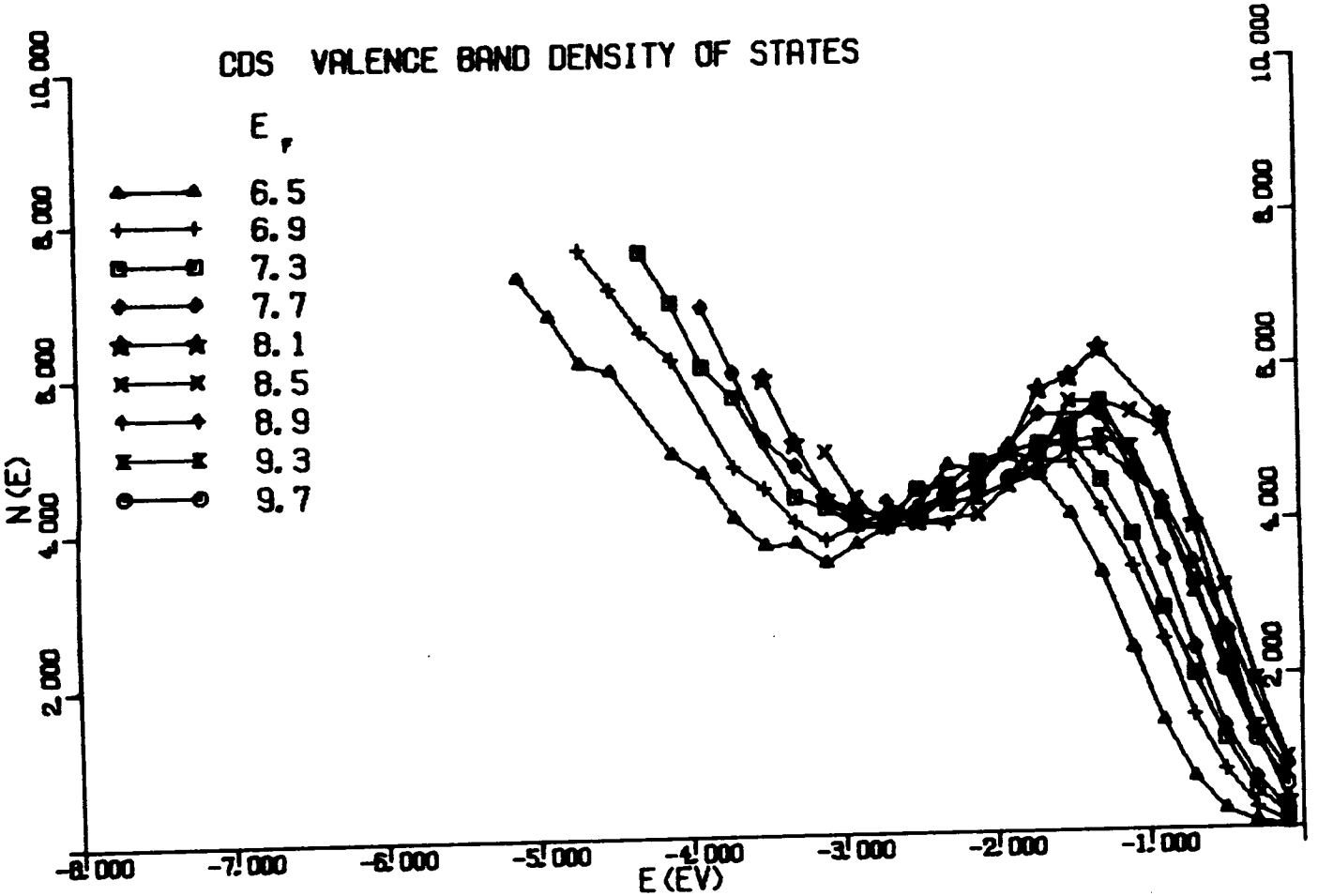

FIG. 73. CdS VALENCE BAND DENSITY OF STATES DETERMINED BY DENSITY OF STATES ANALYSIS OF LOW-VACUUM PHOTOEMISSION DATA. E_f is the energy of the conduction band state used to derive the valence band density of states.

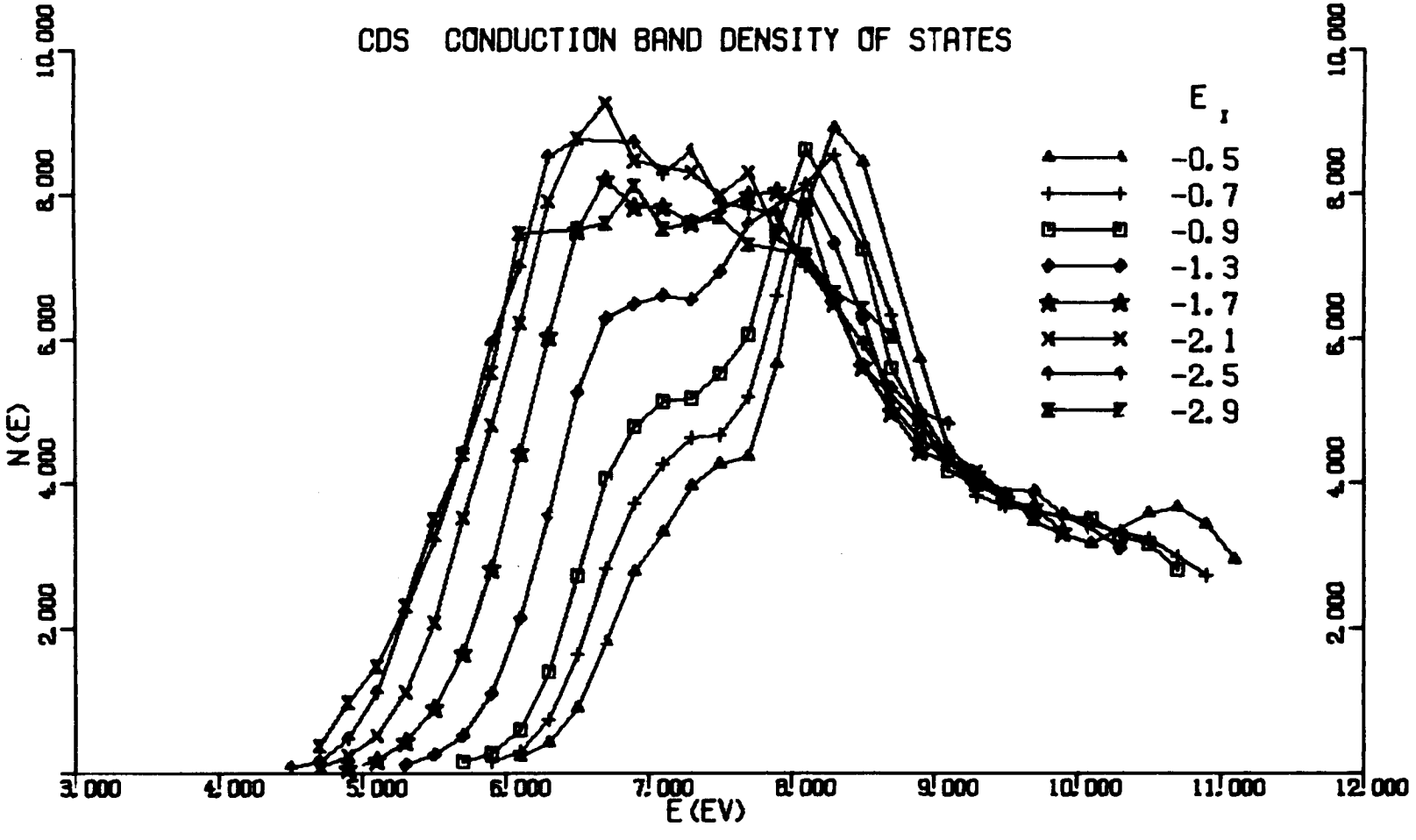

FIG. 74. CdS EFFECTIVE CONDUCTION BAND DENSITY OF STATES DETERMINED BY DENSITY OF STATES ANALYSIS OF LOW-VACUUM PHOTOEMISSION DATA. E_i is the energy of the initial state used to derive the effective conduction band density of states.

$$n(E_f) = N_c^{eff}(E_f)N_v(E_f - \hbar\omega)f(E_f,\hbar\omega) \qquad (37)$$

For a photon energy $\hbar\omega$, the density of photoemitted electrons at energy E_f is not given by $N_c^{eff}(E_f)N_v(E_f - \hbar\omega)$, but rather this product of densities of states must be multiplied by $f(E_f,\hbar\omega)$, the strength of coupling between initial and final states. If the NDCME model were sufficient to explain the photoemission, then $f(E_f,\hbar\omega)$ would be equal to a constant for all E_f and $\hbar\omega$. When the density of states model is not sufficient, then in general, the function f for one final energy will not be simply related to the function f for another final energy.

Obviously, there is a considerable amount of arbitrariness in the choice of N_c^{eff}, N_v, and f. For any arbitrary N_c^{eff} and N_v, a set of f's can be constructed, such that Eq. (37) reproduces the photoemission data. The feature we wish to point out is that, for one particular choice of N_c^{eff} and N_v, f has a very simple form. Using the effective density of states shown in Fig. 75, we derive the strength of coupling shown in Fig. 76 by plotting the quantity

$$f(E_f,\hbar\omega) = \frac{n(E_f)}{N_c^{eff}(E_f)N_v(E_f - \hbar\omega)} \qquad (38)$$

for various final energies E_f. We only use photoemission data for $E_i > -2.4$ eV; hence there are no contributions to Fig. 76 due to secondary electrons. The striking feature about Fig. 76 is that for final energies below about 8.1 eV, the strength of coupling is a function of $\hbar\omega$ only and rises by a factor of 20 between $\hbar\omega = 6.8$ eV and 8.5 eV. This factor of 20 is more than an order of magnitude larger than either the uncertainty in the yield measurement or any correction to the density of states analysis due to optical data (see introductory remarks in this section). Rather, states near the top of the valence band are very weakly coupled to final states between 5.5 and 8.0 eV. It can also be seen in Fig. 76 that transitions to final states near 8.5 eV are enhanced above the predictions of a NDCME model alone.

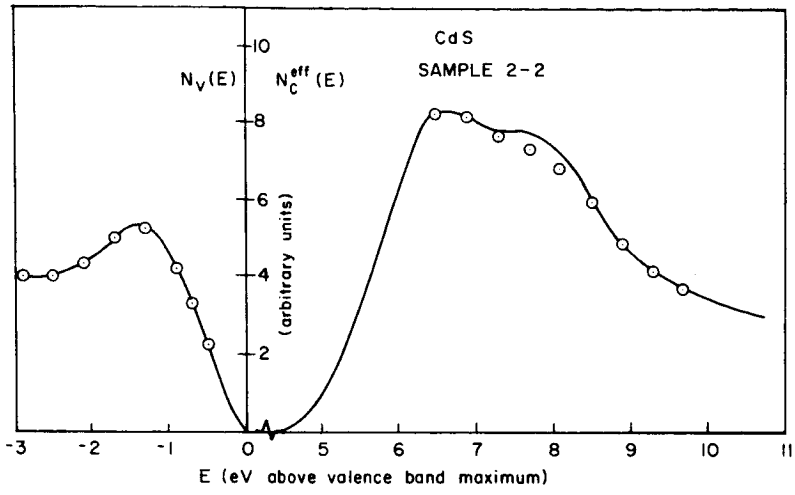

FIG. 75. CdS EFFECTIVE DENSITY OF STATES USED IN EQ. (38) TO DERIVE THE STRENGTH OF COUPLING FOR LOW-VACUUM-CLEAVED SAMPLE. Points indicate the scale factors used in the density of states analysis.

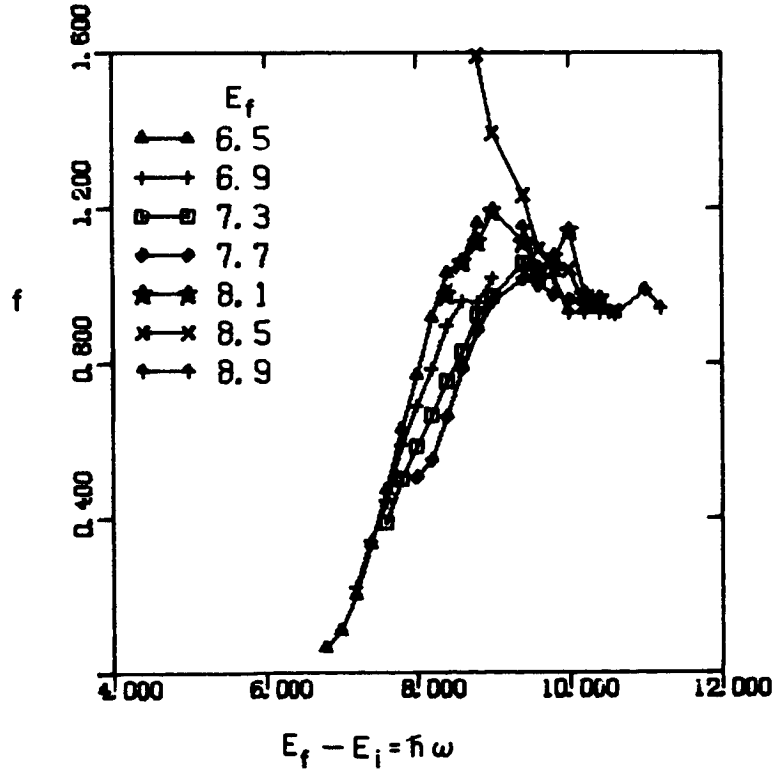

FIG. 76. STRENGTH OF COUPLING BETWEEN INITIAL AND FINAL STATES. E_f is the energy of the final state used in Eq. (38).

D. DISCUSSION OF BAND STRUCTURE AND OPTICAL PROPERTIES

In this section we discuss the electronic band structure and optical properties of CdS using features of the electronic structure determined from the photoemission data. A complete understanding of the electronic properties of CdS is hampered by the lack of a detailed band structure calculation.

These matrix-element-dependent transitions observed in the photoemission data have a large influence on the optical properties of CdS. We present in Fig. 77 the reflectivity of CdS (CARDONA and HARBEKE, 1965). We have presented in Fig. 68 the quantities $\epsilon_2\omega^2$ and $n\omega$ which we have derived from the data of CARDONA and HARBEKE. The peaks at 8.2 eV in the reflectivity (E_2) in Fig. 77 and at 7.8 eV in $\epsilon_2\omega^2$ (Fig. 68) are due to the factor of 20 increase in the strength of coupling to final states below 8.0 eV for $6.8 < \hbar\omega < 8.5$ eV (Fig. 76).

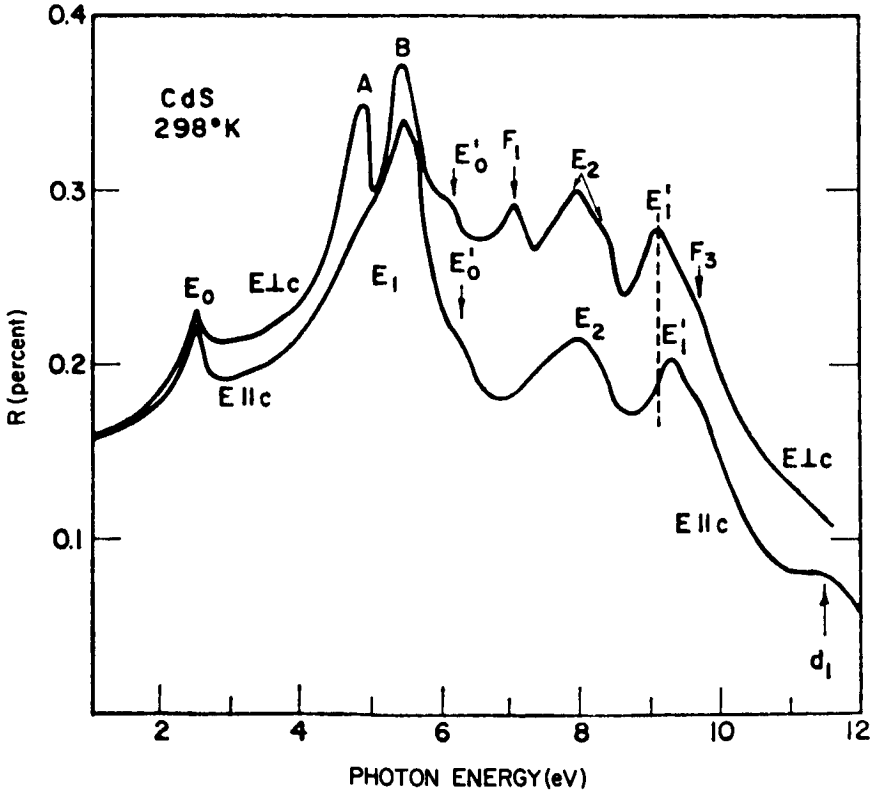

FIG. 77. REFLECTIVITY OF CdS (CARDONA AND HARBEKE, 1965).

NDCME transitions also influence the optical properties of CdS. For photon energies near 9.4 eV, there are NDCME transitions from a peak at -1.3 eV in the valence band density of states to a peak in the conduction band density of states at 8.1 eV (Figs. 60 and 65). The corresponding features of the optical data are a peak in the reflectivity at 9.3 eV (E_1' in Fig. 77) and a peak in $\epsilon_2\omega^2$ at 9.0 eV (Fig. 68). It is clear from the density of states analysis (Sec. C) that the "background" of the optical data for photon energies near 9.4 eV is due to NDCME transitions. However, the peaks in the optical data near 9.4 eV are probably due to the matrix-element enhancement observed in the density of states analysis (Figs. 70 and 74) for transitions to final states near 8.1 eV.

KS found that the gross features of the optical conductivity σ could be predicted by the NDCME model using a density of states derived from photoemission data. However, in order to obtain peaks as sharp as those in the measured optical conductivity (WALKER and OSANTOWSKI, 1964), KS found it necessary to use a much sharper density of states. Energy distributions calculated using the sharpened density of states were much sharper than the measured energy distributions. We suggest that the "background" of σ is due to NDCME transitions (as found by KS) but that the peaks actually are due to matrix-element-dependent transitions.

When it first appears, the shoulder S in the energy distributions for $\hbar\omega > 10.6$ eV (Fig. 67) is due to transitions to final states near 10.6 eV. Although the photoemission data are not definitive, it is likely that S is due to direct transitions to final states near 10.6 eV (see Sec. B2). The corresponding feature of the reflectivity is a peak at 11.4 eV (d_1 in Fig. 77) which PHILLIPS (1964) assigned in zinc blende materials to $L_3^v - L_1$ transitions. The corresponding transition in wurtzite materials is $\Gamma_6^v - \Gamma_3$. If this interpretation is correct, the photoemission data locate Γ_3 at about 10.6 eV above the top of the valence band.

The curves of Fig. 69 for $-3 < E < 0$ are probably quite close to the actual valence band density of states. The rise for $E < -3.5$ eV is most likely due to the appearance of secondary electrons in the energy distributions. It is more difficult to estimate the conduction band density of states. Even in the simplest case, the effective conduction

band density of states is the product of the actual conduction band density of states, a threshold function, and an escape depth (see Chapter II, Sec. D1). The last two quantities are unknown functions of electron energy. Nonetheless, special features of the effective density of states (peaks, dips, etc.) can usually be attributed to the actual conduction band density of states. Since the electron affinity is much lower for the low-vacuum-cleaved sample, the best estimate of the conduction band density of states is obtained from Fig. 74.

E. CONCLUSIONS

A principal conclusion of this study of CdS is that the photoemission and optical properties of CdS are due to a mixture of NDCME transitions and matrix-element-dependent transitions. None of these matrix-element-dependent transitions have been positively identified as direct transitions. The peaks in reflectivity (E_2) and $\epsilon_2\omega^2$ for photon energies near 8.0 eV are due to the factor of 20 rise in the strength of coupling to conduction band states below 8.0 eV for $6.8 < \hbar\omega < 8.5$ eV. Yet the peaks in reflectivity (E_1') and $\epsilon_2\omega^2$ near 9.4 eV are to a large extent due to NDCME transitions from a peak at -1.3 eV in the valence band density of states to a peak at 8.1 eV in the conduction band density of states. The features of the optical properties are therefore determined by both NDCME transitions and matrix-element-dependent transitions.

Most of the photoemission from the high-vacuum-cleaved sample is successfully explained by the NDCME model. Using the density of states analysis we determined the valence band density of states and the effective conduction band density of states. For the high-vacuum data the success of the NDCME model was explicitly demonstrated by comparing experimental data and energy distributions calculated from the derived density of states.

The lower electron affinity of the low-vacuum-cleaved sample allows us to observe strong matrix-element-dependent transitions to final states below 8.1 eV. The strength of coupling to these final states rises by a factor of 20 in the region $6.8 < \hbar\omega < 8.5$ eV. States near the top of the valence band are very weakly coupled to final states near 6.6 eV.

For both high- and low-vacuum data, we observed that states near the

top of the valence band are strongly coupled to conduction band states near 8.1 eV. In the density of states analyses we find that these transitions are enhanced by as much as a factor of 2 over the predictions of the NDCME model. However, since the valence band density of states is weak near the top of the valence band, there is a relatively small number of these transitions.

The shoulder S that appears in the energy distributions for $\hbar\omega > 10.6$ eV corresponds to the d_1 reflectivity peak at 11.4 eV. This structure has been tentatively assigned to transitions to conduction band states near Γ_3. If this assignment is correct, the photoemission data locate Γ_3 at 10.6 eV.

The photoemission data have located a valence band at -9.2 eV. It has been suggested that these valence band states are derived from cadmium 4d states.

Lastly, we have attempted to determine whether or not the lower electron affinity for the low-vacuum-cleaved sample is due to the gaseous hydrogen in the monochromator. A high-vacuum-cleaved sample of CdS was exposed to a 5-micron pressure of ultrapure Linde hydrogen in the high-vacuum chamber. The yield and energy distributions measured while the sample was exposed to the hydrogen were indistinguishable from the measurements before the high-vacuum cleavage was exposed to the hydrogen. Therefore, the lower electron affinity is not due to the hydrogen in the monochromator.

VII. SPECIAL TOPICS

A. EFFECTS OF ELECTRON-ELECTRON SCATTERING

Effects due to electron-electron scattering are observed in the photoemission data. The qualitative features of the scattering are similar in CdTe, CdSe, and CdS. To illustrate, we discuss the scattering observed in the CdSe photoemission data, and show that more secondary electrons are produced internally in the low-vacuum-cleaved sample than in the high-vacuum-cleaved sample. We suggest a possible explanation for this difference.

In Figs. 78 and 79 we compare energy distributions for the high- and low-vacuum-cleaved samples. These data used the same standard for measuring quantum yield so that we may have confidence in the relative heights of two curves at the same photon energy. Consider first the energy distributions in Fig. 78 for a photon energy of 8.0 eV. None of the electrons emitted at 7.3 eV have been electron-electron scattered, since the band gap is 1.8 eV. Since the heights of the two distributions are about equal at 7.3 eV, the fraction of electrons which are excited to 7.3 eV

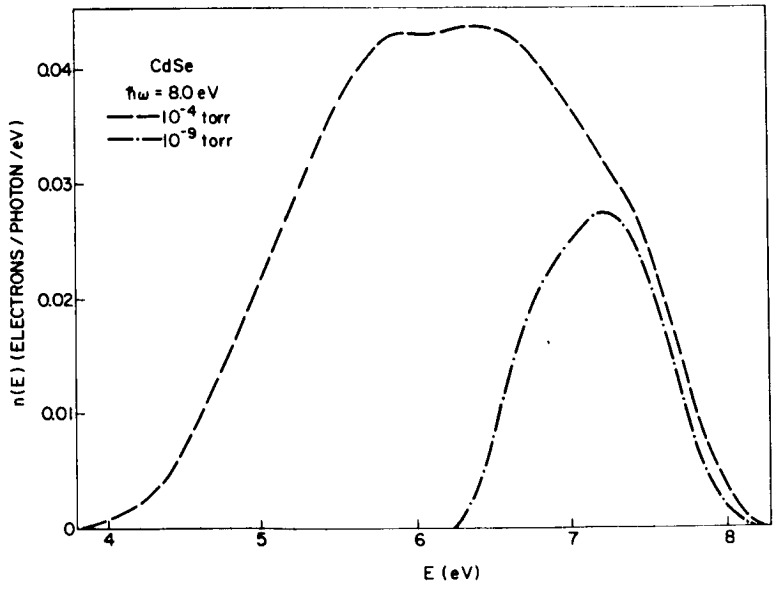

FIG. 78. COMPARISON OF CdSe ENERGY DISTRIBUTIONS FROM HIGH-VACUUM- AND LOW-VACUUM-CLEAVED SAMPLES FOR $\hbar\omega$ = 8.0 eV.

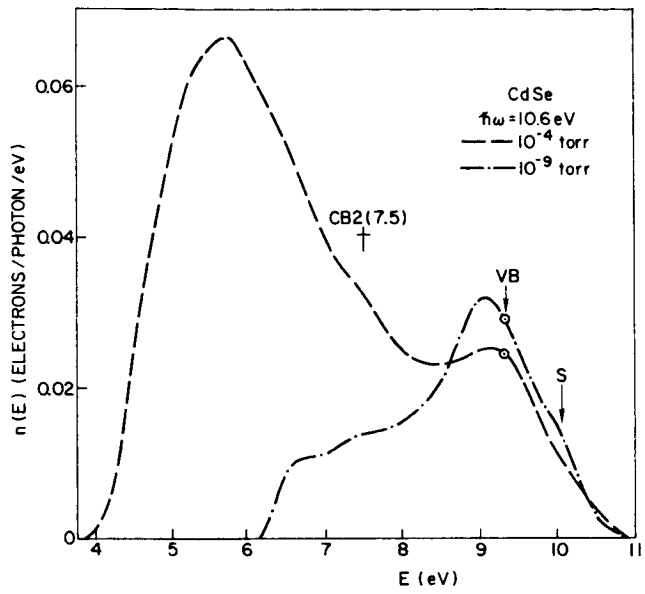

FIG. 79. COMPARISON OF CdSe ENERGY DISTRIBUTIONS FROM HIGH-VACUUM- AND LOW-VACUUM-CLEAVED SAMPLES FOR $\hbar\omega$ = 10.6 eV.

and subsequently escape the crystal is the same for the high- and low-vacuum-cleaved samples. If the threshold function at 7.3 eV is smaller for the high-vacuum cleavage (due to the larger electron affinity), then the loss of 7.3 eV electrons due to electron-electron scattering is more severe for the low-vacuum cleavage.

Consider now the energy distributions in Fig. 79 for a photon energy of 10.6 eV. Secondary electrons may now appear at 7.3 eV since the band gap is only 1.8 eV. For $\hbar\omega$ = 10.6 eV, the number of electrons emitted at 7.3 eV for the low-vacuum-cleaved sample is 2-1/2 times the number emitted for the high-vacuum-cleaved sample. Since we have already shown that the same fraction of 7.3 eV electrons escape for both experiments, the extra 150 percent are additional secondary electrons. Hence more secondary electrons are produced internally in the low-vacuum-cleaved sample than in the high-vacuum-cleaved sample.

It is reasonable that the electron-electron scattering probability should be greater for the low-vacuum-cleaved sample. Contamination near the surface almost certainly perturbs the crystal potential seen by an electron near the surface. One of the effects of this perturbation is

to cause elastic scattering. For a fixed electron-electron mean free path, an increase in elastic scattering causes an increase in electron-electron scattering probability (STUART et al, 1963). The integrated path length to the surface (and hence the scattering probability) is larger due to the inelastic scattering.

In summary, the data indicate that there are more secondary electrons generated internally in the low-vacuum-cleaved sample than in the high-vacuum-cleaved sample. We suggest that this increase is due to a larger electron-electron scattering probability for electrons in the low-vacuum-cleaved sample and that this increase in electron-electron scattering probability is due to the elastic scattering induced by surface contamination.

B. ESTIMATE OF ESCAPE DEPTH

A knowledge of the absolute yield and the absorption coefficient allows us to estimate the escape depth for the high-vacuum-cleaved sample. It is apparent from Figs. 48 and 49 that, for $\hbar\omega > 10$ eV, most of the absorption is to final states well above the vacuum level. It follows that, regardless of the excitation process, the yield is approximately

$$Y \approx \frac{0.5\alpha LT}{1 + \alpha L} \tag{39}$$

This form will suffice here, even though SPICER (1961) has given an exact expression for the appropriate average over the escape depths of the photoexcited electrons. T is the surface transmission probability: of the electrons reaching the surface, a fraction T escapes into the vacuum. $\alpha L/(1 + \alpha L)$ is the fraction of the photoexcited electrons that are not electron-electron scattered on their way to the surface (Chapter II, Sec. D). The factor of 0.5 arises since half of the photoexcited electrons are heading in initial directions away from the semiconductor surface. Equation (39) assumes that electron-electron-scattered electrons are unable to escape the crystal. It also assumes that the mean free path for elastic scattering is longer than the escape depth.

For $\hbar\omega = 10.2$ eV, the absolute yield is 0.071 for the high-vacuum-cleaved sample of CdSe (Fig. 37). If we assume that $T = 0.5$, then

$\alpha L = 0.396$. For $\hbar\omega = 10$ eV, CARDONA and HARBEKE (1965) found an absorption coefficient $\alpha = 6.2 \times 10^5$ cm^{-1}. Using this value for α, we find that the escape depth is 64 Å for an electron about 8.5 eV above the top of the valence band. If our experimental yield is too large by a factor of 2 at 10 eV (Chapter II), then $L = 27$ Å, if we again assume $T = 0.5$. Finally, if the yield is high by a factor of 2 but $T = 0.25$, then the escape depth is 64 Å. Therefore, for the three cases, the CdSe escape depths are 64, 27, and 64 Å.

For CdS at $\hbar\omega = 10.2$ eV, the absorption coefficient is 7.73×10^5 cm^{-1} (CARDONA and HARBEKE, 1965), and the absolute yield of the high-vacuum-cleaved sample is 0.92 (Fig. 57). The CdS escape depths for the three cases considered above for CdSe are 75, 29, and 75 Å.

For CdTe at $\hbar\omega = 10.2$ eV, the absorption coefficient is 9.5×10^5 cm^{-1} (CARDONA, 1965), and the absolute yield of the high-vacuum-cleaved sample is 0.033 (Fig. 17). The CdTe escape depths for the three cases considered above for CdSe are 16, 8, and 16 Å.

In Table 9 we compare the estimated escape depths $L(E)$ for CdTe, CdSe, and CdS for electrons about 8.5 eV above the top of the valence band. We also list the absorption coefficients, yields, and band gaps. Note that the escape depth decreases in the sequence CdS, CdSe, CdTe, and that this is correlated with a decrease in yield and band gap.

TABLE 9. PROPERTIES OF CdTe, CdSe, AND CdS FOR $\hbar\omega = 10.2$ eV

Crystal	L (Å)	Band Gap (eV)	YIELD (%)	α (10^5cm^{-1})
CdTe	16	1.6	3.3	9.5
CdSe	64	1.8	7.1	6.2
CdS	75	2.4	9.2	7.7

C. LOCATION OF d-BAND

We find that the location of the d-band, as determined from photoemission data, is consistent with both the ionic and covalent models for these solids. Hence we are unable to determine the degree of ionicity of

these materials. The d-band is separated 8.6, 8.6, and 7.9 eV from the other valence bands in CdTe, CdSe, and CdS. We lack sufficient atomic data for Te to discuss in detail our result for CdTe. On the ionic model, the smaller separation in CdS relative to CdSe is due to the larger Madelung shift in CdS. On the covalent model, the separation for CdS is less than for CdSe since the 3s-3p separation in atomic S is less than the 4s-4p separation in atomic Se.

1. Ionic Model

The ionic model for the II-VI compounds assumes that two electrons are transferred from the column II atom to the column VI atom. The energy of this system is calculated by first transferring the electrons with the atoms at an infinite separation; the ions are then brought together to form a lattice. The energy of the system of ions at infinite separation is larger than the energy of the atoms; hence the system of ions at infinite separation is unstable against decay into the atoms. However, when the ions are brought together to form a lattice, the decrease in energy due to the electrostatic potential (Madelung potential) is sufficient to make the system stable against decay into the atoms. The Madelung potential increases the energies of electrons on the column II atom and decreases the energies of electrons on the column VI atom. Further details can be found in SEITZ (1940, p. 447ff).

The effects of the Madelung shift for CdSe are shown in Fig. 80. The total electron affinity of $Se^{=}$ is -4.2 eV (SEITZ, 1940, p. 83). The electron affinities of Se^{-} and S^{-} are probably about 1.0 eV (SEITZ, 1940, p. 449). The energy required to remove an electron from $Se^{=}$ at infinity is therefore -5.2 eV. The ionization energy of the 5s level of atomic Cd^{+} is 16.9 eV (MOORE, 1949). Hence the energy required to remove an electron from $Se^{=}$ and place it on Cd^{++} to form Cd^{+} is -22.1 eV. The Cd^{++} 5s levels thus lie 22.1 eV below the $Se^{=}$ 4s levels in Fig. 80. Since the ionization energy of the 4d level of Cd^{++} is 37.5 eV (MOORE, 1949), the energy required to ionize a Cd^{++} ion and place the electron on another Cd^{++} ion is 20.6 eV. Hence the Cd^{++} 4d levels lie 20.6 eV below the Cd^{++} 5s levels in Fig. 80.

The Madelung energy is given by SEITZ (1940, p. 77):

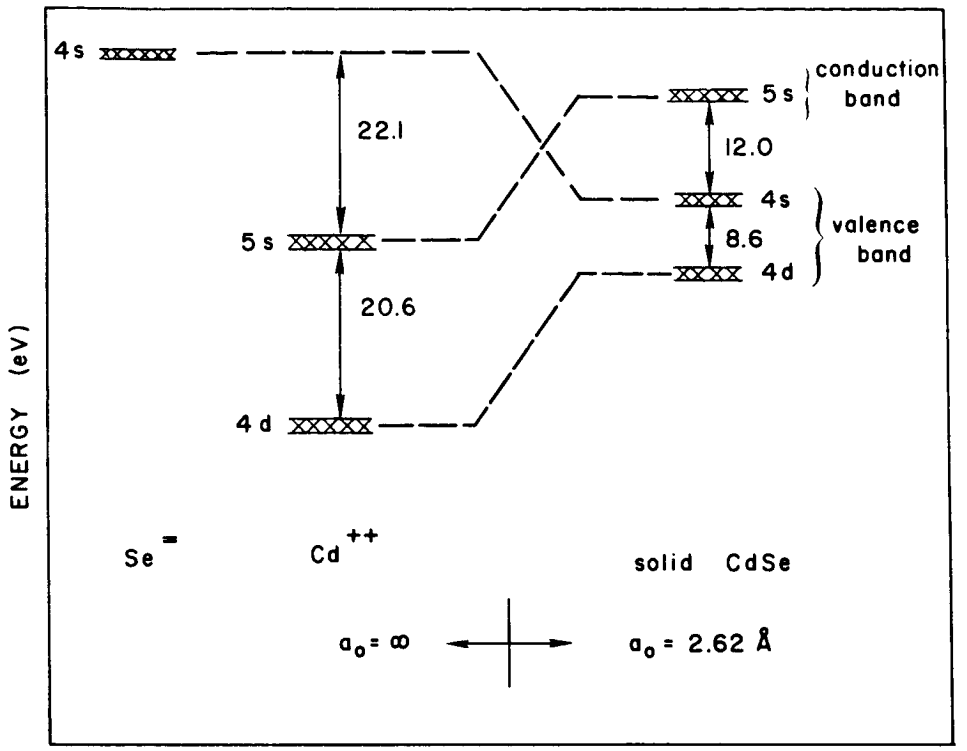

FIG. 80. THE IONIC ENERGY-LEVEL RELATIONS FOR CdSe. The behavior of these levels when a lattice is formed is shown by the dotted lines. The cation-anion separation is a_o.

$$V = -\frac{Mq^2}{a_o} \text{ rydberg per molecule} \qquad (40)$$

M is the Madelung constant (1.641 for wurtzite); q is the number of electrons transferred per molecule; and a_o is the equilibrium cation-anion distance. For CdSe, $a_o = 2.62$ Å. Assuming that $q = 2$, we find $V = 34.1$ eV/molecule, or 17.05 eV/atom. This raises Cd^{++} levels by 17.05 eV and lowers $Se^{=}$ levels by the same amount. Hence, in solid CdSe, the $Se^{=}$ 4s levels lie 8.6 eV above the Cd^{++} 4d levels. This is exactly the value determined by the photoemission experiment. Unfortunately, the ionic model predicts a band gap of about 12 eV, whereas the measured band gap is 1.8 eV.

The total electron affinity of $S^{=}$ is -3.4 eV (SEITZ, 1940, p. 83) and the electron affinity of S^{-} is 1.0 eV. The equilibrium cation-anion

distance for CdS is 2.52 Å; hence the Madelung shift is 17.7 eV/atom. The d levels in CdS therefore lie 6.5 eV below the s levels. The ionic model predicts that the separation in CdS is less than in CdSe; this is experimentally observed. However, the predicted difference (2.1 eV) is three times larger than is experimentally observed.

Since the lattice constant for CdTe is 2.79 Å and M = 1.638, the Madelung shift is 16 eV/atom. For the d-s separation to be the same as in CdSe, the energy required to remove an electron from $Te^{=}$ would have to be 7.3 eV. This value is unreasonably large since the corresponding values for CdSe and CdS were 5.2 and 4.4 eV.

2. Covalent Model

The covalent model takes the point of view that bringing cadmium and selenium atoms together causes mixing of nearly degenerate levels on the two atoms. This situation is shown for CdSe in Fig. 81. The atomic data are taken from MOORE (1949). The Cd 5s levels mix with the Se 4p levels to form a valence band, and the Cd 4d levels mix with the Se 4s levels to form a deeper valence band about 11 eV below the former.

The sulfur 3p levels lie 0.8 eV below the selenium 4p levels; hence the center of gravity of the Cd 5s and S (or Se) p levels lies 0.6 eV lower for CdS than for CdSe. The S 3s and Se 4s levels lie at the same energy. Consequently, the covalent model predicts that the separation of the two valence bands is 0.6 eV smaller for CdS than for CdSe. The experimental value is 0.7 eV. Note that this model provides a more realistic location for the conduction band levels.

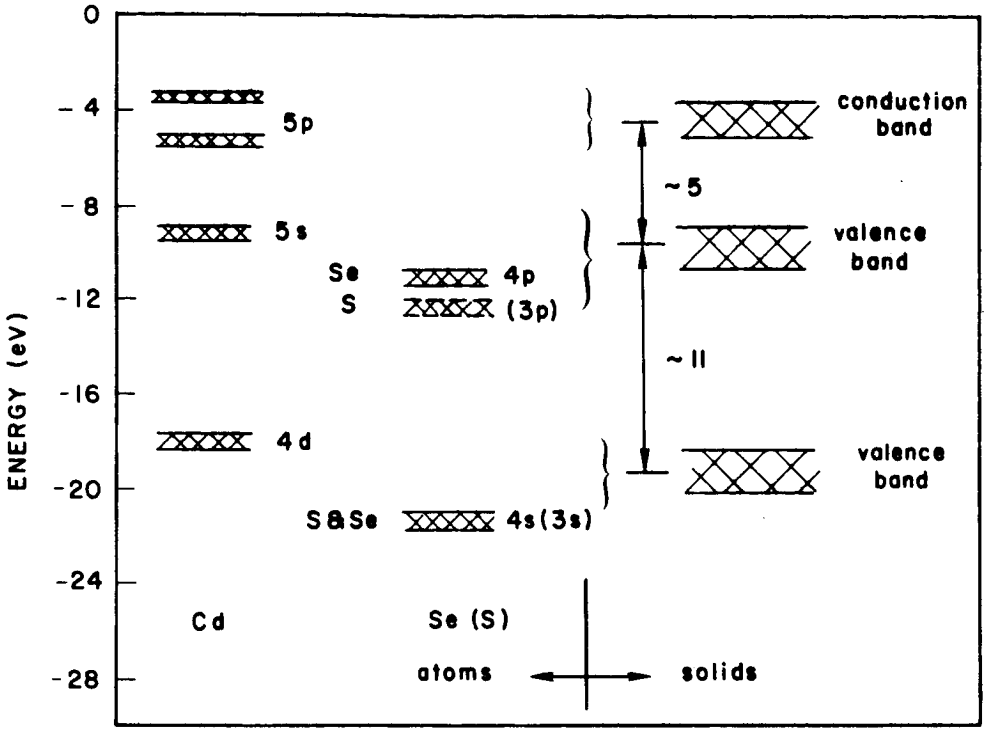

FIG. 81. COVALENT POINT OF VIEW OF FORMING A SOLID FROM THE INDIVIDUAL ATOMS.

VIII. CONCLUSIONS

Matrix elements are important in determining the photoemission from CdTe, CdSe, and CdS. The features of the photoemission from CdSe and CdS are very similar; however, the features of the photoemission from CdTe are quite different from those of CdSe and CdS. The sharp features of the CdTe photoemission data are due to direct transitions. These direct transitions have been assigned to specific regions of the Brillouin zone. In Table 2 of Chapter IV we have compared our results with a pseudopotential band structure (COHEN and BERGSTRESSER, 1966) and with CARDONA and GREENAWAY's (1963) interpretation of their reflectivity data. The agreement is good in some places and poor in others. On the basis of the photoemission data, we have reassigned several of the reflectivity peaks and presented detailed justification for our assignments.

Although there are sharp matrix-element variations in CdSe and CdS, few of these have been positively identified as being due to direct transitions. Using the density of states analysis, we have clearly separated the matrix-element-dependent transitions from those due only to the density of states. In fact, we showed explicitly that most of the high-vacuum CdSe and CdS photoemission data are due to nondirect constant-matrix-element transitions and we have derived the matrix element variation required to explain the low-vacuum CdSe and CdS data. This variation is more than an order of magnitude larger than any of the uncertainties in the calculation.

The qualitative features of the electron-electron scattering are similar in CdTe, CdSe, and CdS. Many more secondary electrons are produced internally in the low-vacuum-cleaved samples than in the high-vacuum-cleaved samples. We suggest that this increase in electron electron scattering is induced by the increased elastic scattering due to surface contamination. The elastic scattering increases the integrated path length to the surface, hence the probability of reaching the surface without pair production is reduced.

The escape depth in the high-vacuum-cleaved samples increases in the sequence CdTe, CdSe, and CdS. The electron-electron scattering is

strongest in CdTe and weakest in CdS. Hence the yield is largest in CdS and smallest in CdTe.

The d-band of cadmium has been located at about 8 eV below the other valence band states in CdTe, CdSe, and CdS. We showed that the slight changes in the location of the d-band in the sequence CdTe, CdSe, and CdS are consistent with both the ionic and the covalent models for the II-VI compounds. Hence we are unable to determine the degree of ionicity of these materials.

APPENDIX A

The purpose of this appendix is to provide additional energy distributions to supplement the data presented in earlier chapters. When combined with the data in Chapters IV (CdTe), V (CdSe), and VI (CdS), energy distributions are presented at intervals of usually 0.2 eV in photon energy for photon energies above the threshold for photoemission.

Figures 82 through 102 illustrate these energy distributions.

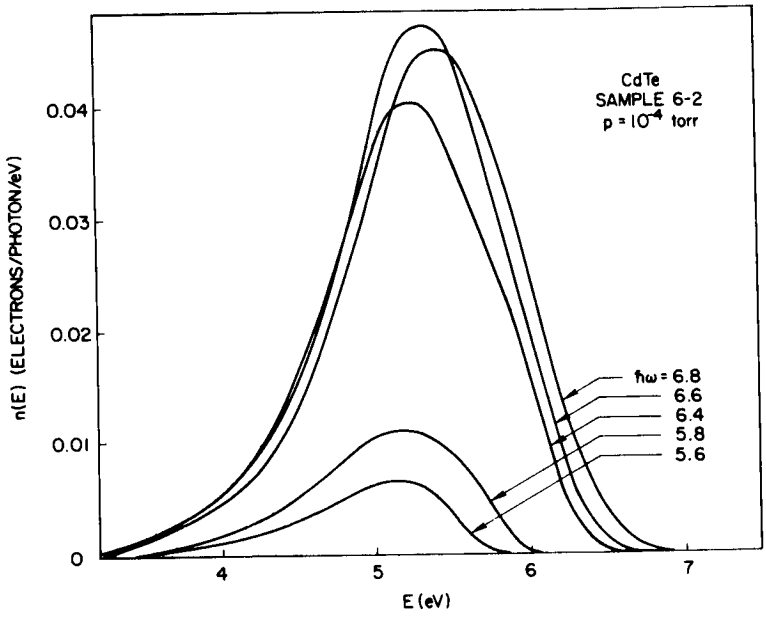

FIG. 82. NORMALIZED ENERGY DISTRIBUTIONS OF THE PHOTOEMITTED ELECTRONS FROM CdTe FOR $5.6 \leq \hbar\omega \leq 6.8$ eV. Electron energy is measured relative to the valence band maximum.

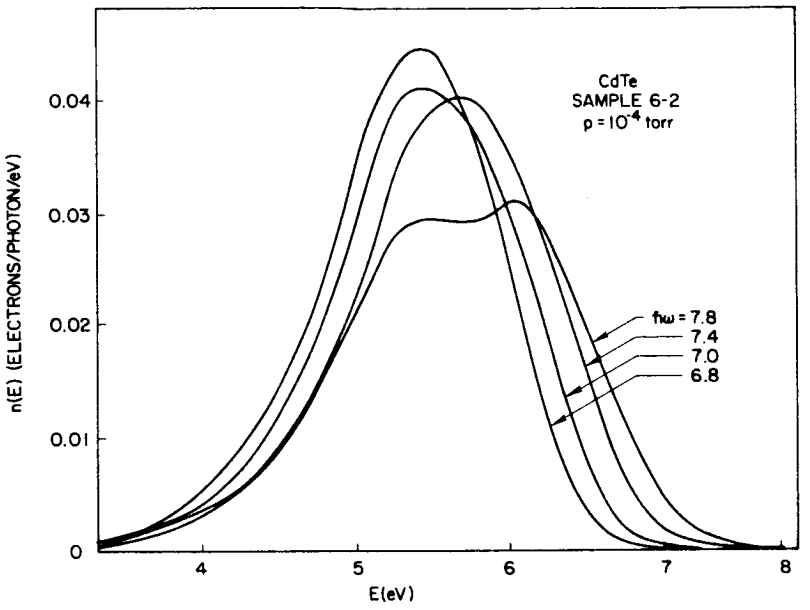

FIG. 83. NORMALIZED ENERGY DISTRIBUTIONS OF THE PHOTO-EMITTED ELECTRONS FROM CdTe FOR $6.8 \leq \hbar\omega \leq 7.8$ eV. Electron energy is measured relative to the valence band maximum.

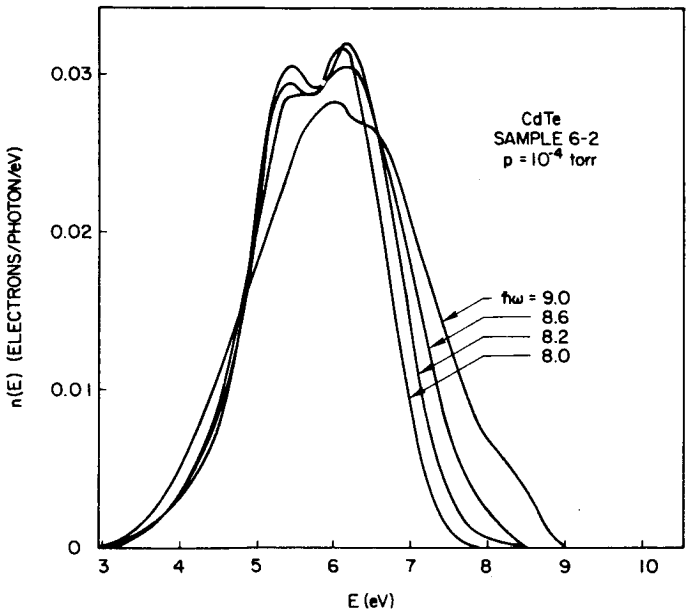

FIG. 84. NORMALIZED ENERGY DISTRIBUTIONS OF THE PHOTO-EMITTED ELECTRONS FROM CdTe FOR $8.0 \leq \hbar\omega \leq 9.0$ eV. Electron energy is measured relative to the valence band maximum.

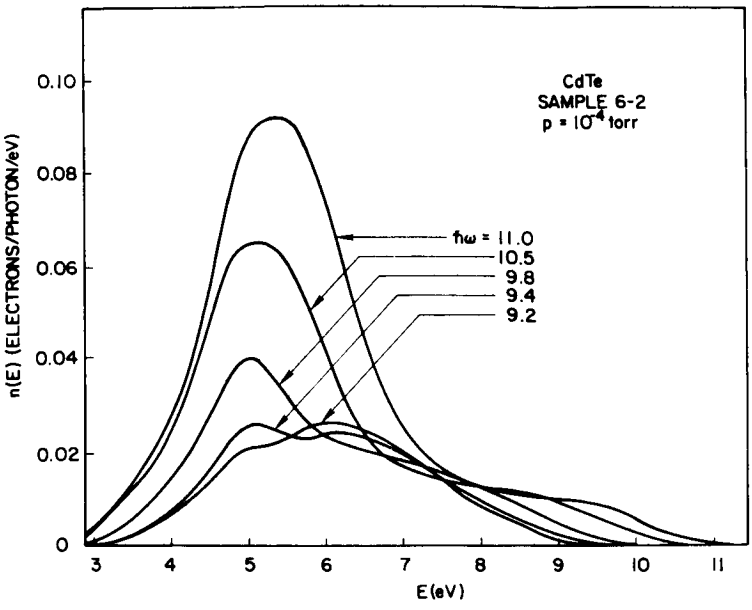

FIG. 85. NORMALIZED ENERGY DISTRIBUTIONS OF THE PHOTO-EMITTED ELECTRONS FROM CdTe FOR $9.2 \leq \hbar\omega \leq 11.0$ eV. Electron energy is measured relative to the valence band maximum.

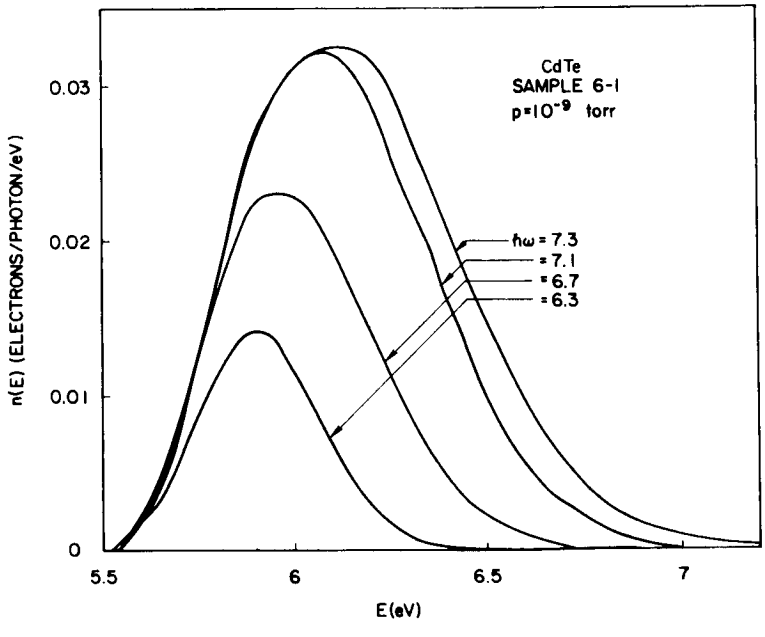

FIG. 86. NORMALIZED ENERGY DISTRIBUTIONS OF THE PHOTO-EMITTED ELECTRONS FROM CdTe FOR $6.3 \leq \hbar\omega \leq 7.3$ eV. Electron energy is measured relative to the valence band maximum.

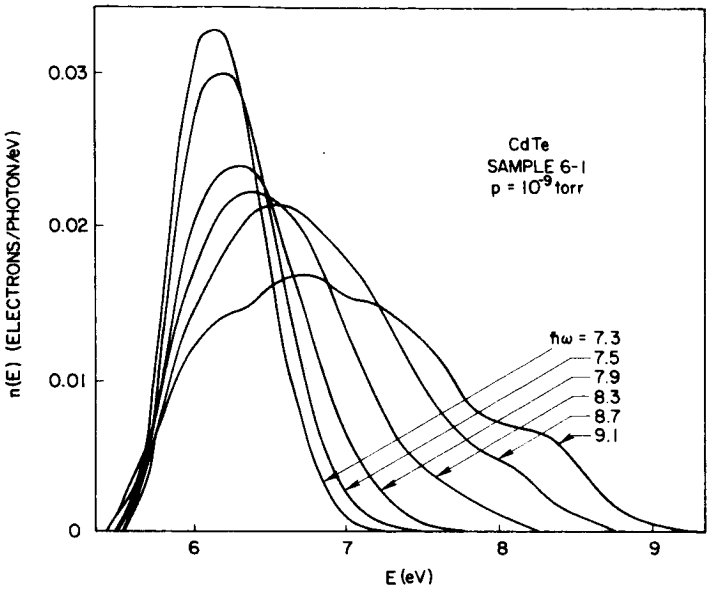

FIG. 87. NORMALIZED ENERGY DISTRIBUTIONS OF THE PHOTO-EMITTED ELECTRONS FROM CdTe FOR $7.3 \leq \hbar\omega \leq 9.1$ eV. Electron energy is measured relative to the valence band maximum.

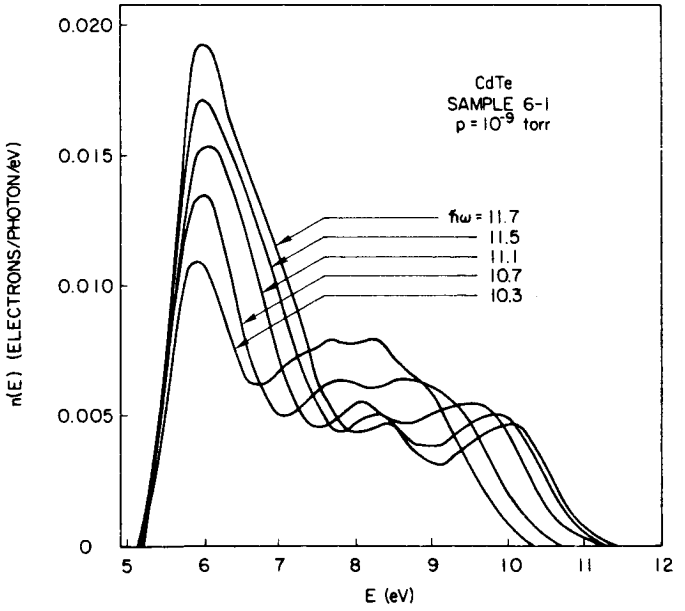

FIG. 88. NORMALIZED ENERGY DISTRIBUTIONS OF THE PHOTO-EMITTED ELECTRONS FROM CdTe FOR $10.3 \leq \hbar\omega \leq 11.7$ eV. Electron energy is measured relative to the valence band maximum.

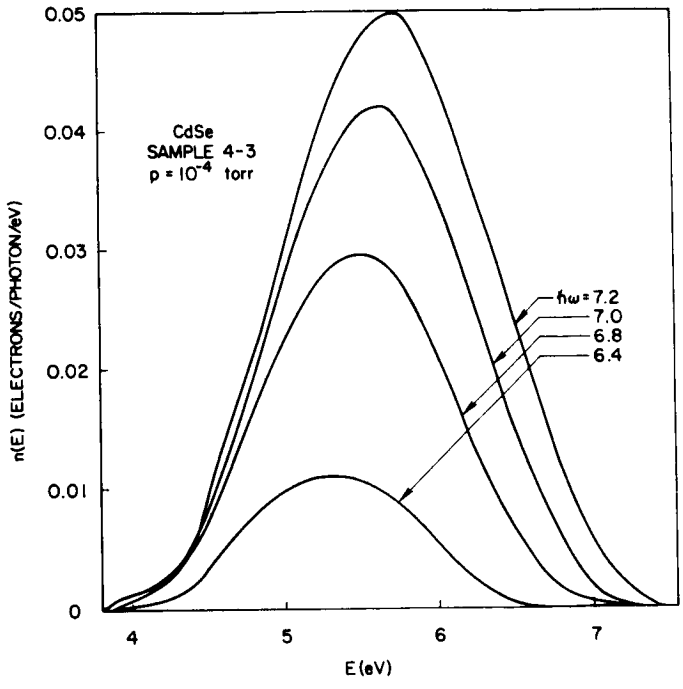

FIG. 89. NORMALIZED ENERGY DISTRIBUTIONS OF THE PHOTOEMITTED ELECTRONS FROM CdSe FOR $6.4 \leq \hbar\omega \leq 7.2$ eV. Electron energy is measured relative to the valence band maximum.

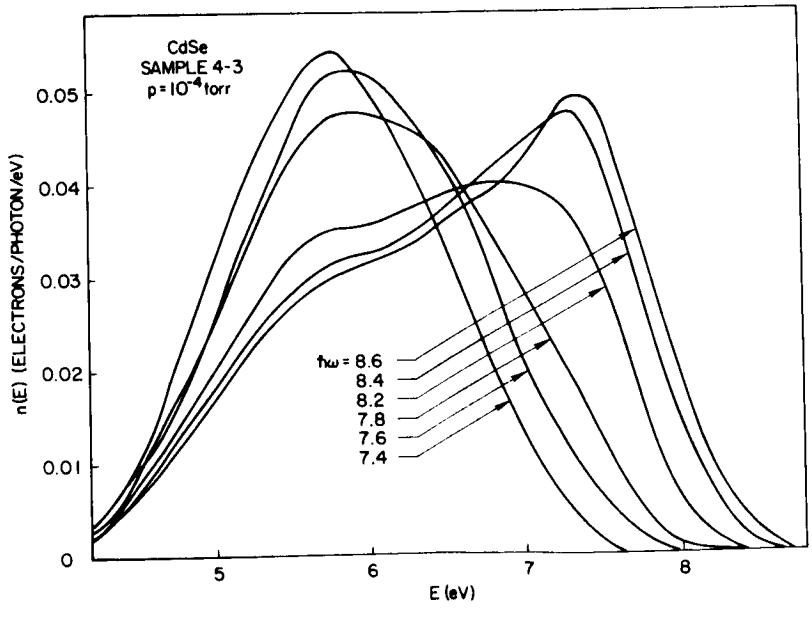

FIG. 90. NORMALIZED ENERGY DISTRIBUTIONS OF THE PHOTOEMITTED ELECTRONS FROM CdSe FOR $7.4 \leq \hbar\omega \leq 8.6$ eV. Electron energy is measured relative to the valence band maximum.

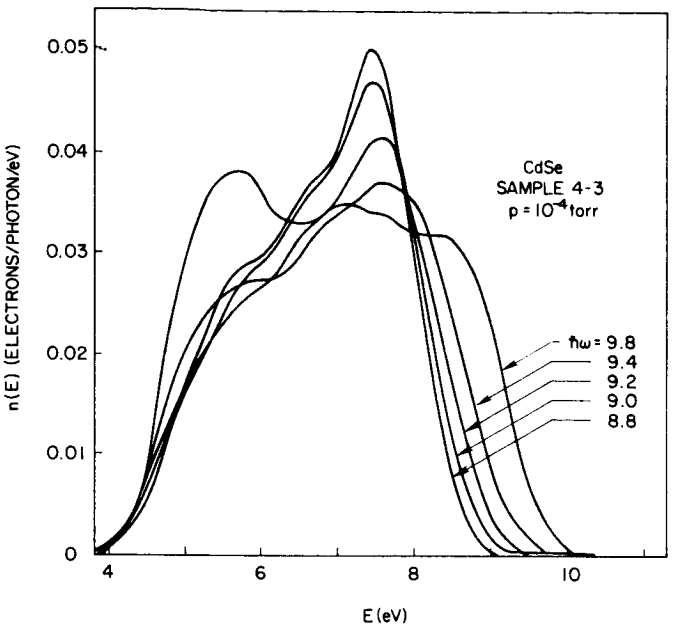

FIG. 91. NORMALIZED ENERGY DISTRIBUTIONS OF THE PHOTOEMITTED ELECTRONS FROM CdSe FOR $8.8 \leq \hbar\omega \leq 9.8$ eV. Electron energy is measured relative to the valence band maximum.

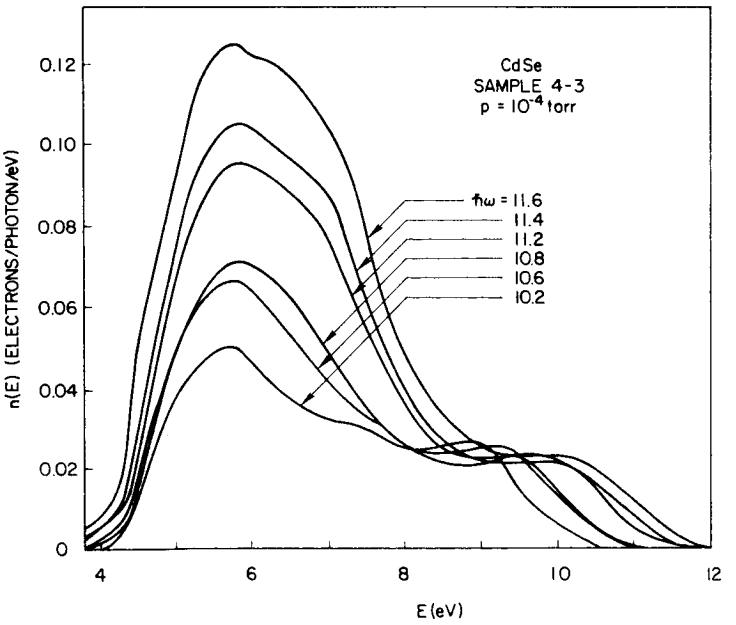

FIG. 92. NORMALIZED ENERGY DISTRIBUTIONS OF THE PHOTOEMITTED ELECTRONS FROM CdSe FOR $10.2 \leq \hbar\omega \leq 11.6$ eV. Electron energy is measured relative to the valence band maximum.

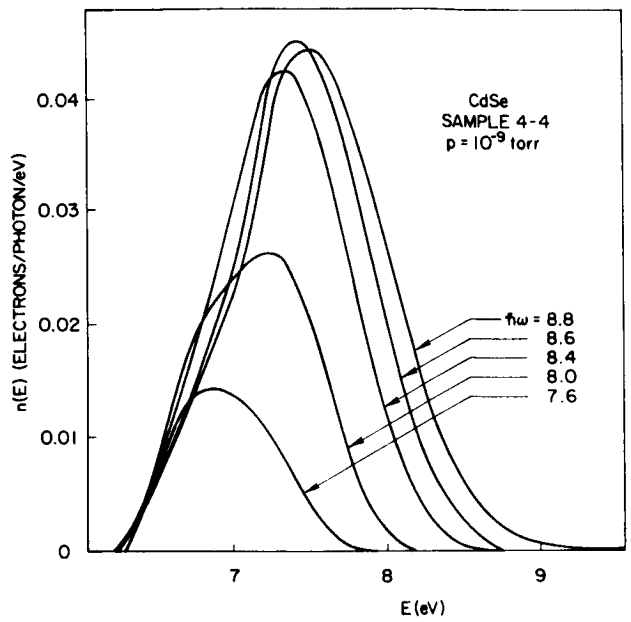

FIG. 93. NORMALIZED ENERGY DISTRIBUTIONS OF THE PHOTOEMITTED ELECTRONS FROM CdSe FOR $7.6 \leq \hbar\omega \leq 8.8$ eV. Electron energy is measured relative to the valence band maximum.

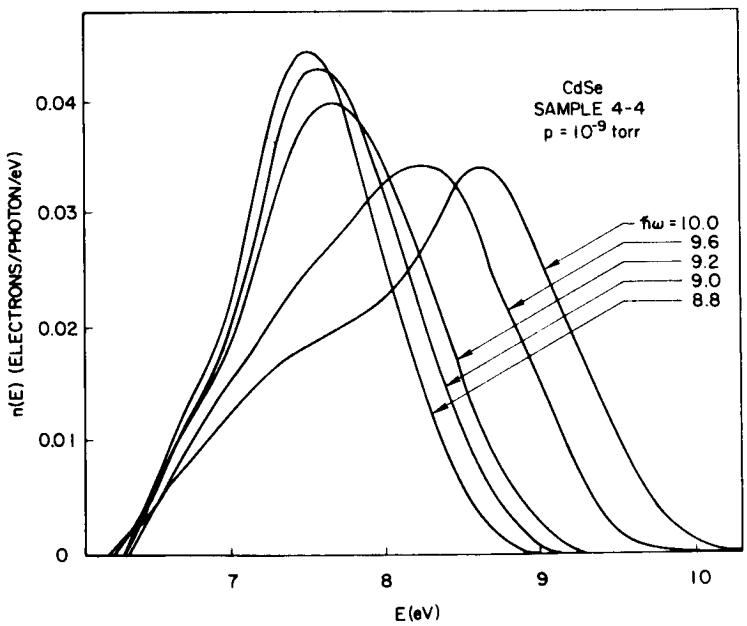

FIG. 94. NORMALIZED ENERGY DISTRIBUTIONS OF THE PHOTOEMITTED ELECTRONS FROM CdSe FOR $8.8 \leq \hbar\omega \leq 10.0$ eV. Electron energy is measured relative to the valence band maximum.

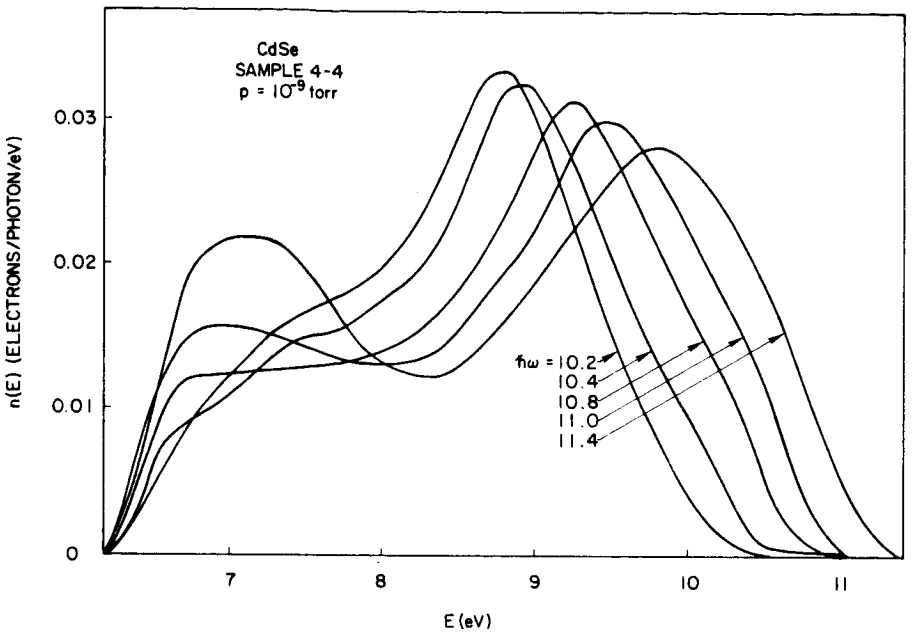

FIG. 95. NORMALIZED ENERGY DISTRIBUTIONS OF THE PHOTOEMITTED ELECTRONS FROM CdSe FOR $10.2 \leq \hbar\omega \leq 11.4$ eV. Electron energy is measured relative to the valence band maximum.

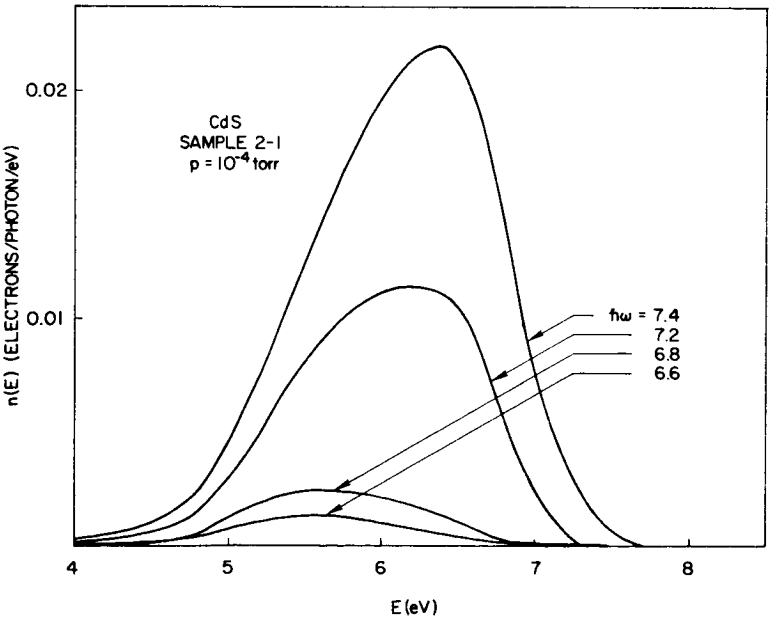

FIG. 96. NORMALIZED ENERGY DISTRIBUTIONS OF THE PHOTOEMITTED ELECTRONS FROM CdS FOR $6.6 \leq \hbar\omega \leq 7.4$ eV. Electron energy is measured relative to the valence band maximum.

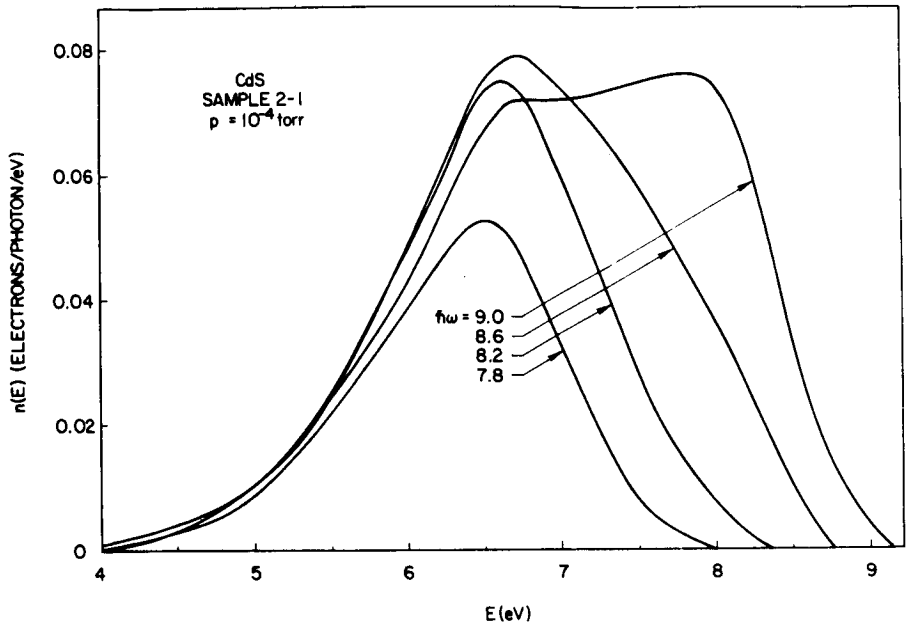

FIG. 97. NORMALIZED ENERGY DISTRIBUTIONS OF THE PHOTOEMITTED ELECTRONS FROM CdS FOR $7.8 \leq \hbar\omega \leq 9.0$ eV. Electron energy is measured relative to the valence band maximum.

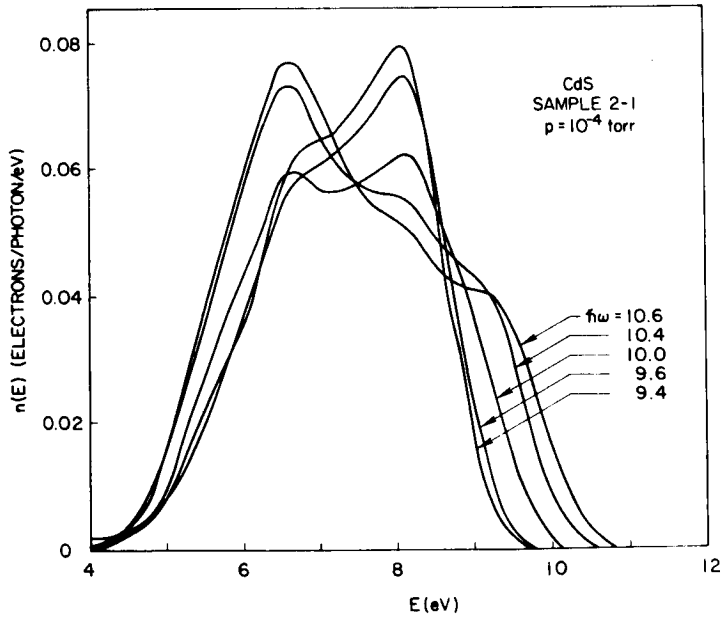

FIG. 98. NORMALIZED ENERGY DISTRIBUTIONS OF THE PHOTOEMITTED ELECTRONS FROM CdS FOR $9.4 \leq \hbar\omega \leq 10.6$ eV. Electron energy is measured relative to the valence band maximum.

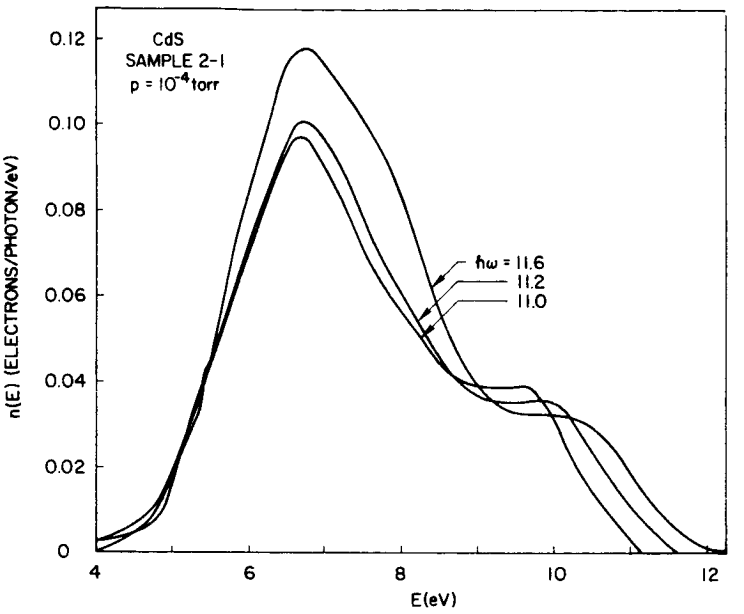

FIG. 99. NORMALIZED ENERGY DISTRIBUTIONS OF THE PHOTOEMITTED ELECTRONS FROM CdS FOR $11.0 \leq \hbar\omega \leq 11.6$ eV. Electron energy is measured relative to the valence band maximum.

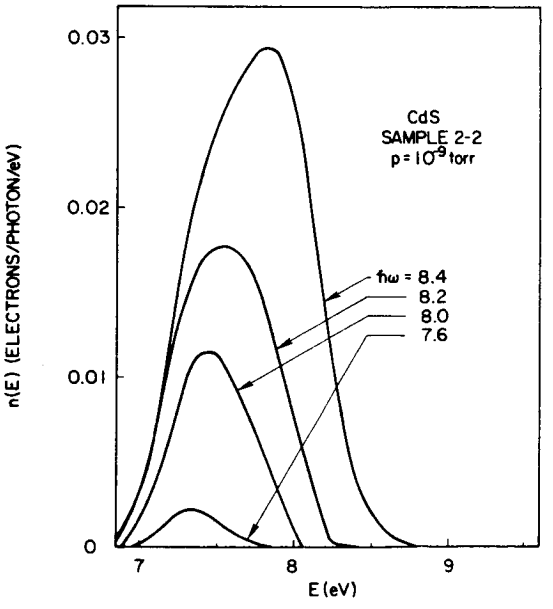

FIG. 100. NORMALIZED ENERGY DISTRIBUTIONS OF THE PHOTOEMITTED ELECTRONS FROM CdS FOR $7.6 \leq \hbar\omega \leq 8.4$ eV. Electron energy is measured relative to the valence band maximum.

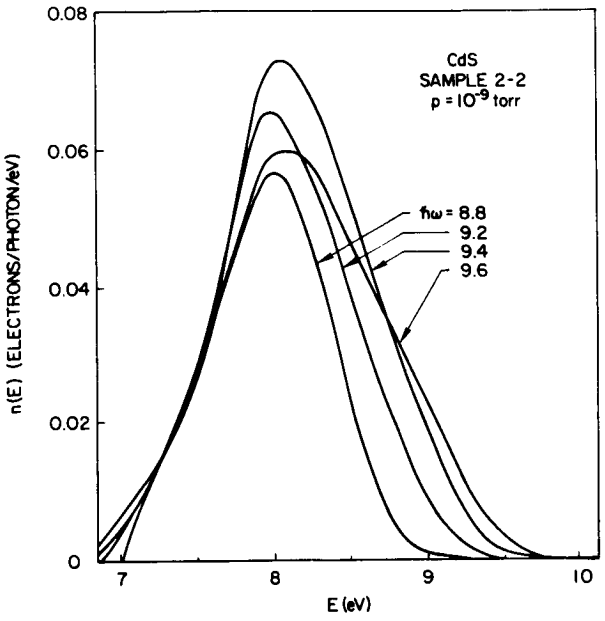

FIG. 101. NORMALIZED ENERGY DISTRIBUTIONS OF THE PHOTO-EMITTED ELECTRONS FROM CdS FOR $8.8 \leq \hbar\omega \leq 9.6$ eV. Electron energy is measured relative to the valence band maximum.

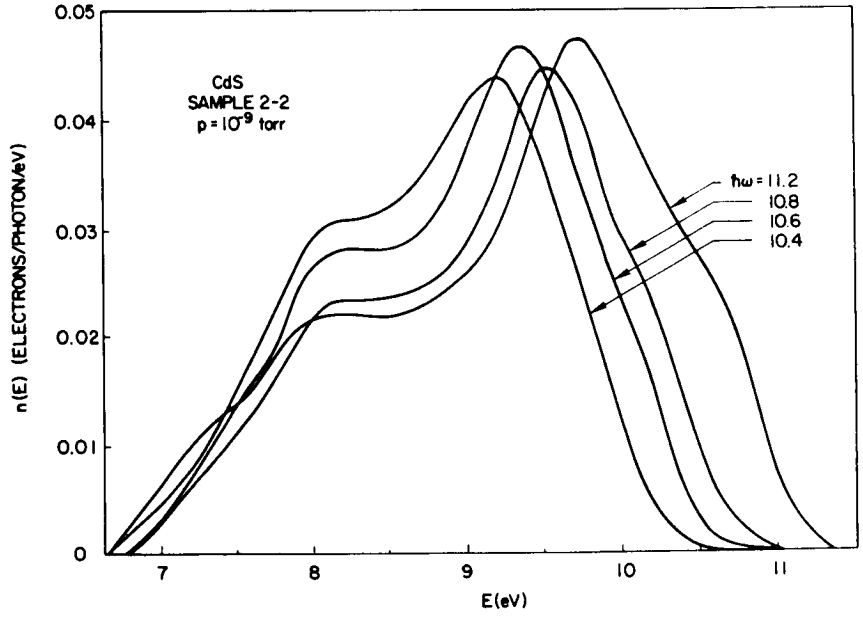

FIG. 102. NORMALIZED ENERGY DISTRIBUTIONS OF THE PHOTO-EMITTED ELECTRONS FROM CdS FOR $10.4 \leq \hbar\omega \leq 11.2$ eV. Electron energy is measured relative to the valence band maximum.

BIBLIOGRAPHY

ANDERSON, P. W., 1964, Concepts in Solids, (W. A. Benjamin, Inc., New York and Amsterdam).

ALLISON, R. et al, 1964, J. Opt. Soc. Am. 54, 747.

APKER, L. 1953, J. Opt. Soc. Am. 43, 78.

BERGLUND, C. N., 1964, Ph.D. Dissertation, Stanford University.

BERGLUND, C. N. and W. E. SPICER, 1964a, Phys. Rev. 136, A1030.

BERGLUND, C. N. and W. E. SPICER, 1964b, Phys. Rev. 136, A1044.

BLOCH, F., 1928, Z. Physik 52, 555.

BLODGETT, A. J. and W. E. SPICER, 1965, Phys. Rev. Letters 15, 29.

BLODGETT, A. J., W. E. SPICER and A. Y-C. YU, 1966, Optical Properties and Electronic Structure of Metals and Alloys, (Proceedings of the International Colloquium, held at Paris, 13-16 September 1965), (North-Holland Publishing Company - Amsterdam) p. 246.

CALLAWAY, J., 1964, Energy Band Theory, (Academic Press, New York and London).

CARDONA, M., 1965, J. Appl. Phys. 36, 2181.

CARDONA, M. and D. L. GREENAWAY, 1963, Phys. Rev. 131, 98.

CARDONA, M. and G. HARBEKE, 1965, Phys. Rev. 137, A1467.

COHEN, M. L. and T. K. BERGSTRESSER, 1966, Phys. Rev. 141, 789.

EDEN, R. C. 1966, Ph.D. Dissertation, Stanford University.

FOCK, V., 1930, Z. Physik 61, 126.

FOYT, A. G., (private communication in Band Structure GE Report #66-C-007, by B. Segall, 1966).

GUNN, J. B., 1963, Solid State Commun. 1, 88.

HARTREE, D. R., 1928, Cambridge Phil. Soc. 24, 89.

HERMAN, F., R. L. KORTUM, C. C. KUGLIN, and R. A. SHORT, 1966, in Quantum Theory of Atoms, Molecules, and the Solid State: A Tribute to J. C. Slater, ed. Par-Olov Löwdin, (Academic Press, New York).

HILSUM, C., 1962, Proc. IRE 50, 185.

HUTSON, A. R. et al, 1965, Phys. Rev. Letters 14, 639.

KANE, E. O., 1966a, Proceedings of the International Conference on the Physics of Semiconductors, Kyoto, in press.

KANE, E. O., 1966b, Phys. Rev. 146, 558.

KINDIG, N. B., 1964, Ph.D. Dissertation, Stanford University.

KINDIG, N. B. and W. E. SPICER, 1965a, Phys. Rev. 138, A561.

KINDIG, N. B. and W. E. SPICER, 1965b, Rev. Sci. Instr. 36, 759.

KNOX, R. S., 1963, Theory of Excitons, in Solid State Physics, Suppl. 5, ed. F. Seitz and D. Turnbull, (Academic Press, New York and London).

KOOPMANS, T., 1933, Physica 1, 104.

KOYAMA, R., 1966 (to be published).

LINDGREN, I., 1965, Physics Letters 19, 382.

MARPLE, D. T. F. and H. EHRENREICH, 1962, Phys. Rev. Letters 8, 87.

MOORE, C. E., 1949, Atomic Energy Levels, Natl. Bur. Std. Circular 467, (U. S. Government Printing Office, Washington, D.C.).

NESBET, R. K., 1958, Phys. Rev. 109, 1632.

OVERHAUSER, A. W., 1962, Phys. Rev. 128, 1437.

PHILLIPS, J. C., 1964, Phys. Rev. 133, A452.

PHILLIPS, J. C., 1966, The Fundamental Optical Spectra of Solids, in Solid State Physics, Volume 18, ed. F. Seitz and D. Turnbull, (Academic Press, New York and London).

POWELL, R. J., 1966, Ph.D. Dissertation, Stanford University.

SCHIFF, L., 1955, Quantum Mechanics, second edition, (McGraw-Hill, New York).

SEITZ, F., 1940, The Modern Theory of Solids, (McGraw-Hill, New York).

SLATER, J. C., 1930, Phys. Rev. 35, 210.

SLATER, J. C., 1951, Phys. Rev. 81, 385.

SPICER, W. E., 1961, J. Phys. Chem. Solids 22, 365.

SPICER, W. E., 1963, Phys. Rev. Letters 11, 243.

SPICER, W. E., 1966, Optical Properties and Electronic Structure of Metals and Alloys, (Proceedings of the International Colloquium, held at Paris, 13-16 September 1965), (North-Holland Publishing Company - Amsterdam) p. 296.

SPICER, W. E. and C. N. BERGLUND, 1964, Rev. Sci. Instr. 35, 1665.

SPICER, W. E. and G. J. LAPEYRE, 1965, Phys. Rev. 139, A565.

STUART, R. N., F. WOOTEN, and W. E. SPICER, 1963, Phys. Rev. Letters 10, 7.

TINKHAM, M., 1964, Group Theory and Quantum Mechanics, (McGraw-Hill, New York).

WALKER, W. E. and J. OSANTOWSKI, 1964, J. Phys. Chem. Solids, 25, 778.

UNCLASSIFIED
Security Classification

DOCUMENT CONTROL DATA - R & D

(Security classification of title, body of abstract and indexing annotation must be entered when the overall report is classified)

1. ORIGINATING ACTIVITY (Corporate author)	2a. REPORT SECURITY CLASSIFICATION
Stanford Electronics Laboratories Stanford University Stanford, California	Unclassified
	2b. GROUP

3. REPORT TITLE

PHOTOEMISSION STUDIES OF THE ELECTRONIC STRUCTURE OF CdTe, CdSe, AND CdS

4. DESCRIPTIVE NOTES *(Type of report and inclusive dates)*

Technical Report

5. AUTHOR(S) *(First name, middle initial, last name)*

Joseph L. Shay

6. REPORT DATE	7a. TOTAL NO. OF PAGES	7b. NO. OF REFS
December 1966	148	50

8a. CONTRACT OR GRANT NO.	9a. ORIGINATOR'S REPORT NUMBER(S)
NASA Grant NGR 05-020-066, CMR Contract SD-87 and NSF Grant GP-1033 and GK-149 b. PROJECT NO.	Technical Report 5216-1
c. d.	9b. OTHER REPORT NO(S) *(Any other numbers that may be assigned this report)* SEL-66-112

10. DISTRIBUTION STATEMENT

Reproduction in whole or in part is permitted for any purpose of the United States Government.

11. SUPPLEMENTARY NOTES	12. SPONSORING MILITARY ACTIVITY

13. ABSTRACT

Photoemission studies are used to determine properties of the electronic structure of CdTe, CdSe, and CdS over an energy range extending from about 10 eV below to 10 eV above the valence band maximum. The features of the photoemission from CdSe and CdS are very similar; however the features of the photoemission from CdTe are quite different from those of CdSe and CdS.

The sharp features of the CdTe photoemission data are due to direct transitions. These direct transitions are assigned to specific regions of the Brillouin zone, and several reflectivity peaks are given new assignments. Although there are sharp matrix-element variations in CdSe and CdS, few of these have been positively identified as being due to direct transitions. Using the density of states analysis, we have separated the matrix-element-dependent transitions from those due only to the density of states.

The mean free path for electron-electron scattering increases in the sequence CdTe, CdSe, and CdS. For electrons about 8.5 eV above the top of the valence band, approximate values for the escape depths are 16, 64, and 75 Å. Since the electron-electron scattering is strongest in CdTe and weakest in CdS, the yield is smallest in CdTe and largest in CdS.

The d-band of cadmium is at about 8 eV below the other valence band states in CdTe, CdSe, and CdS. We show that the slight changes in the location of the d-band in the sequence CdTe, CdSe, and CdS are consistent with both the ionic and the covalent models for the II-VI compounds. Hence we are unable to determine the degree of ionicity of these materials.

DD FORM 1 NOV 65 1473

UNCLASSIFIED
Security Classification

14. KEY WORDS	LINK A		LINK B		LINK C	
	ROLE	WT	ROLE	WT	ROLE	WT
CdS BAND STRUCTURE AND PHOTOEMISSION						
CdSe BAND STRUCTURE AND PHOTOEMISSION						
CdTe BAND STRUCTURE AND PHOTOEMISSION						